

Draft TAMSAT Technical Report: TAMSAT version 3 calibration methodology

September 2016



TAMSAT Group, Department of Meteorology, University of Reading, RG6 6BB, UK
Email: tamsat@reading.ac.uk **Web:** www.tamsat.org.uk

1. Introduction

This report describes a new methodology for historical calibration of rainfall estimates derived from satellite thermal infrared imagery (TIR). The report has been prepared by the University of Reading TAMSAT group as a deliverable from the Joint Research Centre's Monitoring Agriculture with Remote Sensing Operationally (MARSOP4) programme (specifically, *D5.8 Ad hoc development/improvements: calibration development*).

The TAMSAT rainfall estimation approach complements other satellite-based rainfall estimation methods, and as a result TAMSAT data have been widely used for seasonal early warning of drought and assessments of long-term agricultural risk (Black et al, 2015, 2016). In particular:

- Using a historical calibration avoids the temporal biases that arise from inconsistent gauge datasets (Maidment et al, 2015).
- The use of calibration zones enables estimation of rainfall in regions with sparse gauge coverage, without making the false assumption that the cloud-rainfall relationship is stationary for all of Africa and for the whole seasonal cycle (Tarnavsky et al, 2014).

The revision of the TAMSAT calibration method described in this report is motivated by two shortcomings. Firstly, the use of large calibration zones inevitably leads to jumps in calibration parameters and hence to spatial artefacts in the estimates. These artefacts are particularly pronounced when estimates are aggregated in time. For example, the sharp zonal gradient in January climatological mean rainfall evident at around 20°E / 5°S in the left panel of Figure 1.1 results from an abrupt change in one of the calibration parameters (right panel).

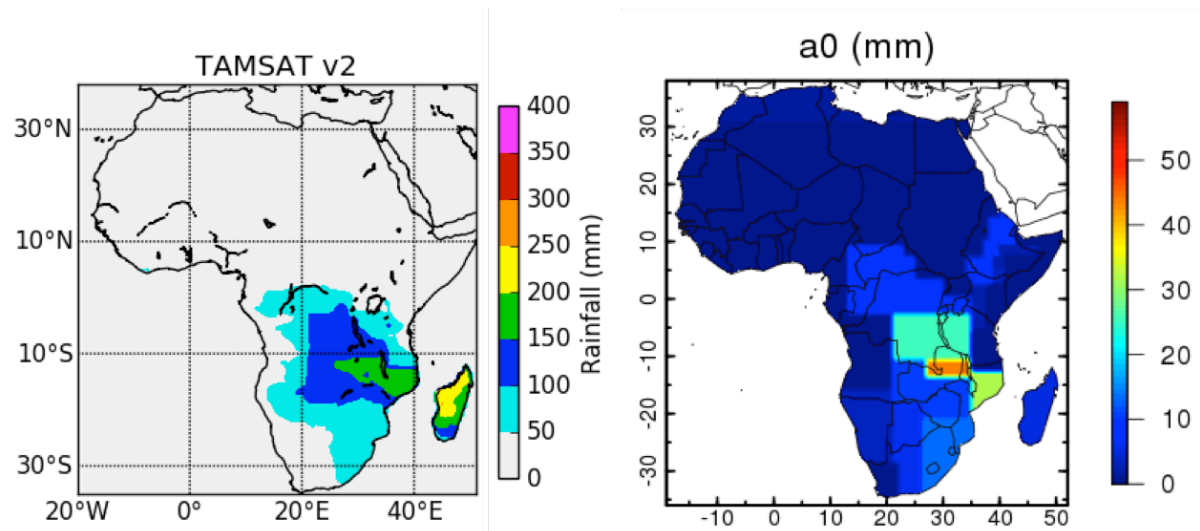


Figure 1.1: Left TAMSATv2 January climatological rainfall; Right Intercept (a_0) calibration parameter map.

Secondly, while some underestimation of rainfall is inevitable for TIR based rainfall products (especially where warm rain processes dominate), in most regions the TAMSAT bias is more severe than for other satellite-based datasets (Figure 1.2 and Maidment et al 2014).

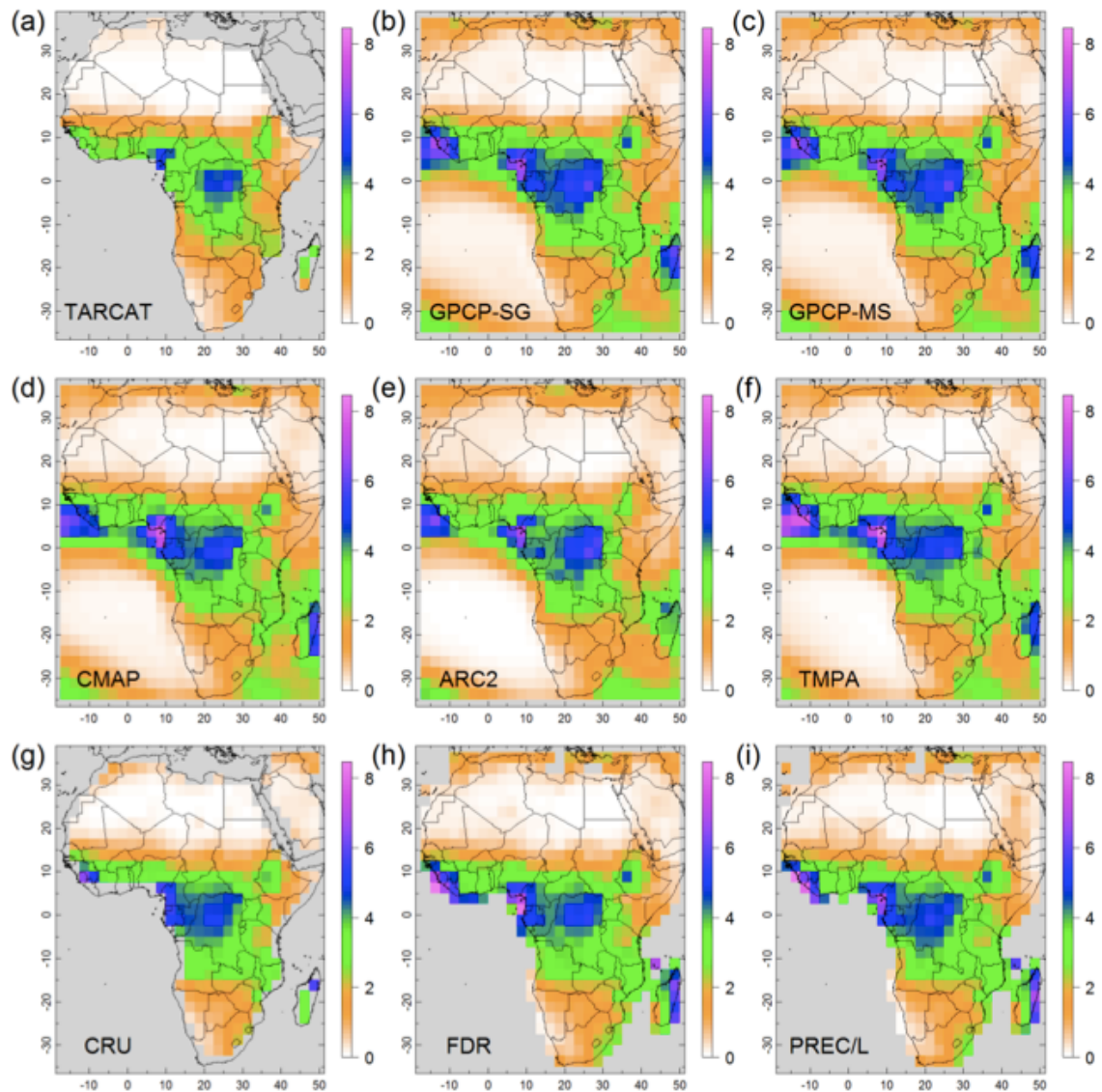


Figure 1.2 Spatial annual rainfall climatology (mm day⁻¹) over the period 1983 to 2010 for (a) TARCAT, (b) GPCP-SG, (c) GPCP-MS, (d) CMAP, (e) ARC2, (f) TMPA (using 1998 – 2010 estimates), (g) CRU, (h) FDR and (i) PREC/L at 2.5° resolution. [From Maidment et al, 2013]

In this report, we present a modified calibration method, which preserves the main features of the TAMSAT approach, whilst eliminating spatial artefacts and markedly reducing the dry bias.

The rest of the report is structured as follows. Section 2 describes the basis of the TAMSAT methodology; Section 3 describes the new calibration method, highlighting changes from the old method; Section 4 presents the new calibration parameters, rainfall estimates and a preliminary validation against the gridded gauge-only Global Precipitation Climatology Centre rainfall dataset (hereinafter GPCP). A series of sensitivity studies, which informed the key decisions made about methodology, are described in an appendix.

2. Basis of the TAMSAT approach

The physical basis of the TAMSAT method is that rainfall in Africa primarily originates from deep convective clouds that penetrate into the upper levels of the troposphere and thus have cold cloud tops. The method therefore assumes that cloud tops colder than a certain threshold temperature produce rain, while cloud tops warmer than this threshold don't rain. From this assumption it also follows that the longer the time the cloud is below this rain/no-rain temperature threshold, the more rain it produces. Thus, the length of time a cloud is below the temperature threshold (cold cloud duration; CCD) can be linearly related to the rainfall amount, R using:

$$R = \begin{cases} a_0 + a_1 CCD & CCD > 0 \\ 0 & CCD = 0 \end{cases}$$

Where R is in mm and a_0 and a_1 are the calibration parameters. The optimal threshold temperature and calibration parameters in this linear relationship are found by calibrating CCD derived from geostationary TIR measurements to a historic rain gauge archive (Tarnavsky et al., 2014). It is important to note that the calibration is conducted for dekadal rainfall and CCD measurements. However, TAMSAT also produces daily rainfall estimates by temporally disaggregating the dekadal rainfall estimates using the daily CCD (Maidment et al., 2012).

Because convective rainfall characteristics over Africa have marked seasonal and regional variability, the optimal temperature threshold and CCD-rainfall relationship described above varies both spatially and temporally.

3. TAMSAT v3.0 calibration methodology

3.1 Key developments

The essence of the TAMSAT approach is preserved in the new version. In particular, the estimates do not incorporate real time information from gauges; a spatially and temporally varying historical calibration is used; and rainfall occurrence and amount are treated separately.

A significant difference between TAMSAT v3 and previous versions is that calibration is carried out at a daily and pentadal time scale, rather than at a 10-daily scale (Appendix 2). Furthermore, to reduce the rainfall bias, CCD is calibrated against mean rather than median rainfall (Maidment et al, 2014). In some regions of Africa, using more than one CCD threshold to model rainfall has been shown to be beneficial (Greatrex et al, 2014). However, further sensitivity studies indicate that, the advantage of using multiple thresholds is not sufficient to justify the computational expense at the continental scale (Appendix 2)

In the previous version of TAMSAT, the expected spatial variability in the rainfall-cloud relationship was accounted for using calibration zones. In order to avoid spatial artefacts, calibration zones are not used for TAMSAT v3.0. Without a dense gauge network, deriving spatially and temporally varying calibration parameters is not straightforward. The

approach taken here is to derive optimal CCD temperature thresholds for 1 degree boxes, which are then interpolated for all of Africa. The regression intercept and slope parameters (a_0 and a_1) are then modelled on T_t and scaled using an established climatology

A full account of the calibration steps is given in the next section. For comparison, the calibration procedure for TAMSAT v2 is summarised in Appendix 3.

3.2 Details of the calibration process

The estimation of rainfall can be considered as a two-part process. The initial step delineates rainy regions from non-rainy regions. The second step assigns a rain rate or amount. The estimation of rainfall can therefore be expressed as a product of rainfall occurrence and rainfall intensity computed over each satellite pixel at a given time-step.

As with the estimation of rainfall, the calibration is split into two parts: derivation of the optimum temperature threshold (T_t) which determines if a pixel is rainy or not and derivation of the linear regression coefficients (a_0 and a_1) which determines the rainfall amount for rainy pixels. This approach applies to both version 2 and version 3 of the calibration.

The calibration steps below were performed Africa-wide and repeated for each month.

3.2.1 Preparatory steps

1. Daily cold cloud duration (CCD) files at a range of temperature thresholds (between -30°C and -60°C) are created using available Meteosat satellite imagery between 1983 and 2014. The methodology for deriving CCD is described in Milford et al, 1994.
2. Africa-wide daily gauge records from various sources (e.g. CHG, TAMSAT archive, JRC, SWALIM) are quality controlled and collated into a single database. The locations of gauges used in the calibration are shown in Figure 3.1.
3. For every daily gauge record, the corresponding CCD pixel values at temperature thresholds of -20°C , -30°C , -40°C , -50°C , -60°C are extracted.

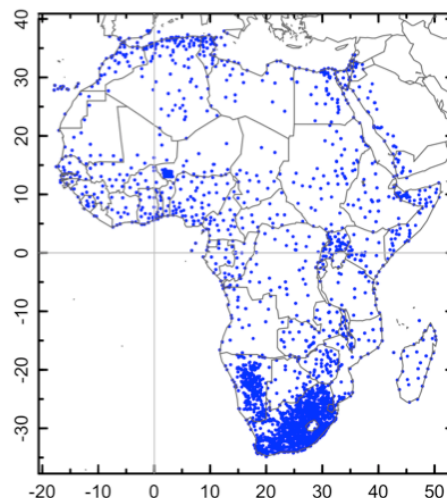


Figure 3.1 Distribution of the rain gauges used to derive the calibration parameters in TAMSAT v3

3.2.2 Derivation of the optimum temperature threshold

1. Derivation of T_t is carried out at the daily scale. This is because (1) it physically makes sense as daily CCD/rainfall values are able to differentiate between rainy and dry days better than temporally aggregated data (e.g. pentadal or dekadal) and (2) there are more events to analyse, especially in regions with few gauge records.
2. Daily gauge-CCD pairs are binned (spatially) into $1^\circ \times 1^\circ$ grid squares across Africa. The T_t is then determined based on the frequency bias for grid squares containing at least 100 gauge-CCD pairs. Typically, this results in around 800 grid squares across Africa where T_t is calculated. Note that, in contrast to previous versions of the TAMSAT calibration methodology, T_t is derived to the nearest degree by interpolating the calculated CCD values explicitly derived from the imagery.
3. These temperature threshold values are then spatially interpolated to produce Africa-wide maps of T_t , using ordinary kriging with a 20° range.
4. Using maps of T_t , daily CCD variable temperature threshold maps are created from 1983 to 2015.

3.2.3 Derivation of a_0 and a_1

1. Derivation of the calibration parameters is based on the pentadal (5-day) gauge-CCD pairs (see Appendix 2).
2. For each $1^\circ \times 1^\circ$ grid square where there are gauge-CCD pairs, the pentadal gauge-CCD pairs are binned by CCD value at regular intervals. A $1^\circ \times 1^\circ$ grid is deemed large enough to contain sufficient gauge-CCD pairs to derive stable temperature thresholds, yet small enough to capture local variations). Linear calibration coefficients (a_0 and a_1) are then estimated by regressing the mean gauge rainfall against the mean CCD value for each bin. This is repeated for each CCD temperature threshold value (i.e. between -30°C to -60°C at 1°C intervals) to produce a table of regression coefficients for each CCD temperature threshold at each grid square.
3. Calibration coefficients from all months and across Africa are then collated and modelled as a function of CCD temperature threshold to produce a lookup table. Africa-wide maps of the a_0 and a_1 are then created based on the corresponding T_t .
4. Using these parameters and the daily CCD variable temperature threshold maps, a time-series of intermediate rainfall estimates for 1983-2009 is created using the standard TAMSAT rainfall estimation algorithm (i.e. $rain = a_0 + a_1 CCD$).
5. Ratios of an established pentadal rainfall climatology (CHPclim – described in Funk et al, 2015) and the TAMSAT pentadal intermediate climatology created from the intermediate estimates are created for each pentad. Such maps indicate the scaling that needs to be applied to the correct for geographic systematic biases not captured in the intermediate TAMSAT estimates. To avoid artefacts resulting from division of small numbers, the ratio is constrained to fall in the range 0.2 – 6.
6. The intermediate calibration coefficient (a_0 and a_1) monthly maps are multiplied by the pentadal ratio maps to create maps of a_0 and a_1 for all 72 pentads.

3.3 Calibration parameters

Examples of the calibration parameters are given in Figures 3.1 and 3.2, for TAMSAT v2 and TAMSAT v3 (calibration parameters for each pentad can be found in Appendix 4). In TAMSAT v3, the calibration parameters vary smoothly for all of Africa, broadly following expected topographic and seasonal patterns. In general, T_t reflects the broad seasonal cycle, with additional topographic-related features incorporated via a_0 and a_1 . This is consistent with our general understanding of tropical rainfall, which is that seasonal mean rainfall occurrence is determined largely by large-scale dynamic features, while seasonal mean intensity is strongly modulated by orography.

Whilst some of the broad features of the v2 calibration are preserved, the v3 calibration is markedly different. In the figures below, for example, it can be seen that the temperature thresholds in dry regions, such as West Africa in January, are colder in v3 than in v2. The greater spatial detail is particularly evident in the monsoon season in West Africa, where the east-west and north-south gradients in T_t reflect known climatological patterns of rainfall.

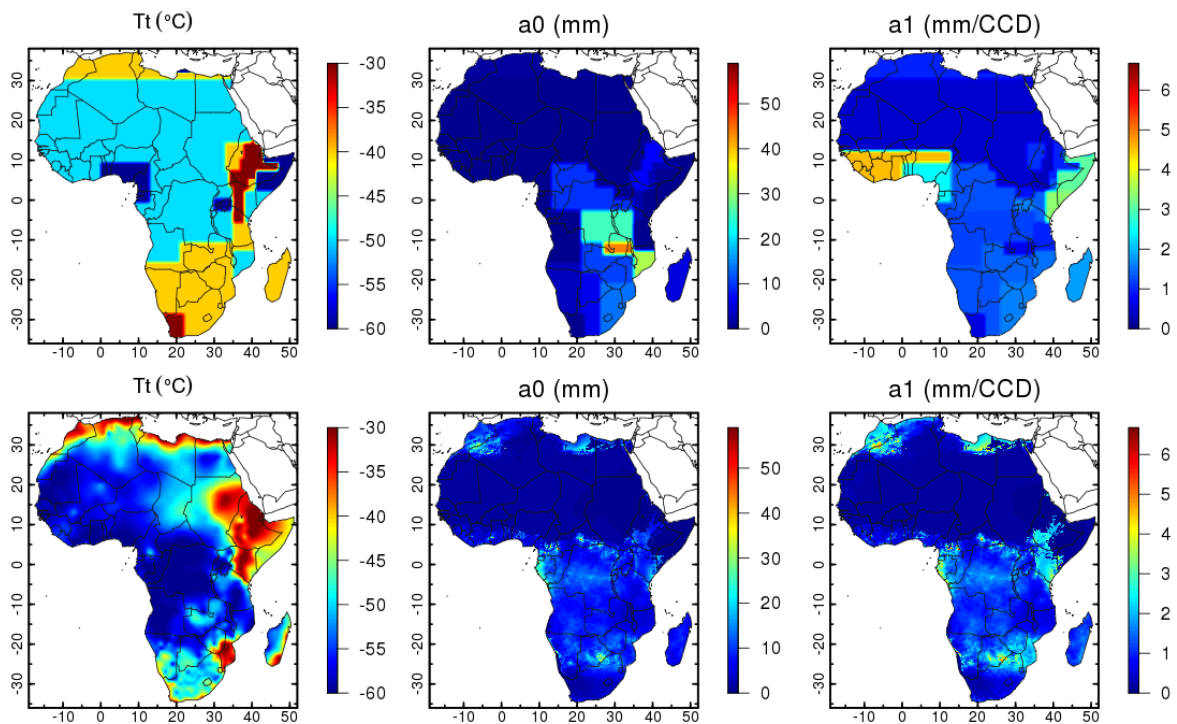


Figure 3.1 Comparison of the calibration parameters (T_t , a_0 and a_1) for the month (v2, top row) and 1st pentad (v3, bottom row) of January. Because of the change in the calibration time step, the pentadal calibration maps are shown along with their respective monthly calibration maps from v2.

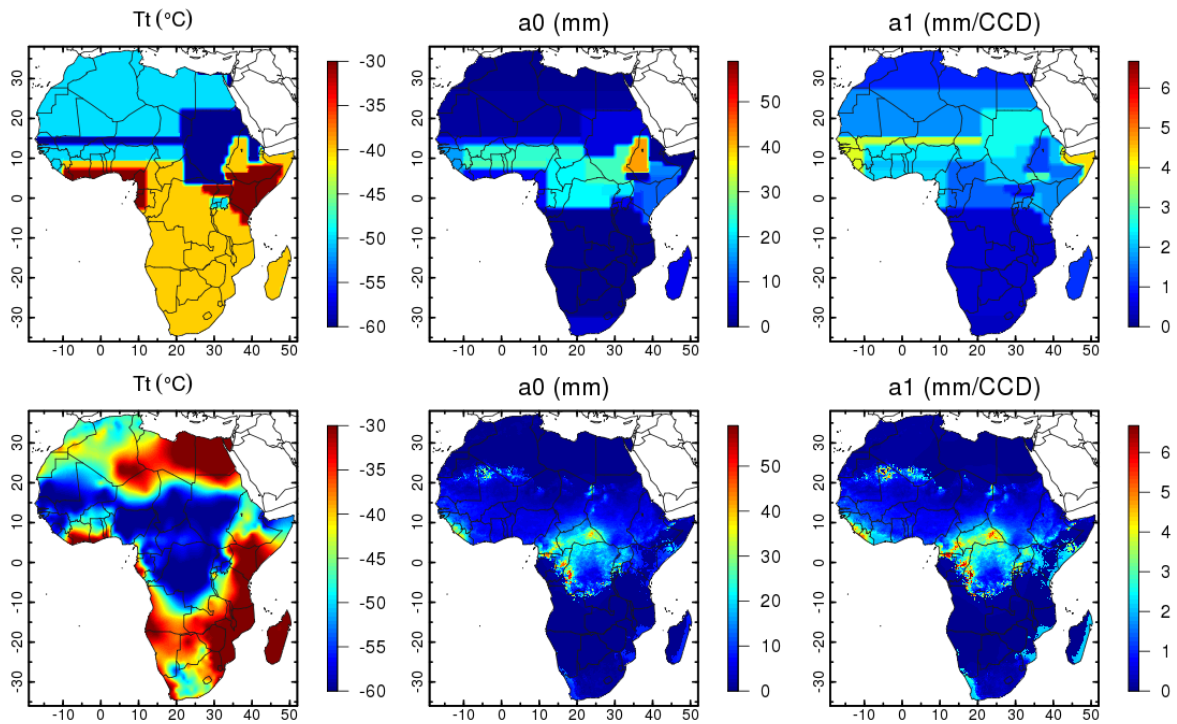


Figure 3.2 Same as Figure 3.1 but for the month (v2) and 1st pentad (v3) of August.

4. TAMSAT 3.0 Rainfall estimates

Examples of dekadal rainfall estimates for TAMSAT v3.0 and TAMSAT v2.0 are shown in Figure 4.1. In TAMSAT v2.0, the use of calibration zones results in spatial artefacts, including a meridional feature at around 20^oE longitude in the January dekad and low rainfall rectangle centered around 25^oE/5^oN in the August dekad. TAMSAT v3.0, in contrast, does not contain obvious spatial artefacts. The TAMSAT v3.0 rainfall is more spatially variable, especially in the high rainfall regions in Central and Southern Africa. In most, but not all locations, rain amounts in TAMSAT v3.0 are higher than in TAMSAT v2.0. As with the dekadal estimates, in TAMSAT v3.0, the spatial artefacts that affected TAMSAT v2.0 are eliminated, spatial variability is higher and in most locations, rainfall is greater (Figure 4.2).

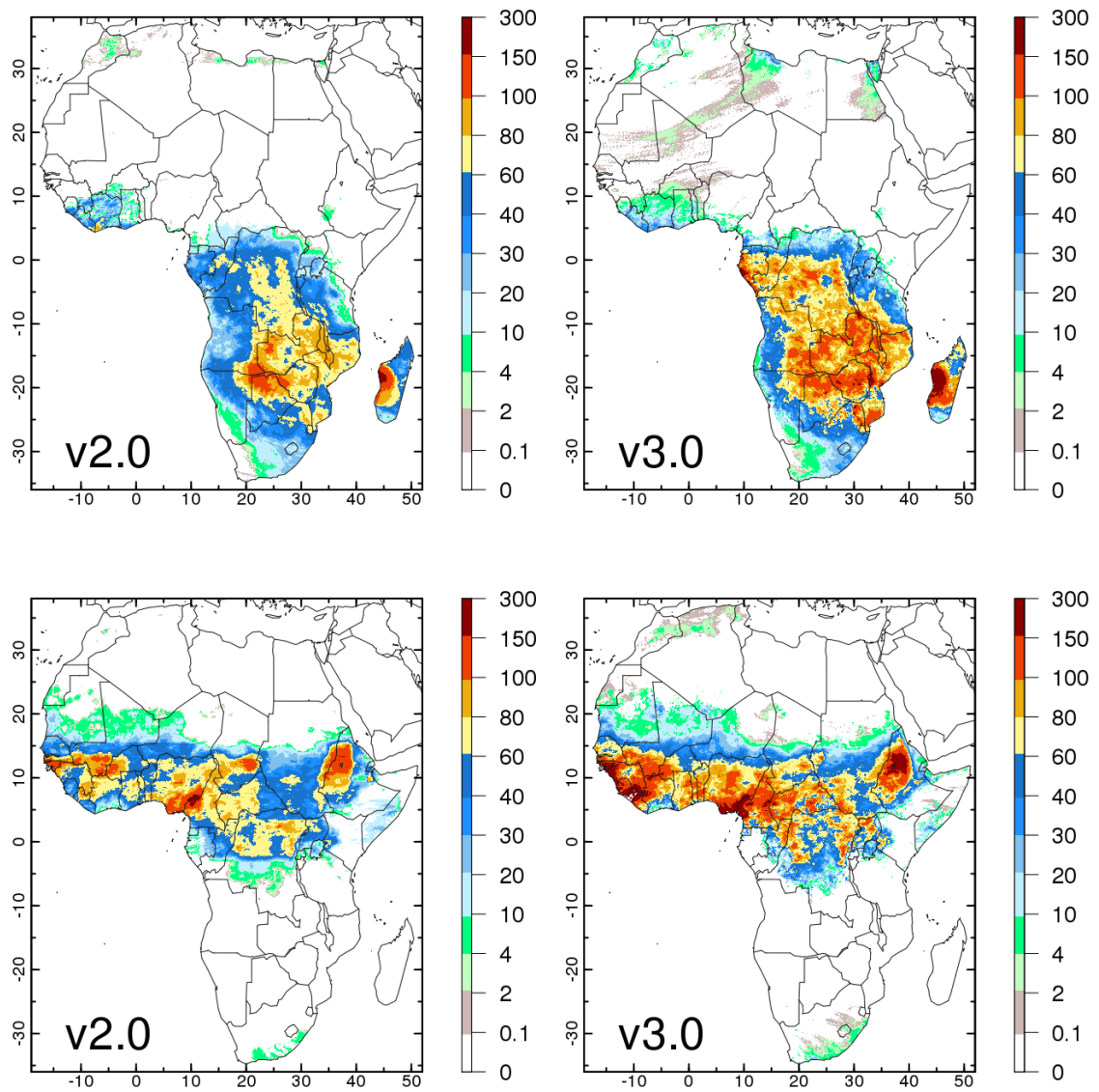


Figure 4.1 Comparison of TAMSAT v2 and v3 dekadal rainfall estimates (mm) for the 1st dekad of January 2000 (top row) and 1st dekad of August 2000 (bottom row).

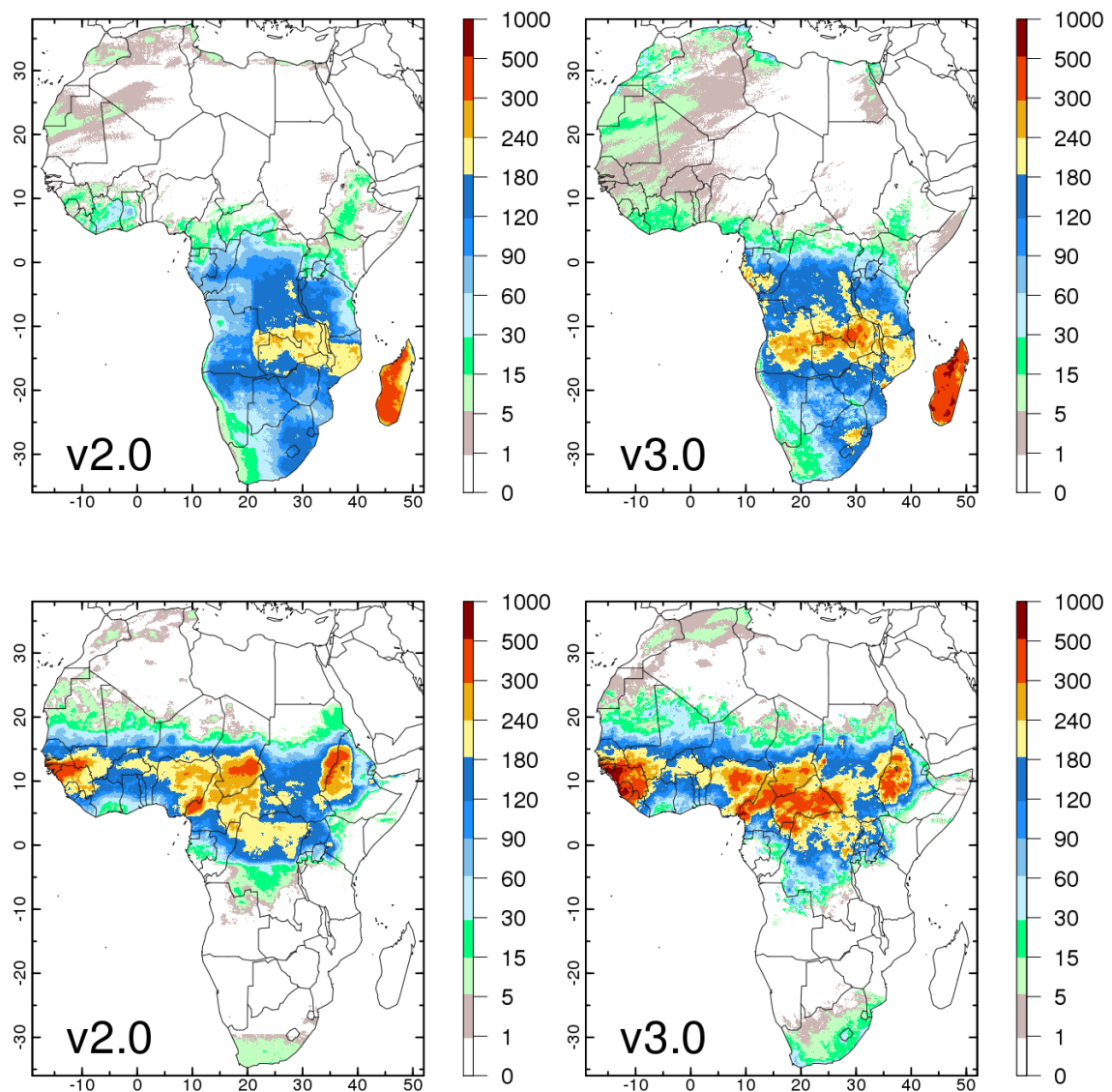


Figure 4.2 Comparison of TAMSAT v2 and v3 monthly rainfall estimates (mm) for January 2005 (top row) and August 2005 (bottom row).

The skill of TAMSAT v3, as compared to TAMSAT v2, has been assessed through a comparison with the GPCP gridded rainfall dataset. The GPCP data used in this study are based purely on gauge observations, and are provided at monthly time scale. The GPCP set of products consists of two datasets, a full data reanalysis (FDR), including all available gauge data and a dataset incorporating only gauges with long, consistent records (VasCLIMO), available for 1982-present. For these analyses, the 0.5° resolution full data reanalysis (FDR) is used for the period 1983-2015 (Schneider et al, 2015). TAMSAT data have regridded onto the GPCP grid for all plots and statistical analyses.

It should be noted that many of the gauges used in the GPCP FDR dataset will have been used in the TAMSAT v2 and v3 calibration. However, since temporal variability in TAMSAT is determined solely by variability in CCD, comparison with GPCP can be considered, to some extent, an independent validation.

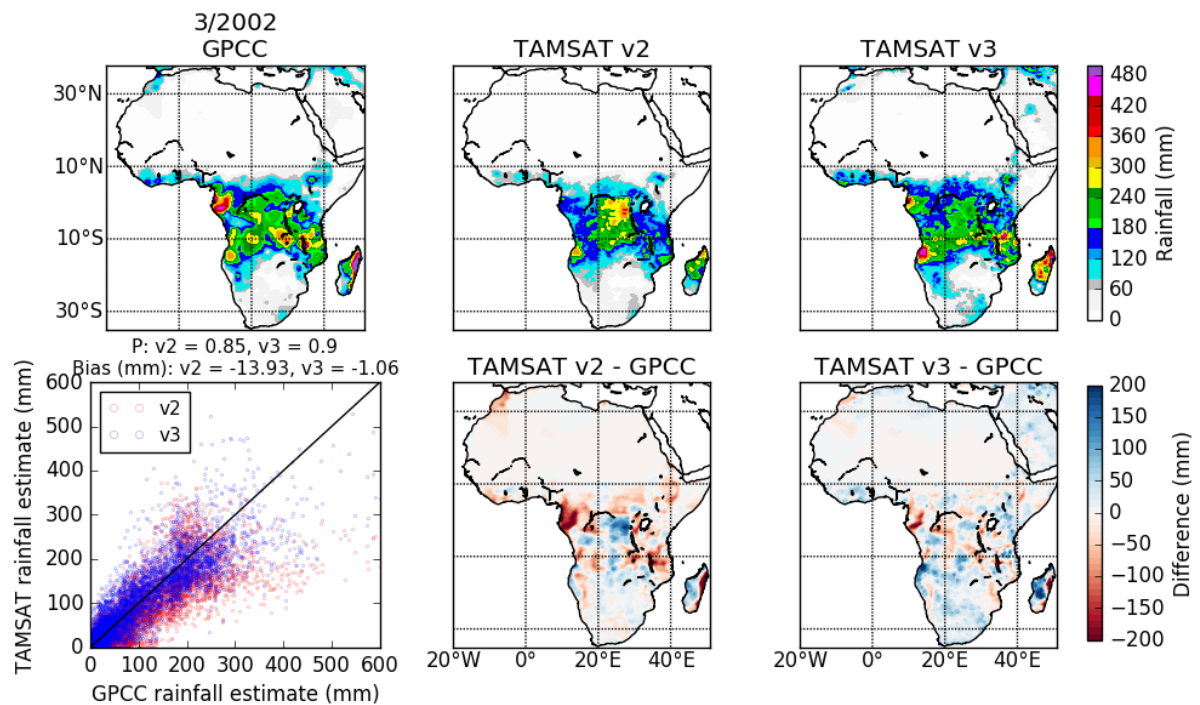


Figure 4.3. An example comparing rainfall estimates during March 2002 from TAMSAT v2, TAMSAT v3 and GPCC. Statistics (Pearson's correlation coefficient, P and bias) comparing TAMSAT v2 and v3 with GPCC are shown above the scatter plot.

Figure 4.3 shows a comparison between TAMSAT v2, TAMSAT v3 and GPCC monthly rainfall estimates for an example month. It can be seen that while the gross spatial pattern of rainfall, as depicted by the GPCC data, is captured by both TAMSAT v2 and TAMSAT v3, there are some discrepancies. For example, neither TAMSAT v2 or v3 represent the spatial extent of the high rainfall in Madagascar or the intensity of the high rainfall in Equatorial Guinea. Nevertheless, the pattern correlations are high for both versions of TAMSAT (0.85 and 0.89 respectively for v2 and v3). The TAMSAT dry bias is reduced markedly in v3 compared to v2 (-1.06mm compared to -13.93mm).

Figure 4.4 compares the annual mean rainfall for TAMSAT v2, TAMSAT v3 and GPCC. It can be seen that compared to TAMSAT v2, v3 captures more of the spatial detail evident in the GPCC data, including the high rainfall on the Guinea coast. Rainfall amounts are generally higher in TAMSAT v3.0 than in TAMSAT v2.0 and agree more closely with GPCC. There remain significant differences between TAMSAT v3.0 and the GPCC climatology, especially in Central Africa. It should be noted, however, that in Central Africa few gauges were available either in for the GPCC product, or for the TAMSAT calibration. Agreement between gridded rainfall datasets is consequently poor in this region (Maidment et al, 2014, 2015, Washington et al, 2013).

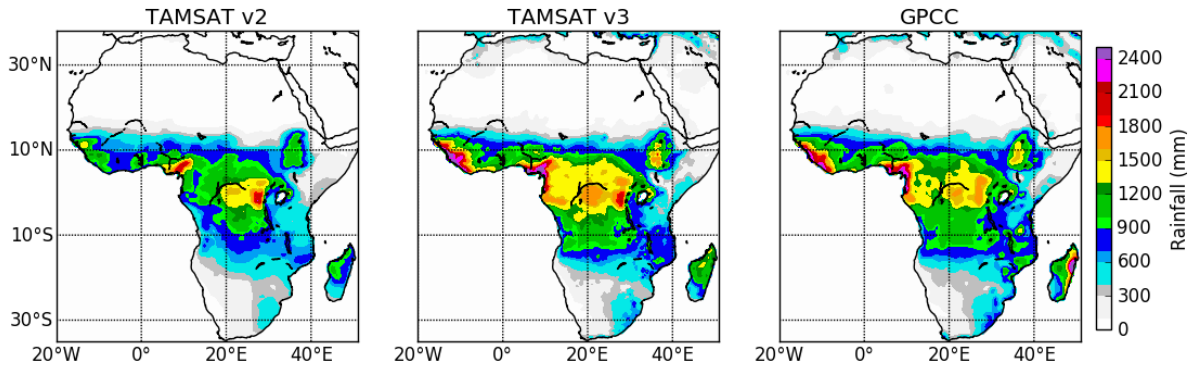


Figure 4.5. Annual mean rainfall estimated by TAMSAT v2, TAMSAT v3 and GPCC, 1983–2013.

Figure 4.6 shows the seasonal climatological cycle for TAMSAT v2, TAMSAT v3 and GPCC. Although not obvious from the annual climatology, the seasonal comparisons show that the TAMSAT v3 climatology for Angola and Central Africa is improved compared to GPCC (see Appendix 1 for plots of individual months).

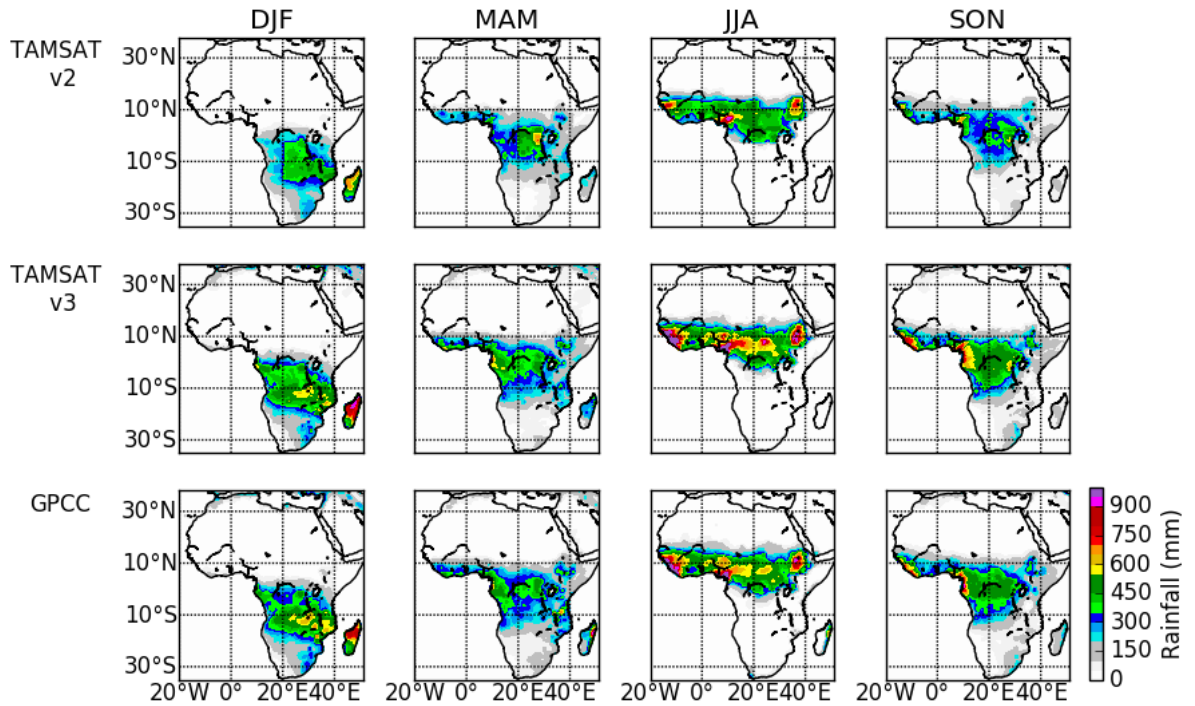


Figure 4.6. Seasonal mean rainfall (December – February, DJF; March – May, MAM; June – August, JJA; September – November, SON) estimated by TAMSAT v2, TAMSAT v3 and GPCC, 1983–2013.

Quantitative comparisons of TAMSAT v2 and v3 with GPCC are shown in Figures 4.7 – 4.10. The greatest improvement in TAMSAT v3 is the reduced bias (-19.8 to -16.6mm in v2 compared to -1.5 to 1.3mm in v3). Although both versions of TAMSAT capture the general pattern of seasonal rainfall (pattern correlations > 0.9 for all seasons/datasets), TAMSAT v2 contains significant spatial artefacts. These are eliminated in TAMSAT v3.

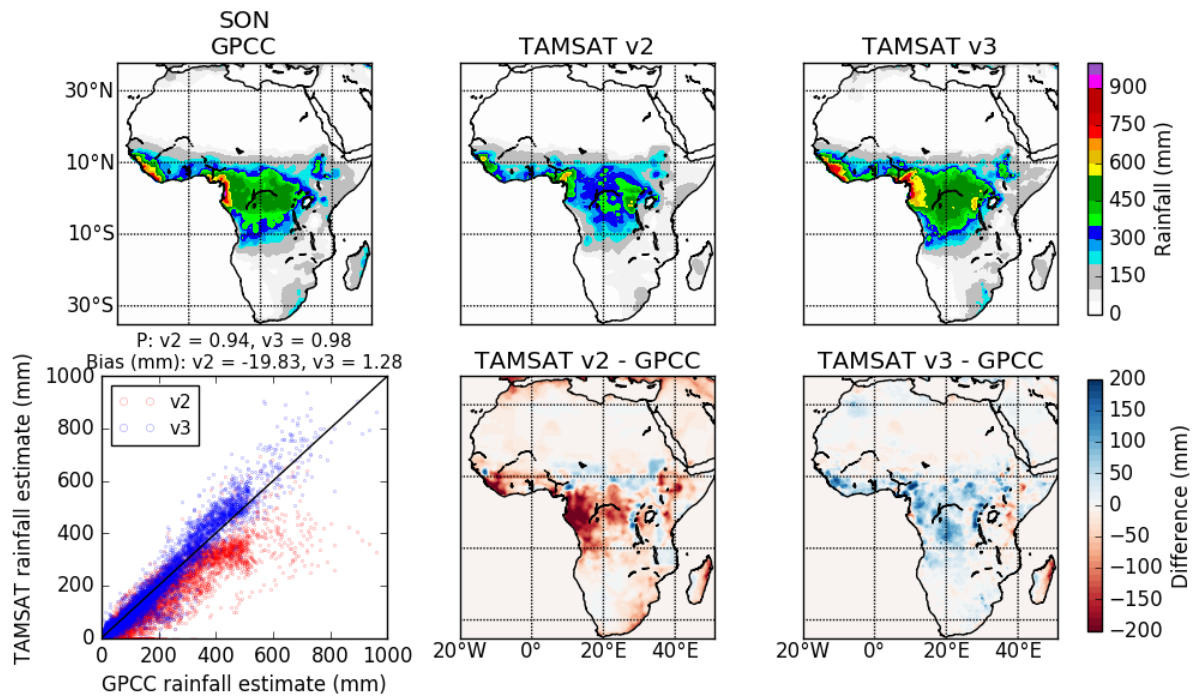


Figure 4.7. Comparison of seasonal mean rainfall during September – November (SON) estimated by TAMSAT v2, TAMSAT v3 and GPCC, 1983-2013. Statistics (Pearson’s correlation coefficient, P and bias) comparing TAMSAT v2 and v3 with GPCC are shown above the scatter plot.

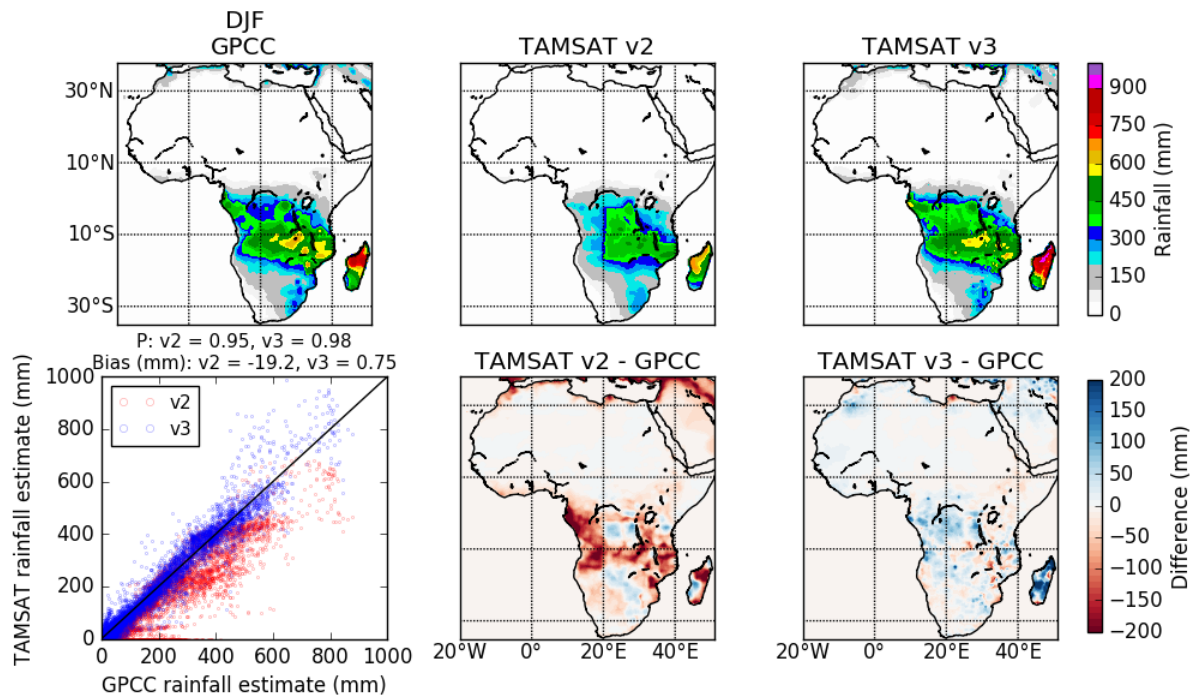


Figure 4.8. As for 4.7 but for DJF.

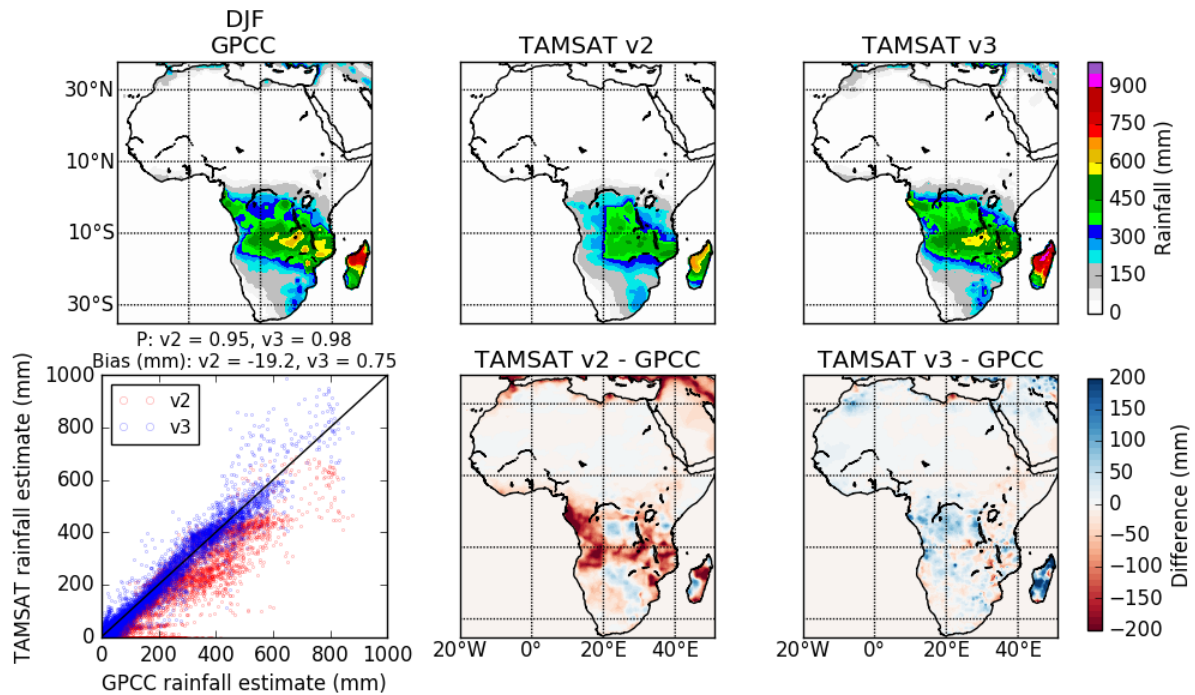


Figure 4.9 As for 4.7 but for MAM.

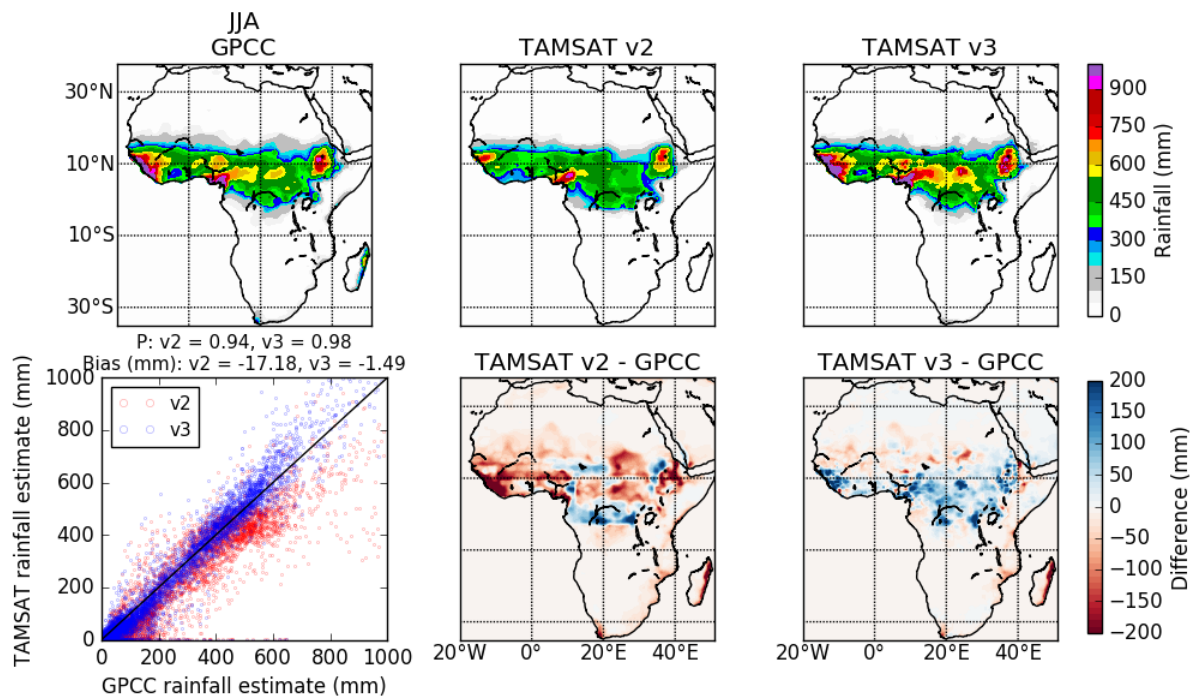


Figure 4.10 As for 4.7 but for JJA.

Figures 4.11 – 4.15 display seasonal and annual time series and statistics for all of Africa and for individual large regions. Tables 1 and 2 give statistical comparisons for annual and seasonal time series for all of Africa (for statistical comparisons over sub-regions see Appendix 1, Tables A1.1–A1.8). For all regions, the dry bias in TAMSAT v2 is reduced and the root mean square error, improved. TAMSAT v3 has more temporal variability than TAMSAT v2, as evidenced by the greater interannual standard deviation in the annual estimates. Comparison with GPCC indicates that TAMSAT v2 underestimates variability, and

the statistical comparisons in Table 2 show that this problem is reduced, if not eliminated, in TAMSAT v3. As with the climatologies, the greatest differences between TAMSAT v2/v3 and GPCC is over Central Africa. In TAMSAT v3, the v2 dry bias is replaced by a moderate wet bias, and temporal variability is overestimated. In other regions, during anomalously wet seasons, TAMSAT v3 captures rainfall magnitudes more accurately than TAMSAT v2. At this spatial scale, calibrating against the mean rather than the median in TAMSAT v3 does not obviously reduce skill in distinguish dry from very dry seasons. This may be because of improvements in the general skill of the method resulting from calibrating at pentadal/daily rather than dekadal time scales. However, more detailed evaluation at finer spatial scales would be necessary to confirm this (Appendix 2).

Table 1. Validation statistics comparing annual mean rainfall estimates over Africa from GPCC, TAMSAT v2 and TAMSAT v3 during 1983–2013.

Statistic	GPCC	TAMSAT v2	TAMSAT v3
Mean (mm)	269.5	197.6	268.9
SD (mm)	80.7	62.7	87.7
RMSE (mm)	-	400.0	2.9
Bias (mm)	-	-71.9	-0.5
Corr. (P)	-	0.99	0.99

Table 2. Validation statistics comparing seasonal mean rainfall estimates over Africa from GPCC, TAMSAT v2 and TAMSAT v3 during 1983 – 2013.

Statistic	DJF			MAM		
	GPCC	v2	v3	GPCC	v2	v3
Mean (mm)	83.2	59.0	85.1	78.0	58.9	78.0
SD (mm)	20.7	14.9	21.8	18.5	13.9	18.7
RMSE (mm)	-	102.8	8.1	-	85.4	0.04
Bias (mm)	-	-24.2	1.9	-	-19.1	-0.01
Corr. (P)	-	0.98	0.97	-	0.96	0.95

Statistic	JJA			SON		
	GPCC	v2	v3	GPCC	v2	V3
Mean (mm)	79.7	61.4	78.2	81.8	58.2	83.3
SD (mm)	16.8	13.0	16.9	19.0	13.6	20.0
RMSE (mm)	-	93.3	7.5	-	110.5	6.9
Bias (mm)	-	-18.2	-1.5	-	-23.6	1.5
Corr. (P)	-	0.95	0.94	-	0.96	0.95

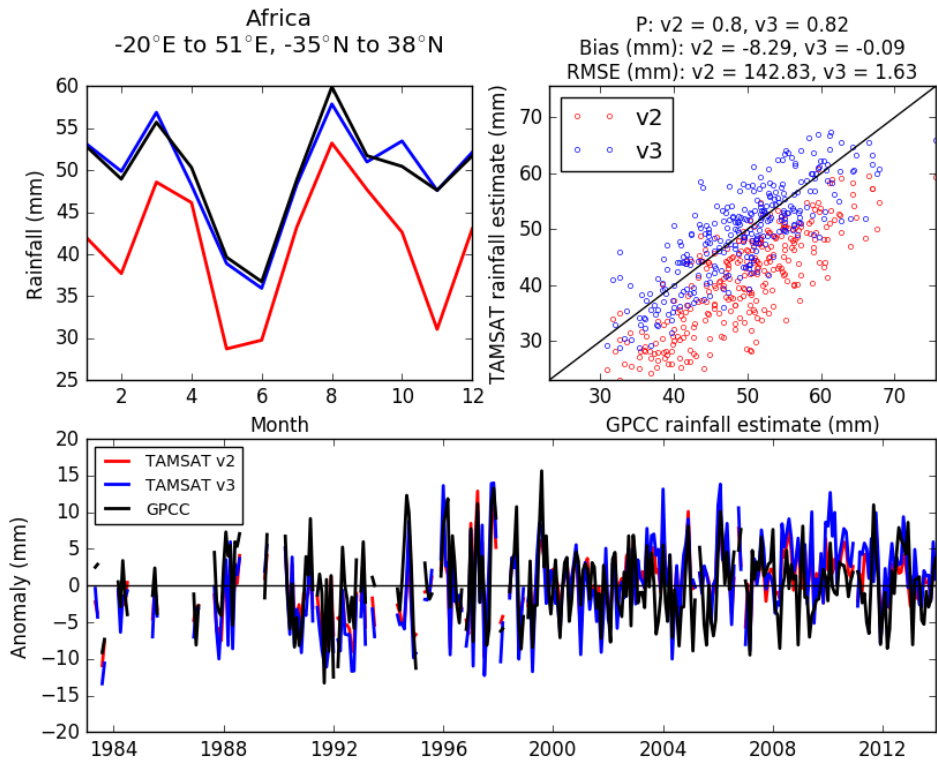


Figure 4.11. Time-series comparison of rainfall estimates from TAMSAT v2, TAMSAT v3 and GPCC over Africa, showing the annual cycle (top left), scatter plot of monthly areal-mean rainfall from TAMSAT (v2 and v3) against GPCC (top right) and time-series of monthly areal-mean rainfall anomalies (with respect to the corresponding monthly climatology of each dataset). Statistics (Pearson's correlation coefficient, P; bias and RMSE) comparing TAMSAT v2 and v3 with GPCC are shown above the scatter plot.

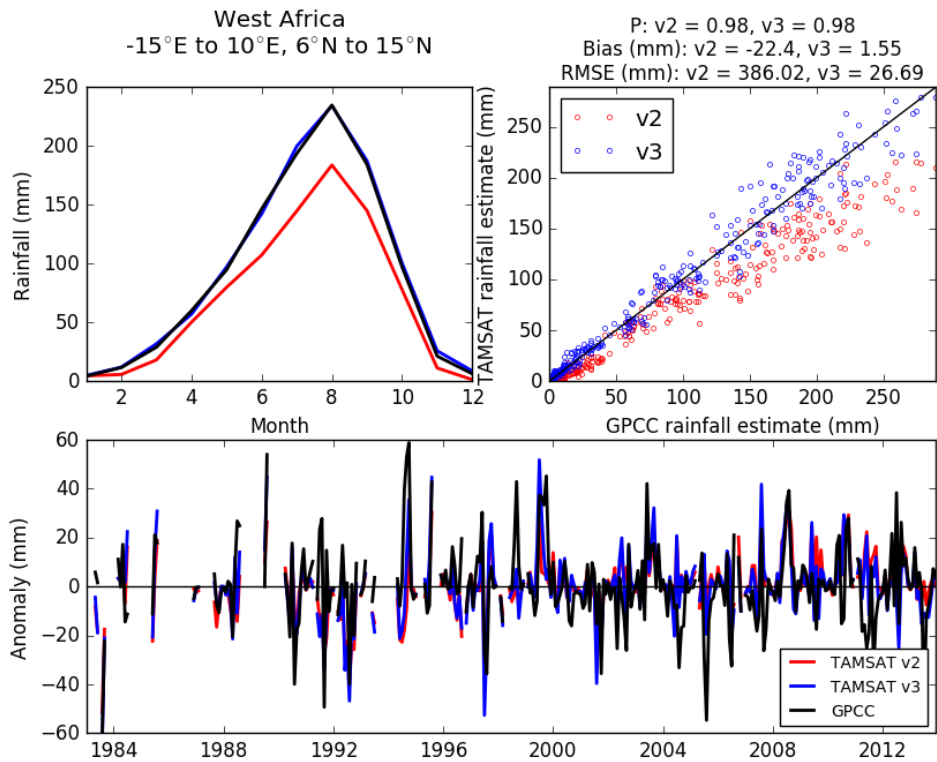


Figure 4.12. As in Fig. 4.11 but for West Africa.

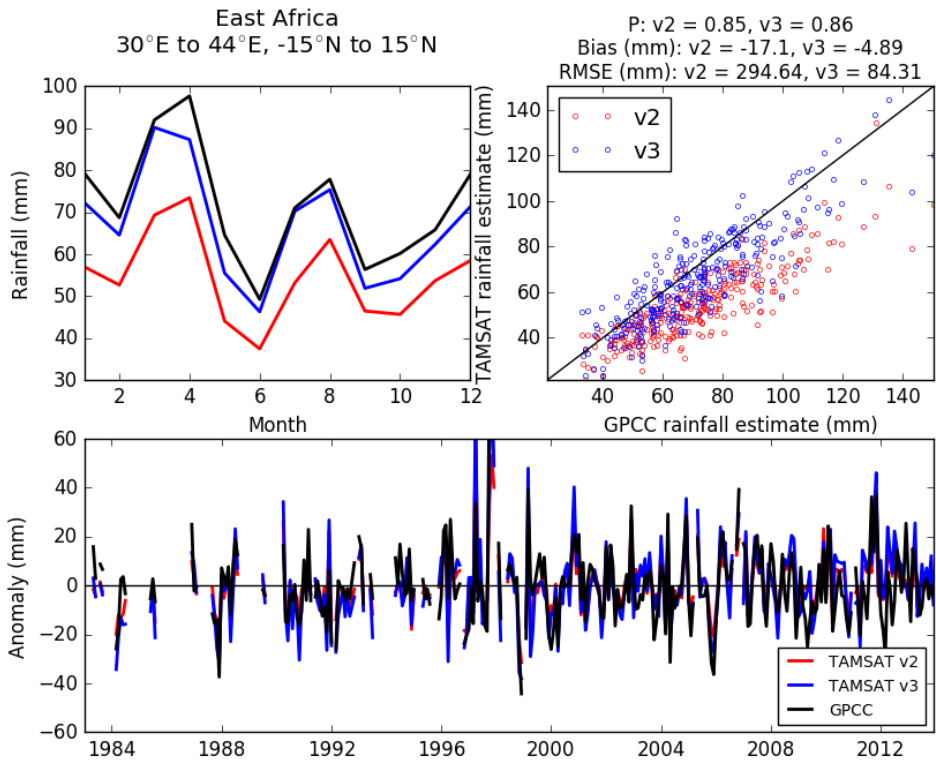


Figure 4.13. As in Fig. 4.11 but for East Africa.

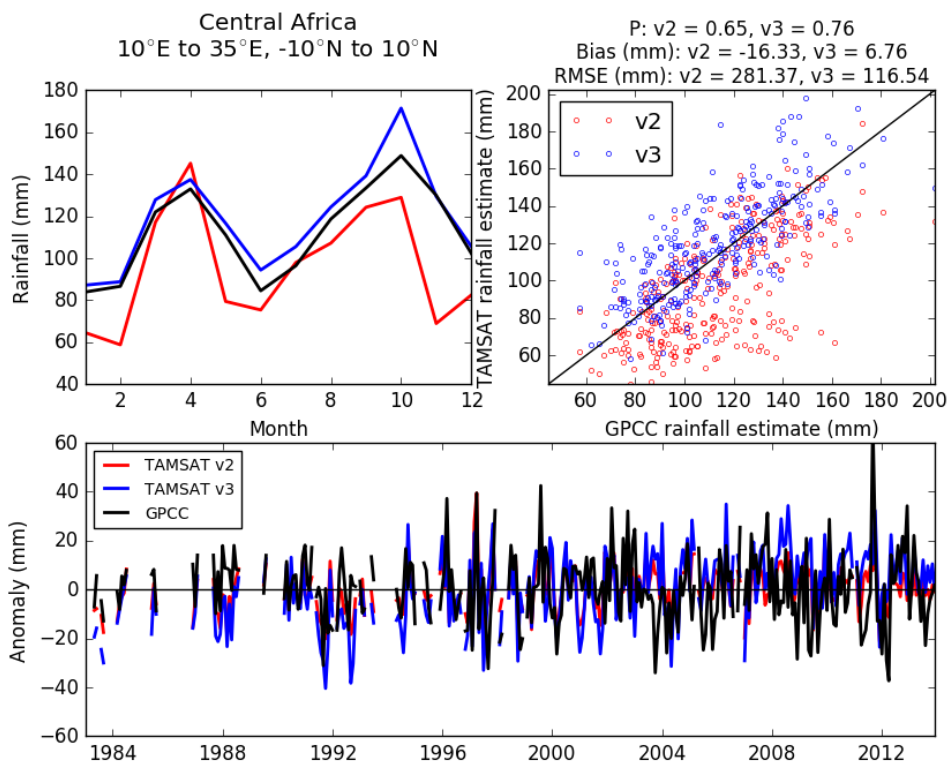


Figure 4.14. As in Fig. 4.11 but for Central Africa.

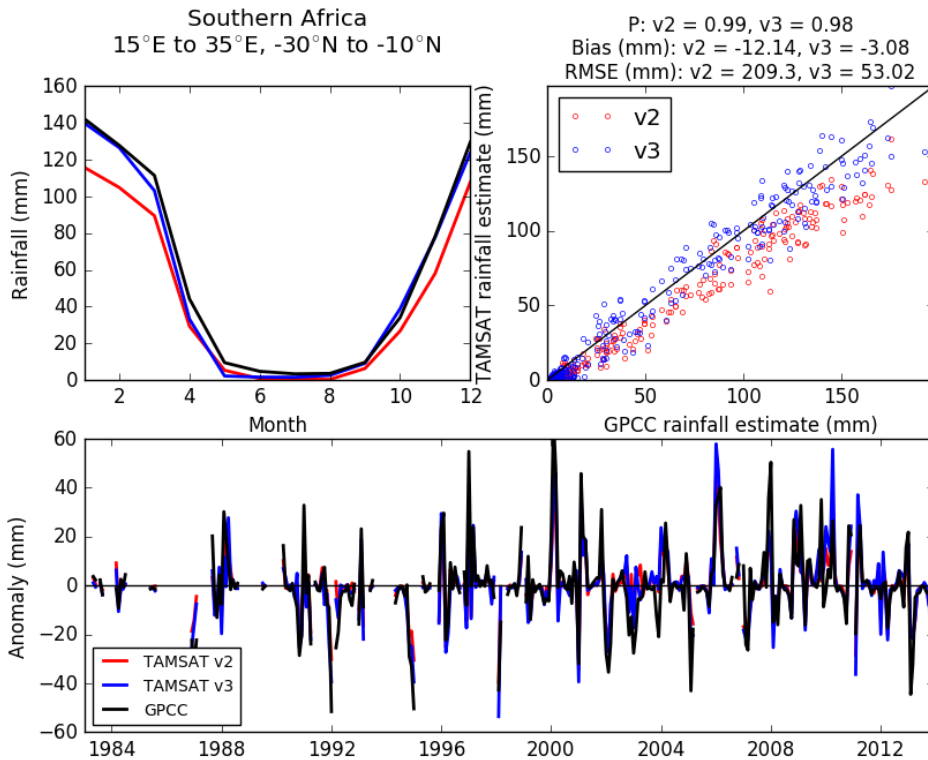


Figure 4.15. As in Fig. 4.11 but for Southern Africa.

5. Summary

The TAMSAT calibration method has been comprehensively assessed and revised. The main modifications are:

- Calibrating at the daily and pentadal, rather than dekadal time scales
- Calibrating CCD against mean rather than median rainfall
- Revision of the method for deriving the calibration regression parameters to avoid the use of rectangular calibration zones

As a result of these changes, TAMSAT v3 is a marked improvement on TAMSAT v2. In particular:

- Spatial artefacts, related to the use of rectangular calibration zones, have been eliminated
- Dry bias has been reduced

In keeping with TAMSAT's general approach, in version 3, calibration parameters vary both in space and through the seasonal cycle, and temporal variability (i.e. year-to-year) is determined solely by variation in CCD. Further validation and application case studies at a range of spatial and temporal scales are planned to establish TAMSAT v3's utility as an operational dataset.

Acknowledgments

This research was supported by the Joint Research Centre's Monitoring Agriculture with Remote Sensing Operationally (MARSOP4) programme (D5.8 Ad hoc development/improvements: calibration development). The TAMSAT group thank Helen Greatrex at the International Research Institute for Climate and Society (IRI), Columbia University, for inputs into this work and the Climate Hazards Group at the University of California, Santa Barbara for providing their quality controlled GTS gauge data for use in the development of TAMSAT version 3. We are endlessly grateful to the many meteorological services in Africa, who have contributed gauge data for TAMSAT calibration.

We gratefully acknowledge the University of Reading and the climate division of the National Centre for Atmospheric Science (NCAS-Climate) for their continued support of the TAMSAT programme.

References

Black, E., Tarnavsky, E., Maidment, R., Greatrex, H., Mookerjee, A., Quaife, T. and Brown, M., 2016. The use of remotely sensed rainfall for managing drought risk: a case study of weather index insurance in Zambia. *Remote Sensing*, 8(4), p.342.

Black, E., Greatrex, H., Maidment, R. and Young, M., 2016. Incorporating satellite data into weather index-based insurance. *Bulletin of the American Meteorological Society*, DOI: <http://dx.doi.org/10.1175/BAMS-D-16-0148.1>.

Funk, C., Verdin, A., Michaelsen, J., Peterson, P., Pedreros, D. and Husak, G., 2015. A global satellite assisted precipitation climatology. *Earth System Science Data Discussions*, 8(1).

Greatrex, H., Grimes, D. and Wheeler, T., 2014. Advances in the stochastic modeling of satellite-derived rainfall estimates using a sparse calibration dataset. *Journal of Hydrometeorology*, 15(5), pp.1810-1831.

Maidment, R.I., 2013. *Development and exploitation of a 30-year African rainfall climatology and time-series* (Doctoral dissertation, University of Reading).

Maidment, R.I., Grimes, D.I., Allan, R.P., Greatrex, H., Rojas, O. and Leo, O., 2013b. Evaluation of satellite-based and model re-analysis rainfall estimates for Uganda. *Meteorological Applications*, 20(3), pp.308-317.

Maidment, R.I., Grimes, D., Allan, R.P., Tarnavsky, E., Stringer, M., Hewison, T., Roebeling, R. and Black, E., 2014. The 30 year TAMSAT African rainfall climatology and time series (TARCAT) data set. *Journal of Geophysical Research: Atmospheres*, 119(18).

Maidment, R.I., Allan, R.P. and Black, E., 2015. Recent observed and simulated changes in precipitation over Africa. *Geophysical Research Letters*, 42(19), pp.8155-8164.

Milford, J.R., McDougall, V.D. and Dugdale, G., 1994, December. Rainfall estimation from cold cloud duration, experience of the TAMSAT group in West Africa. In *Validation Problems*

of Rainfall Estimation by Satellite in Intertropical Africa, Guillot B., ed., Proc. Niamey workshop (pp. 1-3).

Schneider, Udo; Becker, Andreas; Finger, Peter; Meyer-Christoffer, Anja; Rudolf, Bruno; Ziese, Markus (2015): GPCP Full Data Reanalysis Version 7.0 at 0.5°: Monthly Land-Surface Precipitation from Rain-Gauges built on GTS-based and Historic Data. DOI: 10.5676/DWD_GPCP/FD_M_V7_050

Tarnavsky, E., Grimes, D., Maidment, R., Black, E., Allan, R.P., Stringer, M., Chadwick, R. and Kayitakire, F., 2014. Extension of the TAMSAT satellite-based rainfall monitoring over Africa and from 1983 to present. *Journal of Applied Meteorology and Climatology*, 53(12), pp.2805-2822

Washington, R., James, R., Pearce, H., Pokam, W.M. and Moufouma-Okia, W., 2013. Congo Basin rainfall climatology: can we believe the climate models?. *Phil. Trans. R. Soc. B*, 368(1625), p.20120296.

Appendix 1: Additional figures and statistical tables

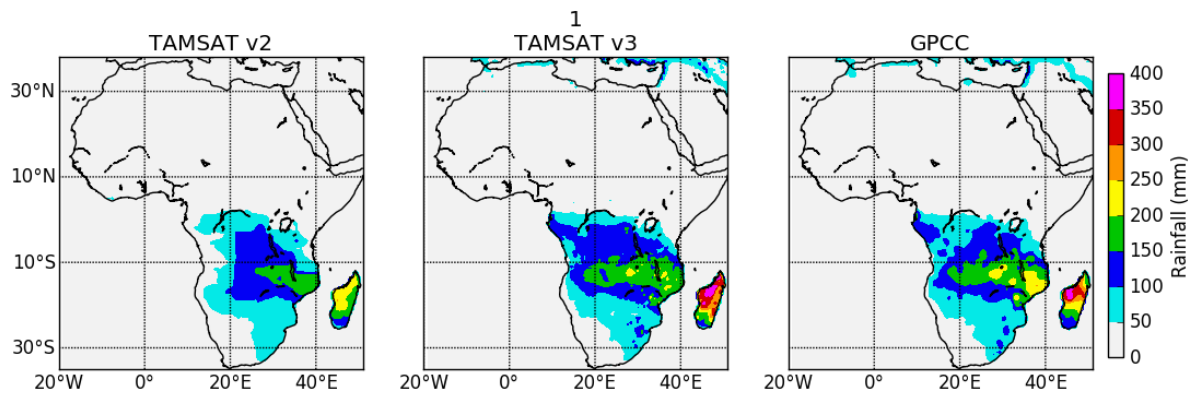


Figure A1.1. January mean rainfall estimated by TAMSAT v2, TAMSAT v3 and GPCCC, 1983–2013.

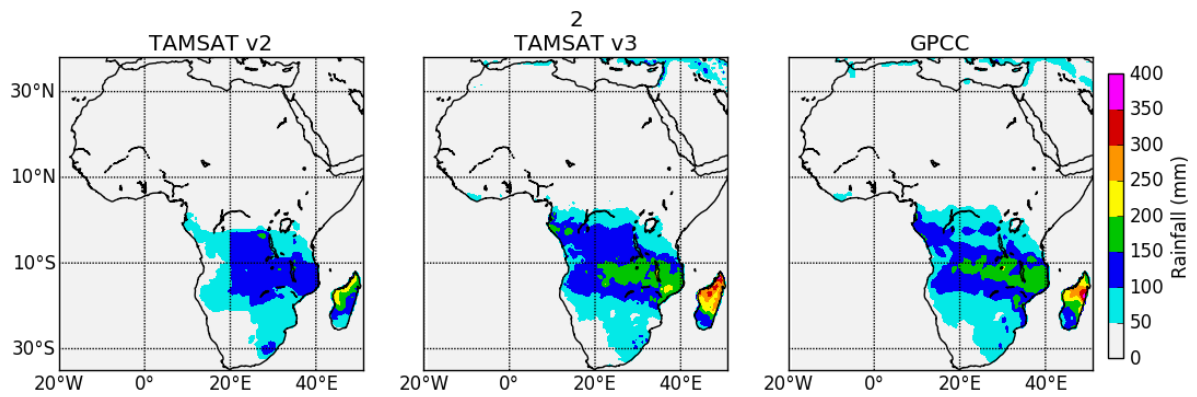


Figure A1.2. February mean rainfall estimated by TAMSAT v2, TAMSAT v3 and GPCCC, 1983–2013.

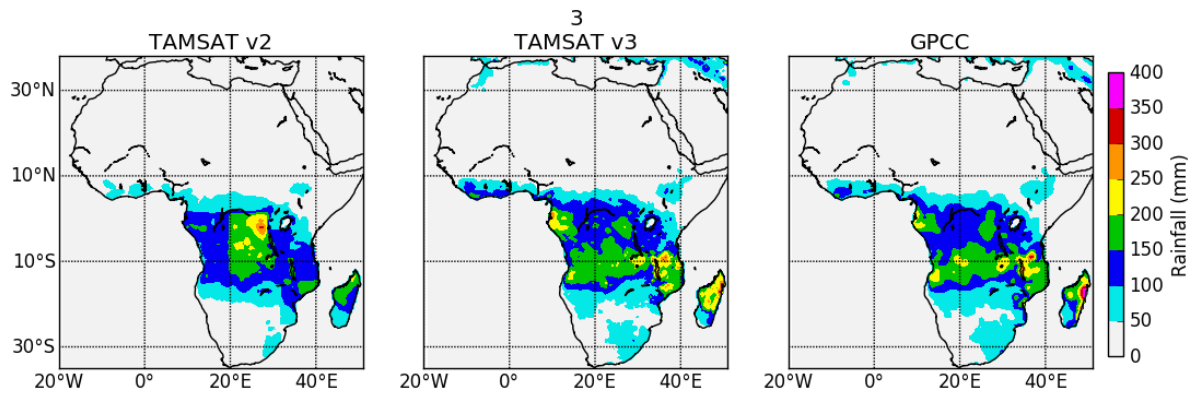


Figure A1.3. March mean rainfall estimated by TAMSAT v2, TAMSAT v3 and GPCCC, 1983–2013.

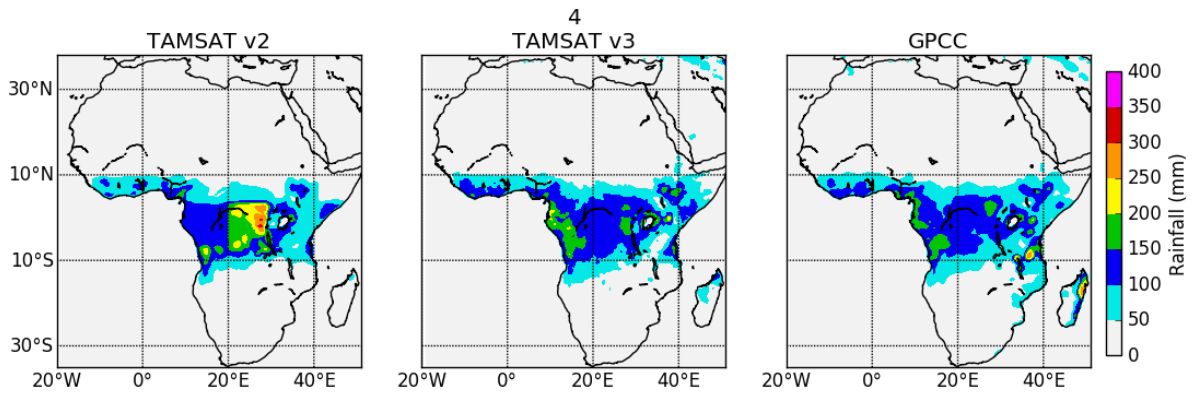


Figure A1.4. April mean rainfall estimated by TAMSAT v2, TAMSAT v3 and GPCC, 1983–2013.

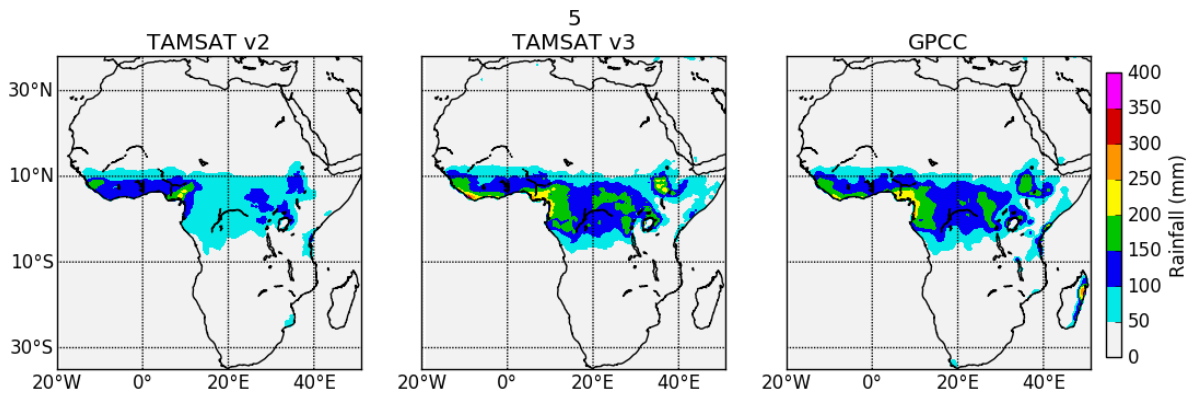


Figure A1.5. May mean rainfall estimated by TAMSAT v2, TAMSAT v3 and GPCC, 1983–2013.

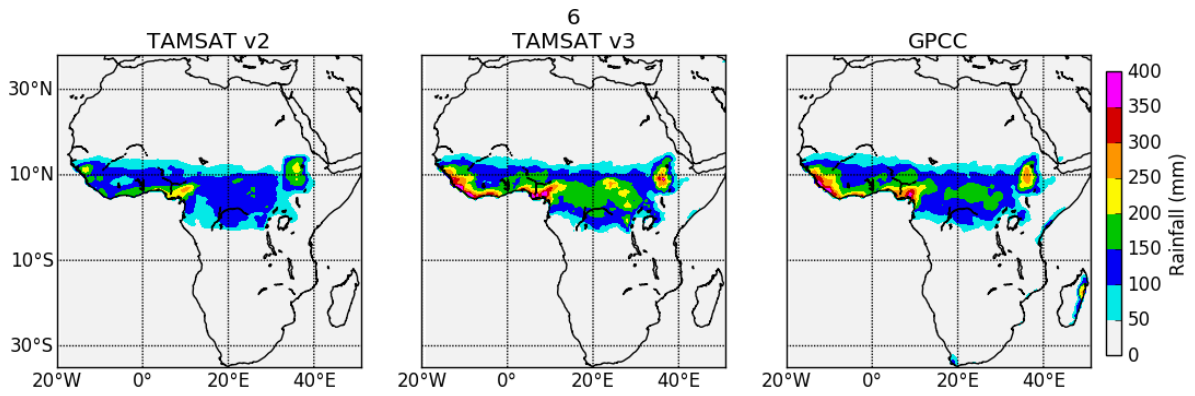


Figure A1.6. June mean rainfall estimated by TAMSAT v2, TAMSAT v3 and GPCC, 1983–2013.

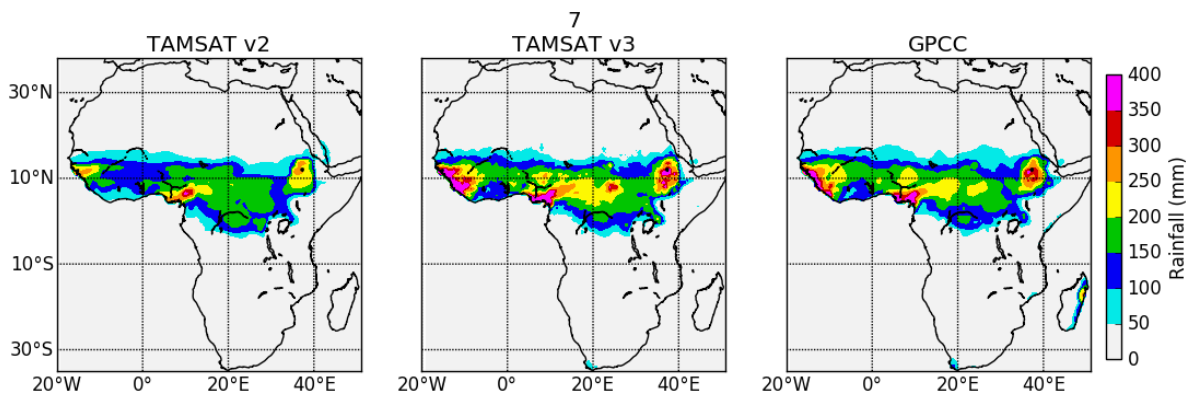


Figure A1.7. July mean rainfall estimated by TAMSAT v2, TAMSAT v3 and GPCC, 1983–2013.

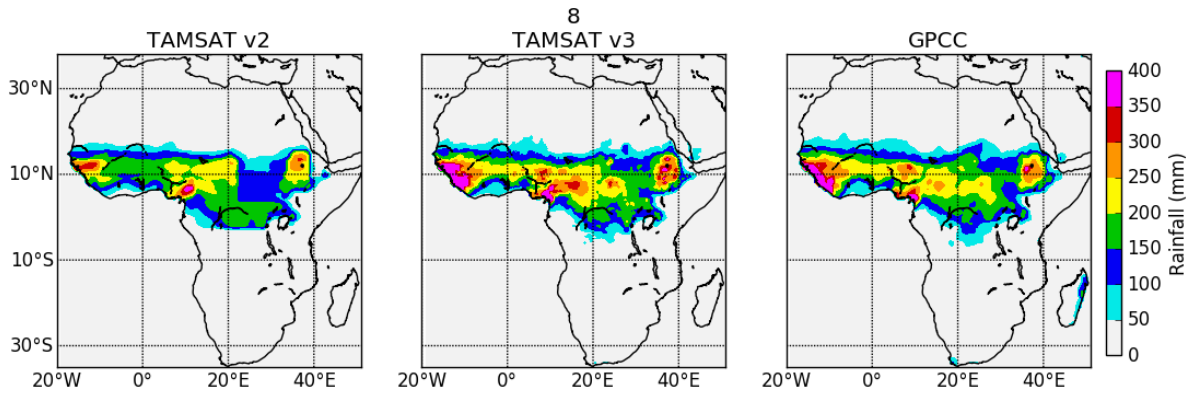


Figure A1.8. August mean rainfall estimated by TAMSAT v2, TAMSAT v3 and GPCC, 1983–2013.

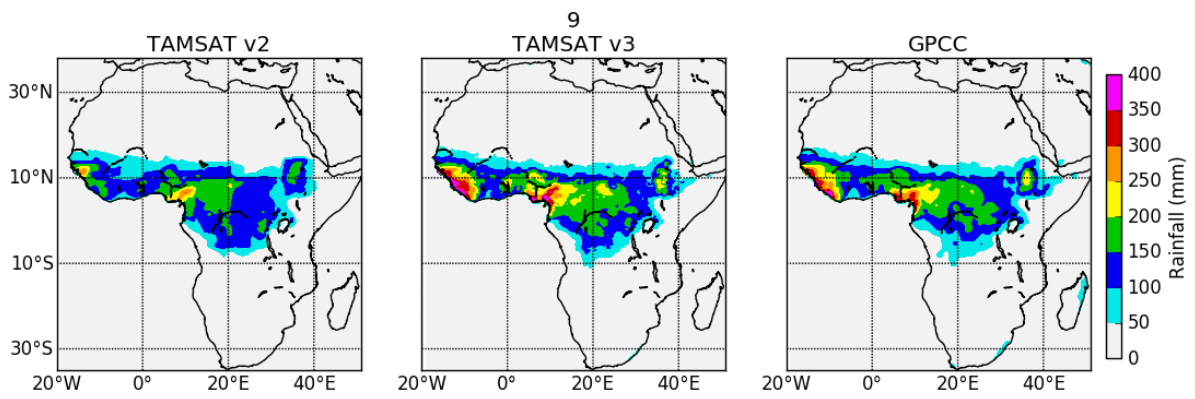


Figure A1.9. September mean rainfall estimated by TAMSAT v2, TAMSAT v3 and GPCC, 1983–2013.

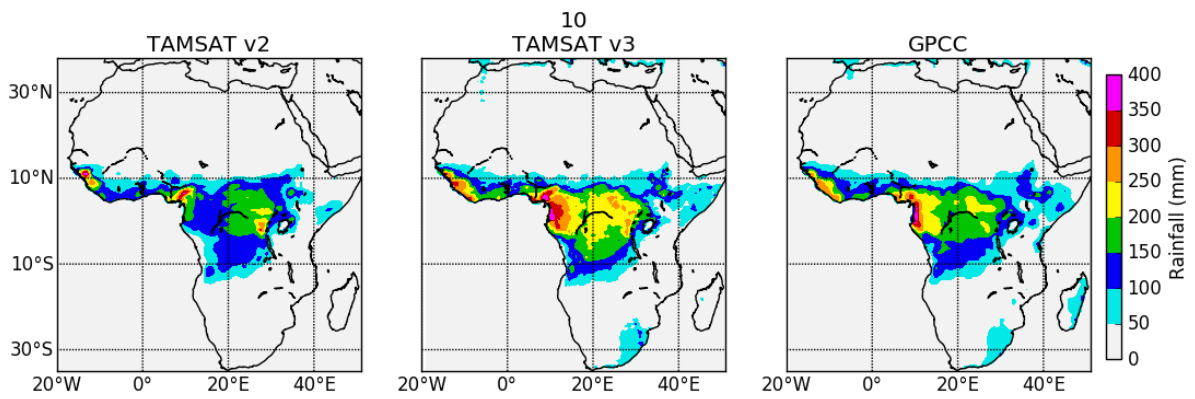


Figure A1.10. October mean rainfall estimated by TAMSAT v2, TAMSAT v3 and GPCC, 1983–2013.

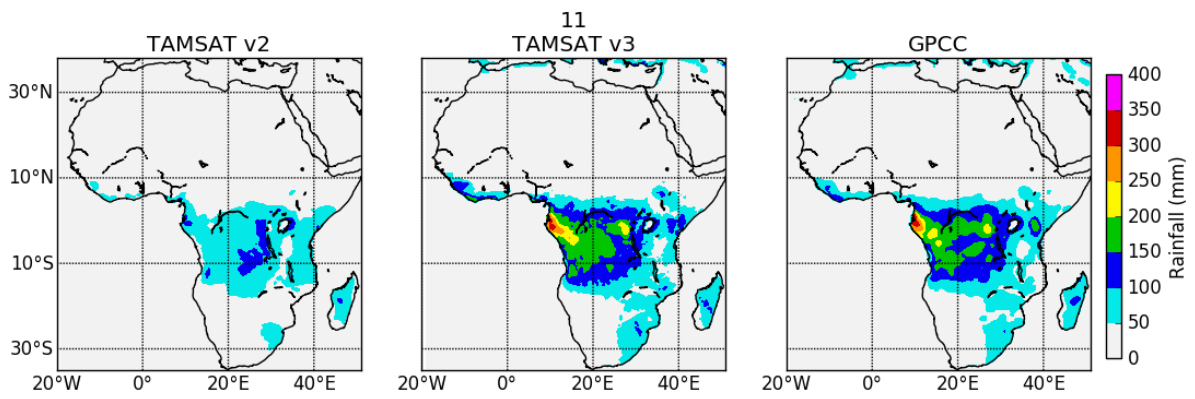


Figure A1.11. November mean rainfall estimated by TAMSAT v2, TAMSAT v3 and GPCC, 1983–2013.

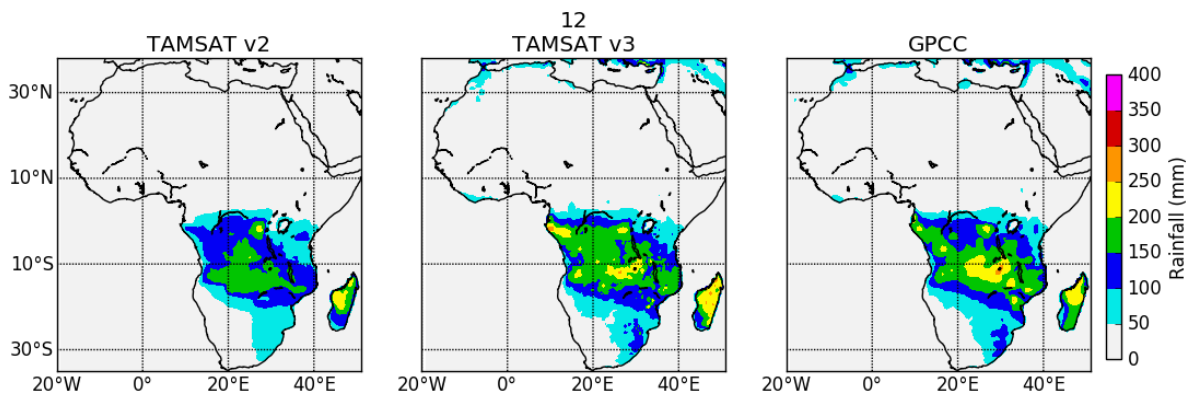


Figure A1.12. December mean rainfall estimated by TAMSAT v2, TAMSAT v3 and GPCC, 1983–2013.

Table 1. Validation statistics comparing annual mean rainfall estimates over Africa from GPCC, TAMSAT v2 and TAMSAT v3 during 1983–2013.

Table A1.1. Validation statistics comparing annual mean rainfall estimates over West Africa from GPCC, TAMSAT v2 and TAMSAT v3 during 1983–2013.

Statistic	GPCC	TAMSAT v2	TAMSAT v3
Mean (mm)	860.7	658.3	874.7
SD (mm)	235.4	193.6	242.2
RMSE (mm)	-	1127.0	77.9
Bias (mm)	-	-202.4	14.0
Corr. (P)	-	0.94	0.96

Table A1.2. Validation statistics comparing seasonal mean rainfall estimates over West Africa from GPCC, TAMSAT v2 and TAMSAT v3 during 1983 – 2013.

Statistic	DJF			MAM		
	GPCC	v2	v3	GPCC	v2	v3
Mean (mm)	19.3	10.5	22.4	163.3	133.7	166.8
SD (mm)	8.5	5.3	8.2	40.6	32.5	39.5
RMSE (mm)	-	37.3	13.2	-	132.5	15.8
Bias (mm)	-	-8.8	3.1	-	-29.6	3.5
Corr. (P)	-	0.72	0.86	-	0.88	0.91

Statistic	JJA			SON		
	GPCC	v2	v3	GPCC	v2	V3
Mean (mm)	522.8	397.0	523.9	276.3	214.5	286.6
SD (mm)	111.7	86.3	112.9	72.2	53.1	67.6
RMSE (mm)	-	641.5	5.6	-	289.5	48.7
Bias (mm)	-	-125.8	1.1	-	-61.7	10.4
Corr. (P)	-	0.90	0.94	-	0.83	0.90

Table A1.3. Validation statistics comparing annual mean rainfall estimates over East Africa from GPCC, TAMSAT v2 and TAMSAT v3 during 1983–2013.

Statistic	GPCC	TAMSAT v2	TAMSAT v3
Mean (mm)	579.5	438.3	539.8
SD (mm)	180.3	147.8	186.3
RMSE (mm)	-	786.4	221.3
Bias (mm)	-	-141.2	-39.8
Corr. (P)	-	0.99	0.98

Table A1.4. Validation statistics comparing seasonal mean rainfall estimates over East Africa from GPCC, TAMSAT v2 and TAMSAT v3 during 1983 – 2013.

Statistic	DJF			MAM		
	GPCC	v2	v3	GPCC	v2	v3
Mean (mm)	178.4	132.8	166.3	199.7	147.5	184.3
SD (mm)	49.3	35.9	44.2	51.2	38.3	49.8
RMSE (mm)	-	193.8	51.7	-	233.4	68.6
Bias (mm)	-	-45.7	-12.2	-	-52.2	-15.3
Corr. (P)	-	0.97	0.97	-	0.90	0.89

Statistic	JJA			SON		
	GPCC	v2	v3	GPCC	v2	V3
Mean (mm)	161.4	126.3	158.5	148.6	119.0	138.3
SD (mm)	36.0	28.3	37.0	47.9	34.4	47.0
RMSE (mm)	-	179.0	14.8	-	138.6	48.3
Bias (mm)	-	-35.1	-2.9	-	-29.6	-10.3
Corr. (P)	-	0.91	0.90	-	0.97	0.97

Table A1.5. Validation statistics comparing annual mean rainfall estimates over Central Africa from GPCC, TAMSAT v2 and TAMSAT v3 during 1983–2013.

Statistic	GPCC	TAMSAT v2	TAMSAT v3
Mean (mm)	1033.1	883.3	1095.1
SD (mm)	304.3	267.0	354.0
RMSE (mm)	-	833.9	62.0
Bias (mm)	-	-149.8	-62.0
Corr. (P)	-	0.98	0.97

Table A1.6. Validation statistics comparing seasonal mean rainfall estimates over Central Africa from GPCC, TAMSAT v2 and TAMSAT v3 during 1983 – 2013.

Statistic	DJF			MAM		
	GPCC	v2	v3	GPCC	v2	v3
Mean (mm)	249.0	189.0	259.7	331.1	310.7	349.9
SD (mm)	63.7	49.6	68.7	81.3	74.3	84.8
RMSE (mm)	-	254.3	45.5	-	91.3	83.7
Bias (mm)	-	-59.9	10.7	-	-20.4	18.7
Corr. (P)	-	0.88	0.86	-	0.94	0.91

Statistic	JJA			SON		
	GPCC	v2	v3	GPCC	v2	V3
Mean (mm)	274.2	258.4	299.8	379.3	294.8	404.7
SD (mm)	59.3	54.0	67.0	88.7	67.2	95.9
RMSE (mm)	-	80.5	130.7	-	396.5	19.3
Bias (mm)	-	-15.8	25.6	-	-84.5	25.4
Corr. (P)	-	0.94	0.88	-	0.92	0.89

Table A1.7. Validation statistics comparing annual mean rainfall estimates over Southern Africa from GPCC, TAMSAT v2 and TAMSAT v3 during 1983–2013.

Statistic	GPCC	TAMSAT v2	TAMSAT v3
Mean (mm)	500.4	389.6	472.3
SD (mm)	210.7	164.6	202.0
RMSE (mm)	-	616.6	156.2
Bias (mm)	-	-110.7	-28.1
Corr. (P)	-	0.99	0.99

Table A1.8. Validation statistics comparing seasonal mean rainfall estimates over Southern Africa from GPCC, TAMSAT v2 and TAMSAT v3 during 1983 – 2013.

Statistic	DJF			MAM		
	GPCC	v2	v3	GPCC	v2	v3
Mean (mm)	367.5	304.4	362.2	152.2	114.6	128.7
SD (mm)	99.9	78.9	94.5	45.1	35.3	42.5
RMSE (mm)	-	267.6	22.7	-	168.5	105.2
Bias (mm)	-	-63.1	-5.4	-	-37.7	-23.5
Corr. (P)	-	0.95	0.95	-	0.94	0.93

Statistic	JJA			SON		
	GPCC	v2	v3	GPCC	v2	V3
Mean (mm)	10.3	1.4	5.1	107.7	81.2	112.7
SD (mm)	4.7	1.5	3.6	29.6	20.2	27.9
RMSE (mm)	-	45.7	26.6	-	124.6	23.2
Bias (mm)	-	-9.0	-5.2	-	-26.6	4.9
Corr. (P)	-	0.82	0.87	-	0.92	0.90

Appendix 2: Assessment of alternative calibration methods

Here we assess the most appropriate linear regression methodology (henceforth referred to as ‘calibration method’) and aggregation length for CCD and rainfall (henceforth referred to as ‘calibration timescale’) for the development of TAMSAT v3.0. The study reported in this appendix is based on TAMSAT rainfall estimates using gauge–CCD pairs over Ghana. Additional analyses were carried out for Zambia and Ethiopia, with similar results (not shown).

First, the data and calibration methods are described. Then an initial sensitivity study of the methods and timescales is conducted using observations at Tamale (07005TLE) in northeastern Ghana during September. Based on initial assessments at Tamale, we then present results investigating the performance of the methods and timescales over the whole of Ghana.

a. Data

Daily rain gauge measurements from of 22 stations spanning 1983–2011 from the Ghana meteorological agency are used to calibrate and validate the different calibration methods (Fig. A2.1). CCD at five TIR temperature thresholds (–20, –30, –40, –50 and –60°C) is derived from observations of cloud top temperature retrieved every 15-min from the Spinning Enhanced Visible and Infrared Radiometer (SEVIRI) 10.8 μm channel on-board the geostationary Meteosat satellite. Each daily station measurement is collocated with the nearest daily CCD observation to make a daily gauge-CCD pair. In order to account for the spatial difference between the point gauge measurements and areal coverage of the satellite pixel, the gauge measurements in each gauge-CCD pair are spatially interpolated to the nominal SEVIRI pixel resolution of 0.0375° using block-kriging. Additionally, all daily gauge-CCD pairs are accumulated to pentadal (5 days) and dekadal (10 days) time periods to investigate the optimal time window for calibration. To conduct an independent validation, Gauge-CCD pairs from 1983 to 2004 are first used for calibration and then observations for the remaining 6-year period (2005–2011) are used for validation.

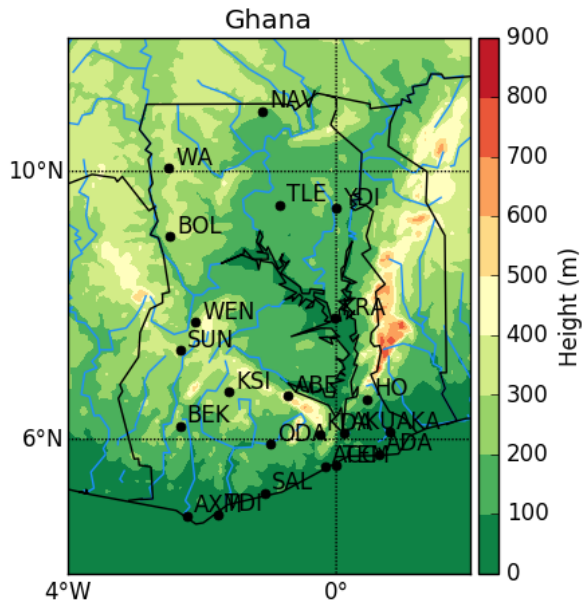


Figure A2.1. Topographic map of Ghana, showing the stations used to calibrate and validate each calibration method. Tamale (TLE) is located in the center of the northern region.

b. Calibration Methods

To improve the ability of the TAMSAT algorithm to estimate rainfall amount, we assess and compare four calibration methods (Table A2.1).

Table A2.1. Names and descriptions of each calibration method.

Name	LR	MLR	LR PC1	MLR PC1 + PC2
Method	Linear regression on CCD at the dominant threshold	Multiple linear regression on CCD at all thresholds	Linear regression on the first principal component of CCD	Multiple linear regression using the first and second principal components

Note that all methods use the same method to determine rainfall occurrence; that is, using the occurrence of CCD greater than zero at the optimal TIR rain/no-rain threshold. Here, the optimal TIR rain/no-rain threshold is selected using gauge-CCD pairs at the *daily* time scale (as used in TAMSAT v3) rather than *dekadal* timescale as used in the original TAMSAT calibration.

1. Linear regression of CCD at the optimal temperature threshold (–20, –30, –40, –50 or –60°C) against rainfall. [LR in Table A2.1]

Specifically, this linear regression is conducted by grouping CCD values into discrete bins and regressing the mean CCD against the mean rainfall in each CCD bin. The regression is weighted by the number of gauge-CCD pairs in each bin. This method is analogous to the current TAMSAT method except that it uses the mean rather than the median rainfall in

each CCD bin for the regression, to help reduce the current dry bias present in TAMSAT as explained previously. An example of a dekadal calibration is shown in Fig. A2.2 for gauge-CCD observations during September at Tamale, Ghana at the optimal temperature threshold of -30°C . This figure emphasises the well-defined linear correlation between rainfall amount and CCD, highlighting both the simplicity and strength in this method for rainfall estimation.

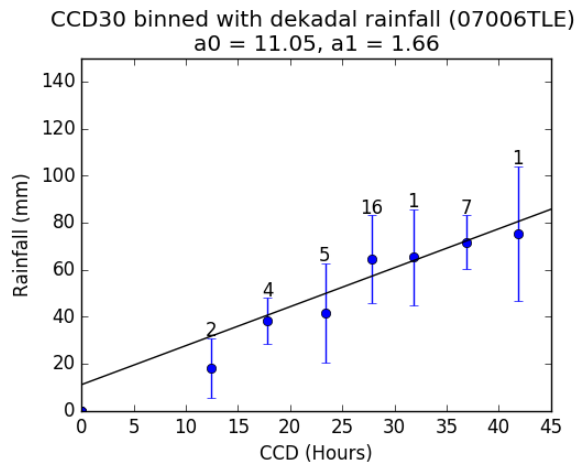


Figure A2.2. Relationship between dekadal rainfall (mm) and CCD (hours) below -30°C during September 1984–2004 at Tamale, Ghana. The mean rainfall, standard deviation and number of samples within each CCD bin are represented by the circles, whiskers and numbers respectively. The line of best fit represents the linear regression between CCD and the mean rainfall in each CCD bin, where a_0 and a_1 are the intercept and slope parameters in the regression.

2. Multiple linear regression of CCD at all temperature thresholds to rainfall [MLR in Table A2.1]

The purpose of testing a multiple-linear regression is to ascertain whether CCD at multiple thresholds provides more information of rainfall amount. Unlike the standard method, there is no binning of CCD and rainfall, and thus the multiple-linear regression is performed on all gauge-CCD pairs such that:

$$R = a \text{ CCD20} + b \text{ CCD30} + c \text{ CCD40} + d \text{ CCD50} + e \text{ CCD60} + f$$

Where R is rainfall in mm, $a - f$ are coefficients obtained from the regression and CCDXX is the CCD observation at a given temperature threshold $-XX$ (i.e. -20° , -30° , ..., -60°).

3. Linear regression of the principal component of CCD at multiple thresholds against rainfall. [LR PC1 and MLR PC1 + 2 in Table A2.1]

This method first conducts a principal component analysis (PCA) on CCD observations at the 5 thresholds. An example of the PCA is given by Fig. A2.3 showing the proportion of variance explained from each principal component of CCD during September at Tamale in Ghana. The fact that most of the variability ($> 80\%$) is contained in PC1 is somewhat unsurprising because the CCD at each threshold contains a significant amount of co-variability (i.e. if

there is CCD at the coldest threshold of -60°C , there will also be CCD observed at every other threshold). Furthermore, the first principal component shows a clear dependence on rainfall in comparison to the other three principle components (Fig. A2.4). This rainfall dependence illustrates the potential strength of using the PCA to reduce the dimensions of the multiple threshold CCD field for rainfall estimation.

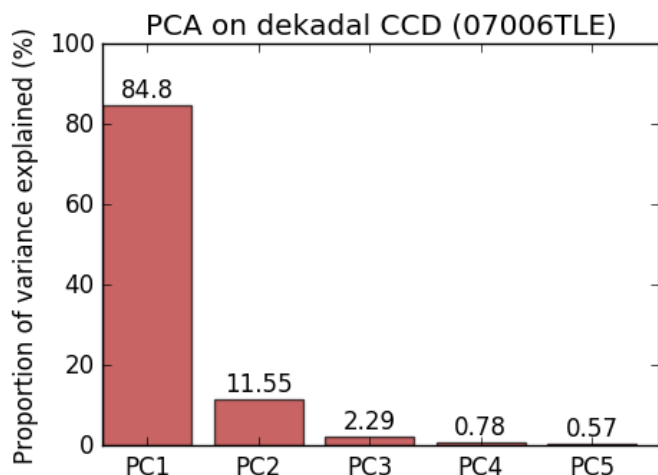


Figure A2.3 Proportion of variance explained (%) for the principal components of Dekadal CCD at multiple thresholds (-20° , -30° , -40° , -50° , -60°C) during during September 1989–2004 at Tamale, Ghana. The number above each box is the proportion of variance explained in each principal component.

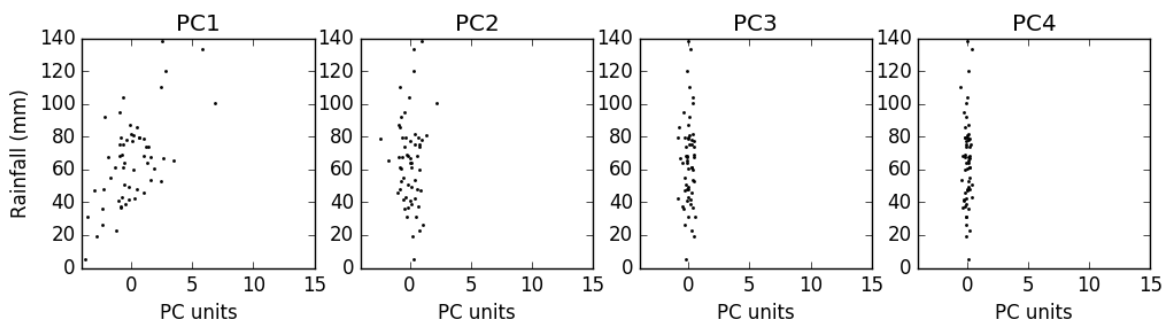


Figure A2.4. Relationship of each principal component (PC1 to PC4) of Dekadal CCD at multiple thresholds (-20° , -30° , -40° , -50° , -60°C) to gauge observed rainfall during September 1989–2004 at Tamale, Ghana.

PC1 can be regressed against rainfall in the same way as the standard method (Figure A2.5). For this case the regression is conducted by transforming CCD at the 5 thresholds into the 1-dimensional PC1 space and binning PC1 with gauge rainfall. We also perform a multiple-linear regression using both PC1 and PC2 in order to test the effect of the second principle component.

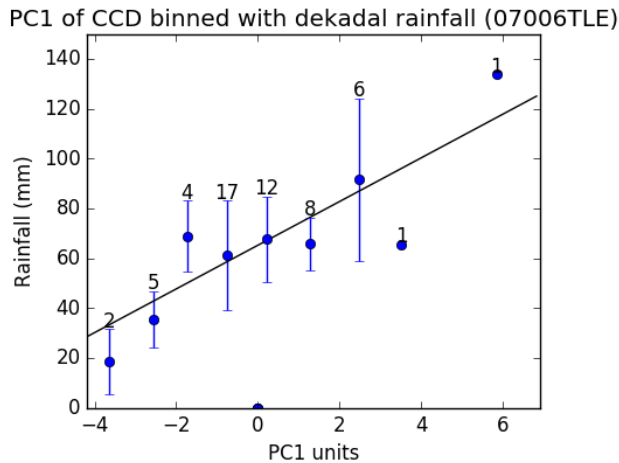


Figure A2.5. Relationship between Dekadal rainfall (mm) and PC1 during September 1989–2004 at Tamale, Ghana. The mean rainfall, standard deviation and number of samples within each PC1 bin are represented by the circles, whiskers and numbers respectively. The line of best fit represents the linear regression between PC1 and the mean rainfall in each PC1 bin.

c. Results

Method Performance

As an initial sensitivity study, each calibration method is evaluated against the gauge observations at Tamale during September, 2005–2011. For the purposes of the validation, Tamale has been removed from the calibration. This station is selected for its low numbers of missing data and the month of September is the height of the wet season, providing a large number of wet days to both calibrate and validate each method.

Overall, the scatter plots and statistics presented in Fig. A2.6 show that both the standard method (LR CCD) and linear regression of the first principal component of CCD (LR PC1) perform best at all timescales. Interestingly, the LR CCD performs best at the pentadal scale, with the lowest RMSE and bias relative to the other methods at all timescales. The better accuracy of the LR CCD pentadal calibration relative to the dekadal calibration shown here, hints that a pentadal calibration using the standard method could be highly appropriate for improving TAMSAT rainfall estimates. However, at the daily scale, the LR PC1 method has the highest accuracy, illustrating the strength of utilising information from all CCD thresholds for daily rainfall estimation. In comparison, both multiple-linear regression methods (MLR CCD and MLR PC1+PC2) perform poorly, particularly at the daily scale. The MLR CCD tends to substantially overestimate rainfall, while the MLR PC1+PC2 substantially underestimates rainfall.

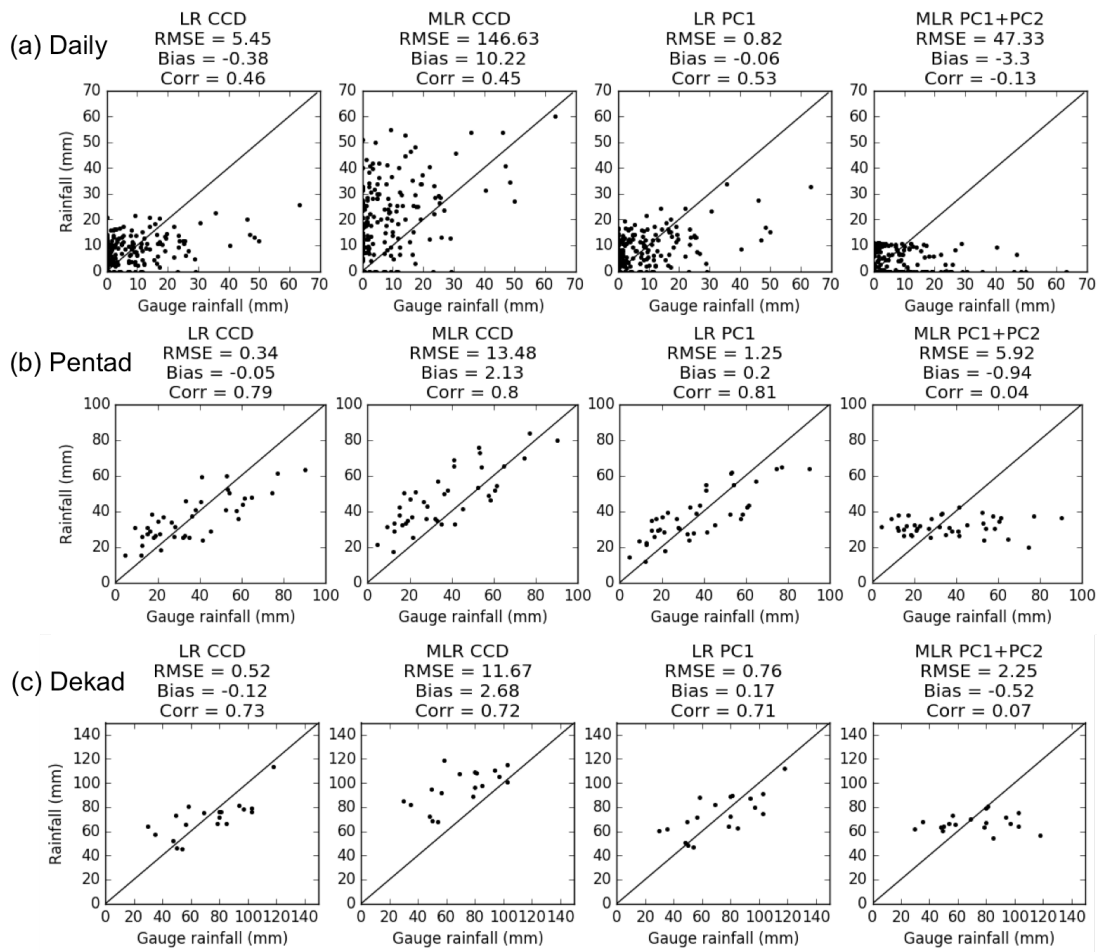


Figure A2.6 Scatter plots comparing (a) daily, (b) pentad and (c) dekadal rainfall estimates from each calibration method to rain gauge observations at Tamale, Ghana during September 2005–2011. Statistics above each scatterplot are the root-mean-square error (RMSE; mm d⁻¹); Bias (mm d⁻¹) and linear correlation (Corr).

These features can also be clearly identified in the timeseries in Fig. A2.7; the LR CCD and LR PC1 methods have closest agreement with the gauge data at all timescales, but have difficulty capturing heavy rainfall events (> 20 mm) at the daily scale. Conversely, the substantial overestimation by the MLR CCD is pronounced at the daily (and dekadal) timescale, meaning that occasionally it captures the heavier daily rainfall events, but in general shows no coherent estimation skill. The poor skill by MLR CCD further suggests that the method is over-fitted and captures too much noise rather than a coherent rainfall signal. However, the fact that the estimates from this method co-vary like the LR CCD and LR PC1 methods, illustrates the strong covariance in CCD at all thresholds. In contrast to the MLR CCD method, the variability in the MLR PC1+PC2 is highly reduced, and sometimes contradictory to the other methods, suggesting that PC2 primarily contains noise that dampens the signal from PC1 when both PC1 and PC2 are combined in the regression.

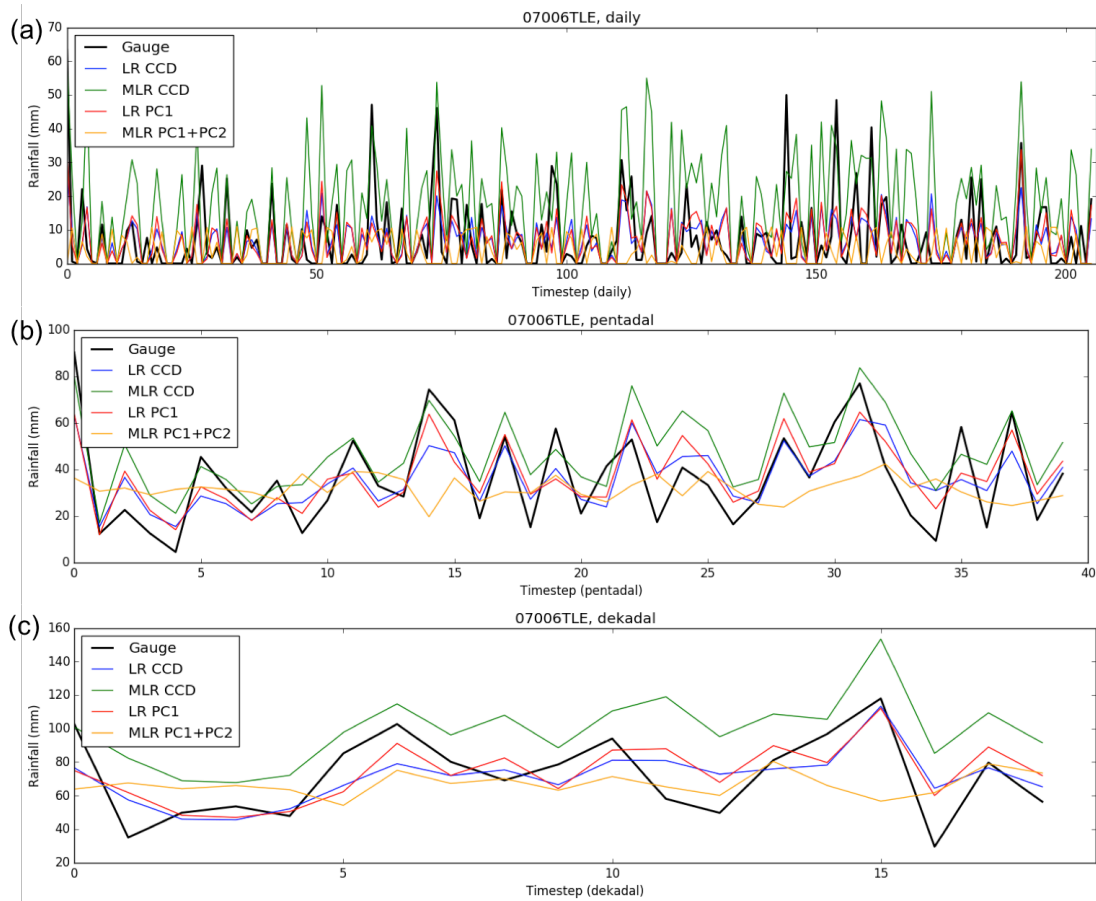


Figure A2.7. Timeseries of (a) daily, (b) pentadal and (c) dekadal rainfall from rain gauge and estimation methods at Tamale, Ghana during September 2005–2011.

The full regional performance of the calibration methods during September over Ghana can be gathered from the spatial maps of error statistics at all gauges for the three timescales (Fig. A2.8). In general, the error characteristics found in the methods at Tamale are also similar over the whole region. Both LR methods (LR CCD and LR PC1) have the lowest RMSE and smallest bias at all timescales and perform similarly at all stations. Overall, the bias in the LR methods is near-zero, however at some stations in the south a dry bias emerges at all calibration timescales, most likely due to increased rainfall occurrence from warm clouds (cloud top temperature $> -20^{\circ}\text{C}$) over this region. In contrast to the LR methods, MLR CCD overestimates whereas MLR PC1+PC2 underestimates rainfall almost everywhere. These substantial errors in the MLR methods suggest that both methods are unsuitable for accurate rainfall estimation.

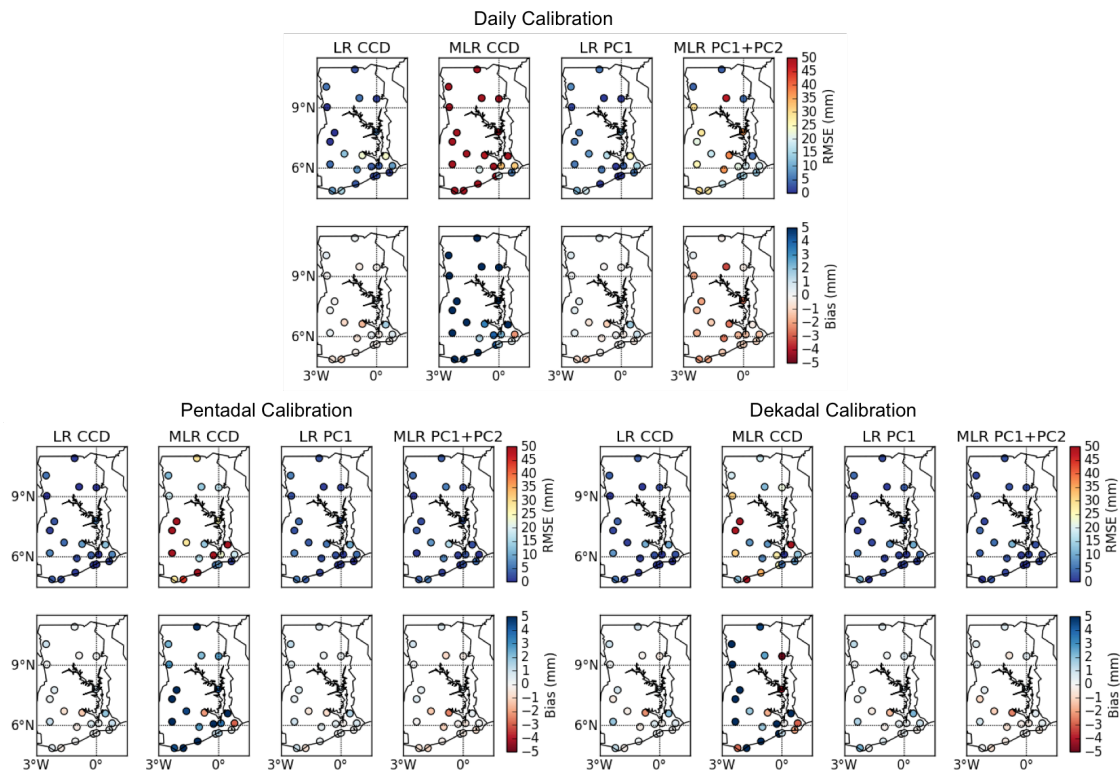


Figure A2.8 Spatial maps of RMSE and bias statistics at different timescales over Ghana, September, 2005–2011. For relative comparisons, units are all expressed in mm d^{-1} .

To further investigate how well each method captures the full seasonal cycle of rainfall over Ghana, monthly timeseries of mean rainfall and error statistics are displayed in Figs A2.9–A2.11. The statistics are grouped into two regions (north and south) to help assess the representation of the unimodal (single wet-season) annual cycle in the north and the bimodal (two wet-seasons) annual cycle in the south. Results from the MLR CCD method are not shown here because it performed very poorly relative to the other methods by highly overestimating rainfall amount. Overall, both LR methods are similar and capture the annual cycle in the north and south relatively well at each calibration timescale presented in Figs A2.9–A2.11. However, the LR methods sometimes overestimate rainfall during the wettest months (e.g. positive bias during April and August in both regions) and slightly underestimate rainfall during transitional months in the north (e.g. negative bias during March, June/July). In contrast, the MLR PC1+PC2 clearly underestimates rainfall at the daily scale with a negative bias however this reduces at the pentadal and dekadal scales.

As was also apparent for the September calibration, both LR methods produce very similar results. Consequently, it is clear that even though the LR PC1 method contains information from multiple TIR thresholds, the method shows no substantial improvement on the LR CCD method. This result further highlights the strength of the current standard TAMSAT calibration and from these conclusions we therefore choose to continue using the standard TAMSAT calibration method.

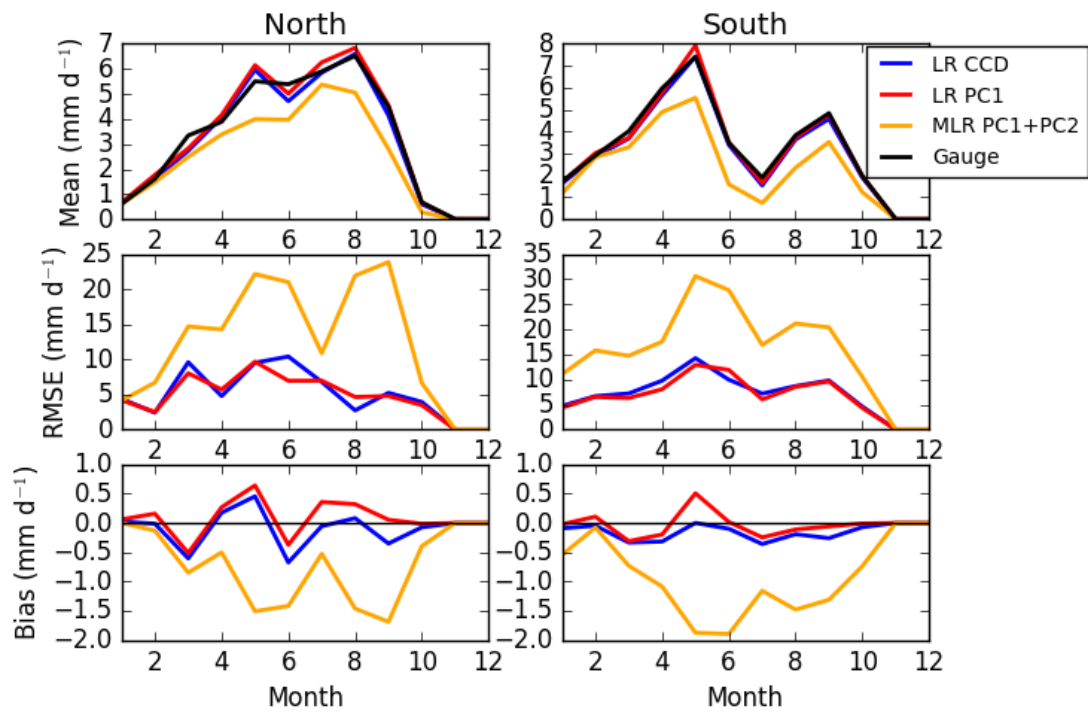


Figure A2.9. Monthly timeseries of daily mean rainfall, RMSE and Bias for the daily calibration of each method averaged over northern stations (north of 7°N) and southern stations (south of 7°N).

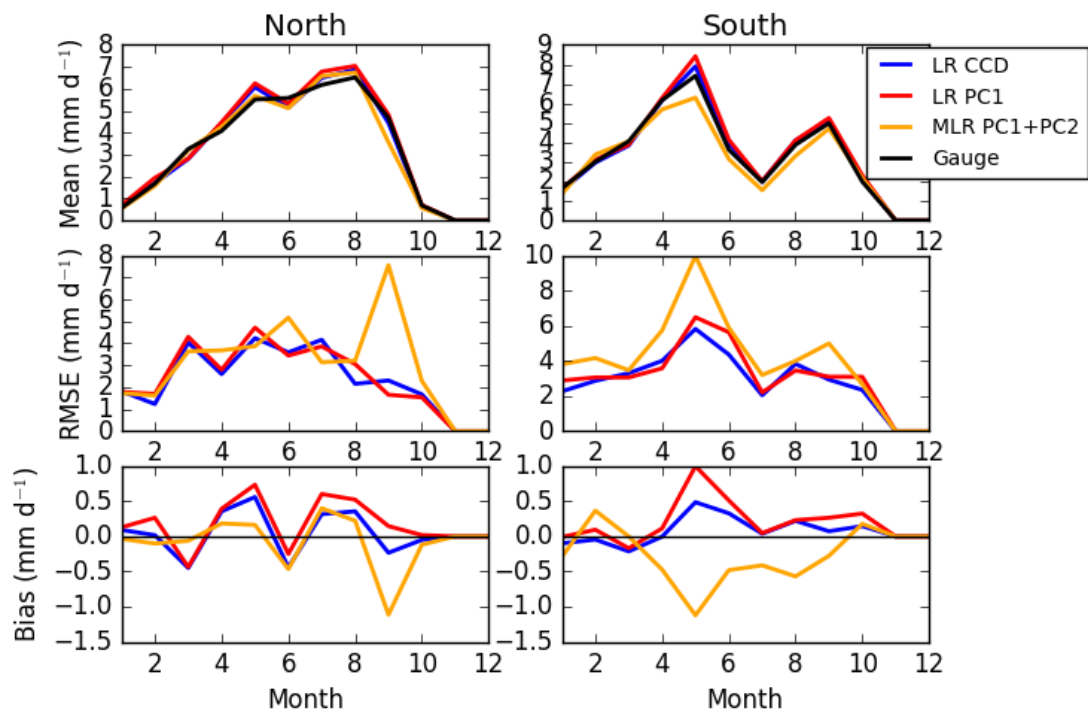


Figure A2.10. Monthly timeseries of daily mean rainfall, RMSE and Bias for the pentadal calibration of each method averaged over northern stations (north of 7°N) and southern stations (south of 7°N).

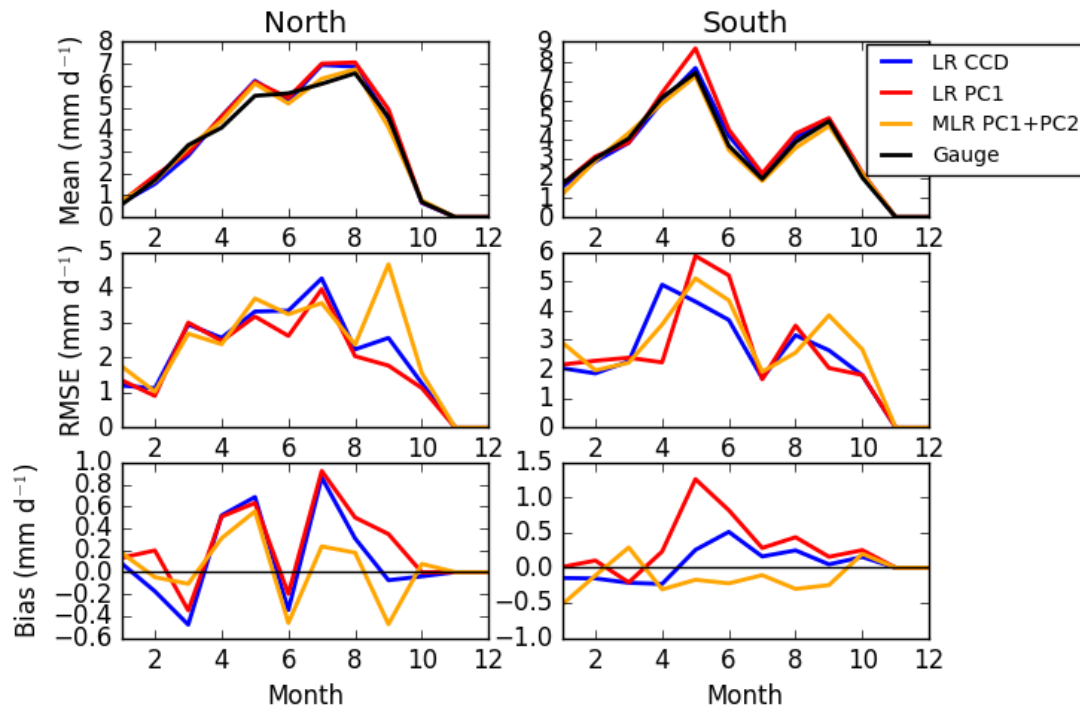


Figure A2.11. Monthly timeseries of daily mean rainfall, RMSE and Bias for the dekadal calibration of each method averaged over northern stations (north of 7°N) and southern stations (south of 7°N).

Calibration timescale

The previous sensitivity study assessing different calibration methods illustrates that the standard TAMSAT method is optimal for rainfall estimation at all timescales. Now that the most appropriate calibration method is identified, we investigate which timescale is optimal for calibrating the algorithm and deriving rainfall estimates. In the previous analysis, the performance of the daily, pentadal and dekadal LR CCD calibrations all showed similar results, however it is important to highlight some factors that effect the calibration at these different timescales which should be taken into account. A calibration conducted at the shortest (daily) timescale, has the benefit of having many gauge-CCD pairs (> 10) in each CCD bin allowing for a statistically robust calibration. However, calibrating at daily scale may be less skilful than calibrating at longer scales because the amount of CCD is associated with cumulated rainfall rather than the intensity of individual events. Calibrating at the longest (dekadal) timescales has, moreover, been shown to cumulate rainfall sufficiently by Milford et al, (1994). Nevertheless, dekadal rainfall may result from several distinct systems, each of which has the potential to add information to the calibration. There is value, therefore, in exploring whether the additional information provided by daily or pentadal estimates outweighs the shorter rainfall accumulation time.

Figure A2.12 depicts linear regressions using the standard method for the three timescales during September at Tamale. All timescales show strong linear correlations with gauge rainfall highlighting that calibrating the TAMSAT method at sub-dekadal timescales is feasible for this time period and location. Moreover, these linear relationships between the

gauge–CCD pairs further illustrate the trade-offs between using different timescales for the calibration. At daily timescales, there is large range of rainfall associated with a given CCD, suggesting that the relationship between CCD and rainfall is highly variable. In contrast, despite the larger number of events included, the range of rainfall for a given CCD at pentadal time scales is only slightly greater than at dekadal time scales. The use of more independent samples furthermore leads to a less noisy calibration. On this basis and on the basis of similar studies for Ethiopia and Zambia (not shown), we therefore choose to use a pentadal calibration.

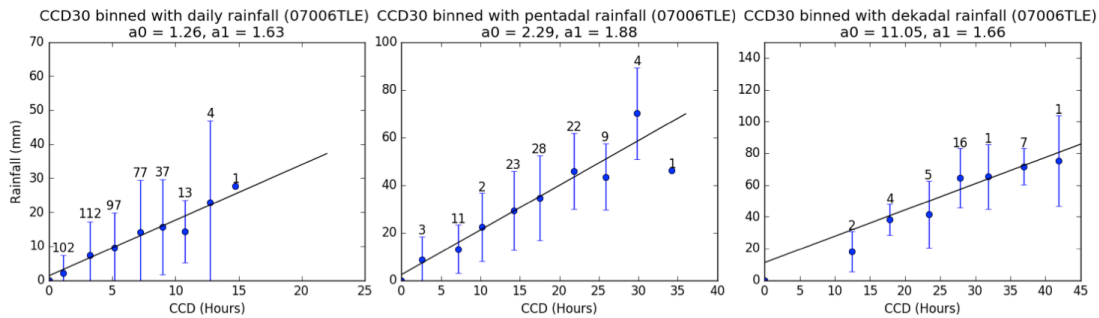


Figure A2.12. Relationships between rainfall and CCD (hours) during September 1989–2004 at Tamale, Ghana for daily, pentadal and dekadal time periods. The mean rainfall, standard deviation and number of samples within each CCD bin are represented by the circles, whiskers and numbers respectively.

Pentadal calibration: aggregation and disaggregation results

To assess the performance of the daily/dekadal rainfall estimates disaggregated/aggregated from pentadal estimates derived using a pentadal calibration, we compare them to the Ghana rain gauge observations and current operational TAMSAT rainfall estimates. The disaggregation from pentad to daily rainfall is conducted using the daily and pentadal CCD (as described above), whereas the aggregation from pentadal to dekadal rainfall is conducted by simply accumulating the two pentads within a given dekad. As in Fig’s A2.1–A2.11, seasonal statistics of the pentadal calibration disaggregated to the daily timescale and aggregated to the dekadal timescale are depicted in Fig.’s A2.13 and A2.14. As indicated by their lower RMSE and bias, it is clear from these figures that the disaggregated and aggregated estimates at both timescales from the pentadal calibration improve relative to the current TAMSAT estimates derived from a dekadal calibration. For the daily disaggregated estimates, the RMSE has reduced by a factor of 2 during April and September in both regions. As expected, current TAMSAT estimates at the daily and dekadal periods are characterised by a dry bias that reaches between -0.5 and -1.3 mm d^{-1} . In contrast, the bias of the pentadal calibration is smaller – a negative bias of up to -0.5 mm d^{-1} during ‘transitional’ months (e.g. March, June and September in the northern region) and conversely a positive bias of up to 0.5 mm d^{-1} during wet months.

Although the pentadal calibration clearly improves on the current TAMSAT method at both timescales, it is important to note that it has been locally calibrated against the 22 individual stations, whereas the TAMSAT estimates have been calibrated using larger calibration zones. Because regional rainfall characteristics can be very localised, the regional calibration of the current TAMSAT estimates will be an additional factor that leads to its poorer performance at these 22 stations.

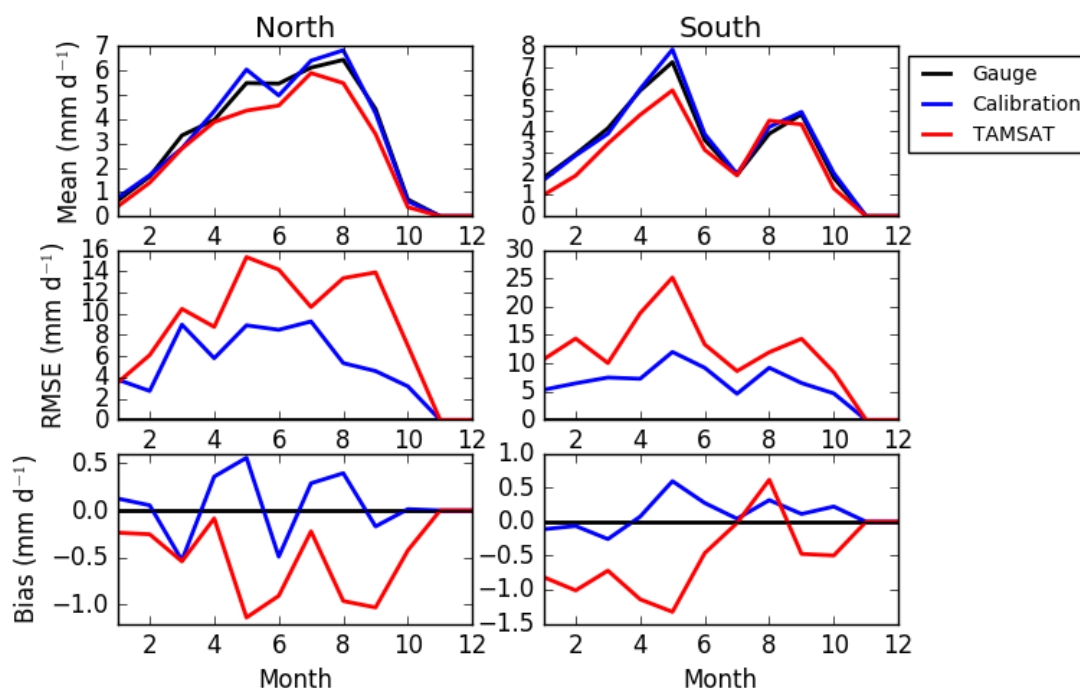


Figure A2.13. Monthly timeseries of the performance of daily rainfall estimates disaggregated from the pentadal calibration ('calibration') and disaggregated from the current TAMSAT dekadal calibration ('TAMSAT').

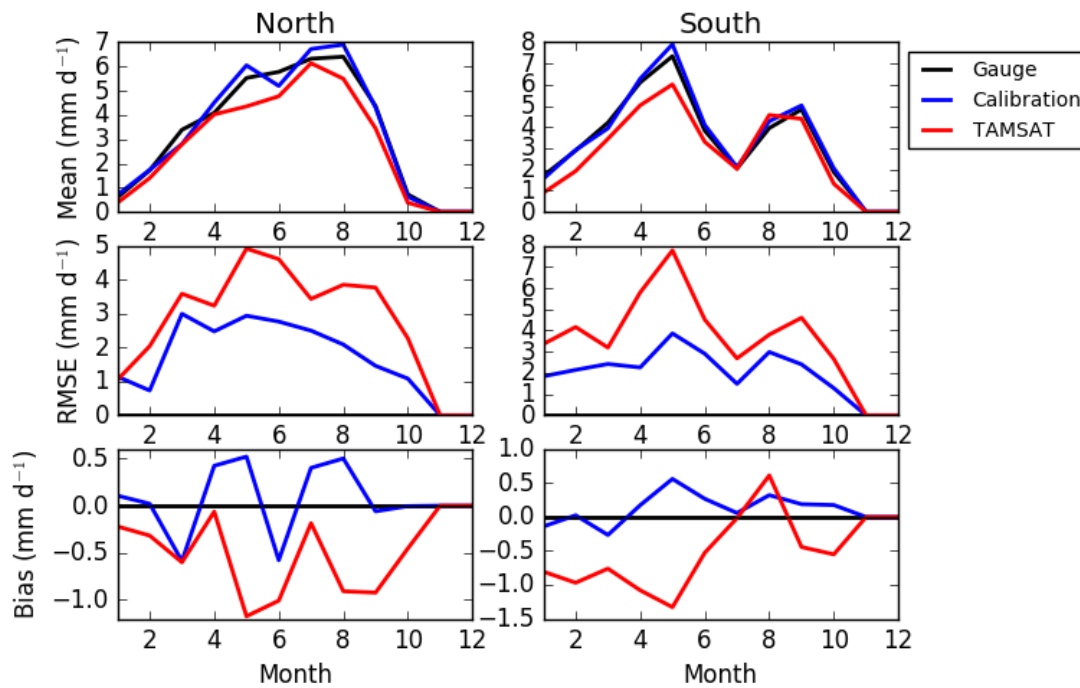


Figure A2.14. Monthly timeseries of the performance of dekadal rainfall estimates aggregated from the pentadal calibration ('calibration') and the current TAMSAT dekadal rainfall estimates ('TAMSAT').

d. Summary and conclusions

This appendix has reported the results of a series of sensitivity tests to assess the optimal calibration method and timescale to utilise to improve TAMSAT rainfall estimates. In order to understand whether the use of multiple TIR thresholds could improve rainfall estimation, four different calibration methods were assessed – the standard TAMSAT method (Linear regression on CCD at the dominant threshold), a linear regression on the first principal component of CCD, a multiple linear regression on CCD at all thresholds and a multiple linear regression on the first and second principal components of CCD all thresholds. Each of these methods were independently calibrated and evaluated using measurements from 22 gauge–CCD pairs over Ghana over the period 1984–2011.

Overall, the analysis showed that a linear regression on CCD at the dominant threshold and a linear regression on the first principal component of CCD had the best accuracy (lowest RMSE and bias) for rainfall estimation relative to multiple linear regression techniques. Somewhat surprisingly, the simple standard linear regression method performed as well as the more sophisticated principal component method. Although the first principle component effectively reduces the information represented by multiple CCD thresholds into one-dimension, there is marked co-variability in CCD at all thresholds. This strong co-variability explains why the standard method performed so similarly and further highlights that the use of a single threshold is suitable for estimating rainfall amount without the need for a more complex approach.

The influence of different timescales (daily, pentadal and dekadal) on the calibration was also examined. It was found that the pentadal calibration of the LR CCD method performed better than the dekadal calibration over Ghana. A comparison of daily, pentadal and dekadal calibrations illustrated that calibrating at the pentadal scale optimised the number of gauge-CCD pairs available for calibration while at the same time capturing relatively high rainfall totals. Daily and dekadal rainfall estimates disaggregated and aggregated from the pentadal calibration showed a reduced error and bias relative to current TAMSAT rainfall estimates. In summary, these results suggest that the application of a pentadal calibration to the current TAMSAT method (LR CCD) will result in improved rainfall estimates.

References

Arkin, P. A. and B. N. Meisner, 1987: The Relationship between Large-Scale Convective Rainfall and Cold Cloud over the Western Hemisphere during 1982-84. *Mon. Wea. Rev.*, **115**, 51–74.

Dinku, T., P. Ceccato, E. GroverKopec, M. Lemma, S. J. Connor and C. F. Ropelewski, 2007: Validation of satellite rainfall products over East Africa's complex topography. *Int. J. Remote Sens.*, **28**, 1503–1526.

Grimes, D., E. Pardo-Iguzquiza and R. Bonifacio, 1999: Optimal areal rainfall estimation using raingauges and satellite data. *J. Hydro.*, **222**, 93–108.

Jobard, I., F. Chopin, J. C. Berges and R. Roca, 2011: An intercomparison of 10-day satellite precipitation products during West African monsoon. *Int. J. Remote Sens.*, **32**, 2353–2376.

Lorenz, C. and H. Kunstmann, 2012: The Hydrological Cycle in Three State-of-the-art Reanalyses: Intercomparison and Performance Analysis. *J. Hydrometeor.*, **13**, 1397–1420.

Maidment, R. I., R. P. Allan, and E. Black 2015: Recent observed and simulated changes in precipitation over Africa. *Geophys. Res. Lett.*, **42**, 8155–8164, doi:10.1002/2015GL065765.

Maidment, R. I., D. I. Grimes, R. P. Allan, H. Greatrex, O. Rojas and O. Leo, 2013: Evaluation of satellite-based and model re-analysis rainfall estimates for Uganda. *Meteorol. App.*, **20**, 308–317.

Maidment, R. I., D. Grimes, D., R. P. Allan, E. Tarnavsky, M. Stringer, T. Hewison, R. Roebeling and E. Black, 2014: The 30-year TAMSAT African rainfall climatology and time-series (TARCAT) dataset. *J. Geophys. Res. Atmos.*, **119**, 10,619–10,644.

Maidment, R. I., D. I. F. Grimes, and E. Tarnavsky, 2012: Rainfall data generation and analysis for African meteorology. *Climate Change, Agriculture and Food Security Tech. Rep.*, 26 pp.

Appendix 3: TAMSAT v2.0 calibration summary

This section provides a brief description of the calibration process used to create TAMSAT v2.0 (otherwise known as the TAMSAT African Rainfall Climatology and Time-series (TARCAT) dataset). The estimation of rainfall can be considered as a two-part process. The initial step delineates rainy regions from non-rainy regions while a rain rate or amount is then assigned to the rainy regions. The estimation of rainfall can therefore be expressed as a product of rainfall occurrence and rainfall intensity computed over each satellite pixel at a given time-step.

The calibration is split into two parts: derivation of the optimum temperature threshold (T_t) which determines if a pixel is rainy or not and derivation of the linear regression coefficients (a_0 and a_1) which determines the rainfall amount for rainy pixels. This approach applies to both version 2 and version 3 of the calibration.

The calibration steps below are performed Africa-wide and repeated for each calendar month.

Data requirements

1. Africa-wide dekadal gauge records from various sources (e.g. various African Met Services, JRC) collated over the years into a single database.
2. Dekadal cold cloud duration (CCD) files at a discrete temperature thresholds (-30°C , -40°C , -50°C , -60°C) are created using available Meteosat satellite imagery between 1983 and 2014.
3. For each dekadal gauge record, the corresponding dekadal CCD pixel value at each CCD temperature threshold is extracted – these are known as gauge-CCD pairs. For TAMSATv2.0, gauge records and CCD between 1983–2010 were used.

Derivation of the optimum temperature threshold

1. Derivation of T_t is carried out at the dekadal scale.
2. Dekadal gauge-CCD pairs are pooled together from climatologically similar regions. The boundaries for these climatological zones, illustrated in Figure #, were created and subsequently refined from numerous calibration attempts since the 1980s. The zone size and boundaries are chosen to account for local rainfall characteristics while containing enough rain gauges for the calibration (Tarnavsky et al., 2014).
3. The T_t is determined based for each zone on a metric comparable to the frequency bias using the gauge-CCD pairs. A threshold of 0 mm is used to determine if a dekadal is dry or not.
4. Africa-wide maps of T_t are then created for each zone. To prevent sharp discontinuities between zones, artificial smoothing is applied over a 1° distance.

Derivation of the calibration parameters

1. Derivation of the calibration parameters are based on the dekadal gauge-CCD pairs.

2. For each zone, the available dekadal gauge-CCD pairs are binned by CCD value at regular intervals. Only the CCD values derived from the optimum cloud top temperature for that zone are used. Linear calibration coefficients (a_0 and a_1) are then estimated by regressing the median gauge rainfall against the mean CCD value for each bin.
3. Africa-wide maps of the a_0 and a_1 are then created for each zone. To prevent sharp discontinuities between zones, artificial smoothing is applied over a 1° distance.

Appendix 4: TAMSAT v3.0 pentadal calibration parameters

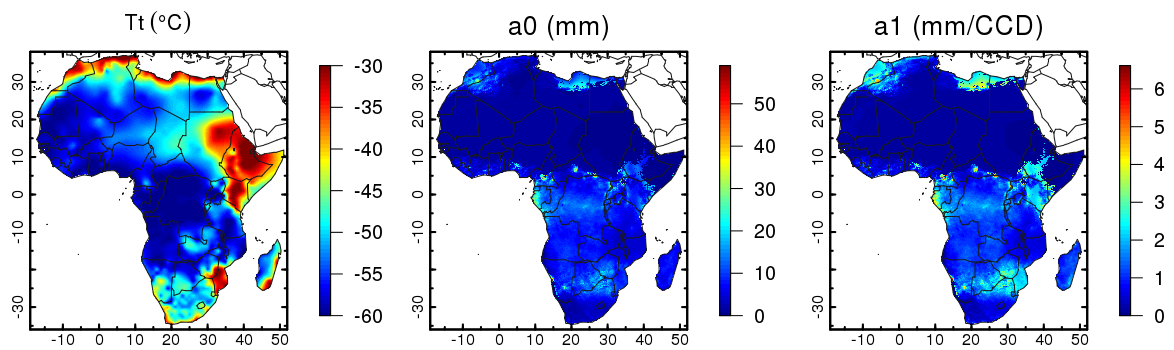


Figure A4.1. TAMSAT v3.0 calibration parameters for January, 1st pentad.

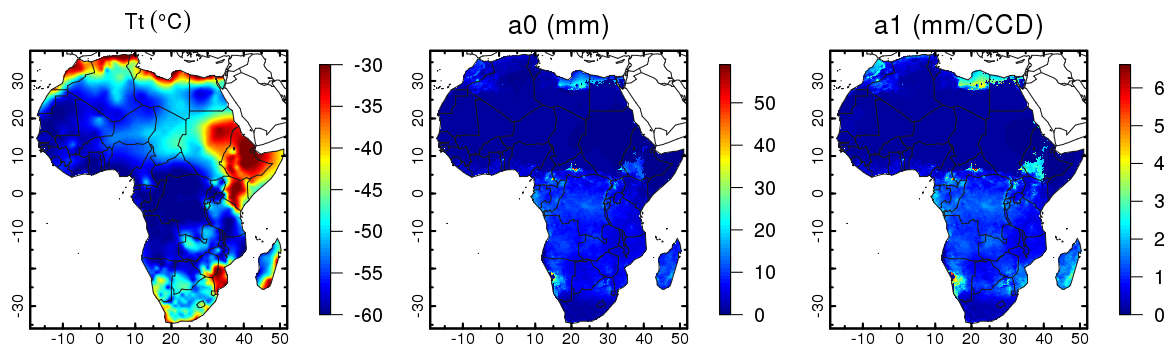


Figure A4.2. TAMSAT v3.0 calibration parameters for January, 2nd pentad.

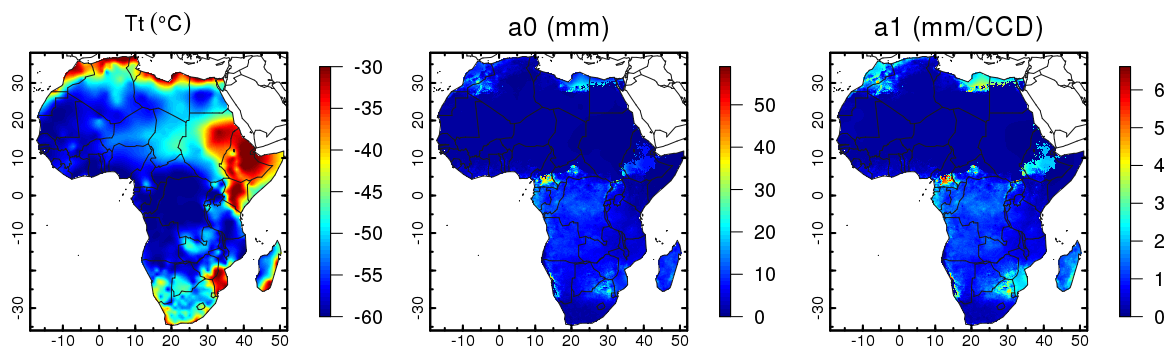


Figure A4.3. TAMSAT v3.0 calibration parameters for January, 3rd pentad.

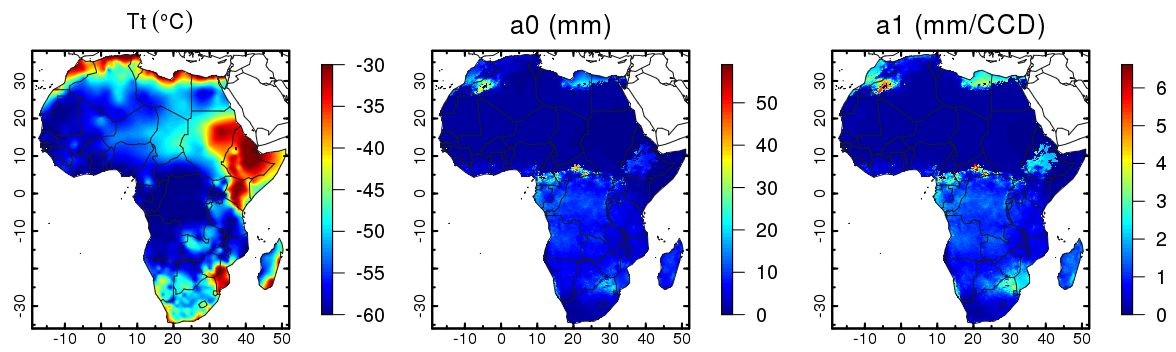


Figure A4.4. TAMSAT v3.0 calibration parameters for January, 4th pentad.

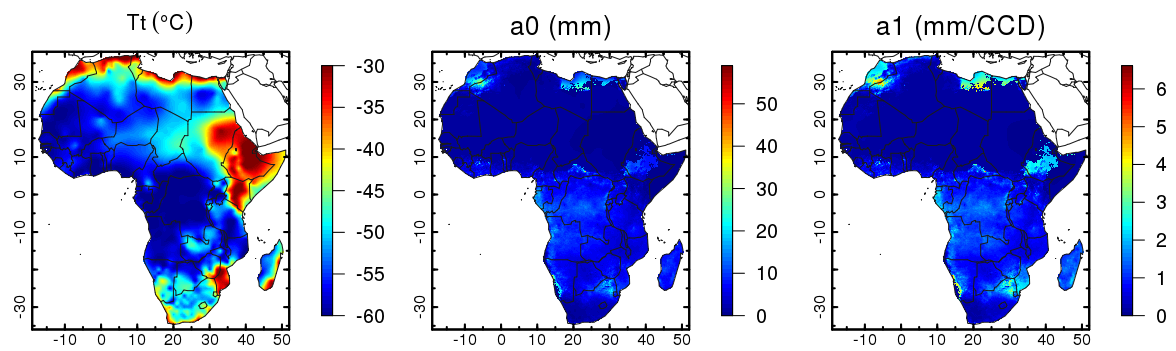


Figure A4.5. TAMSAT v3.0 calibration parameters for January, 5th pentad.

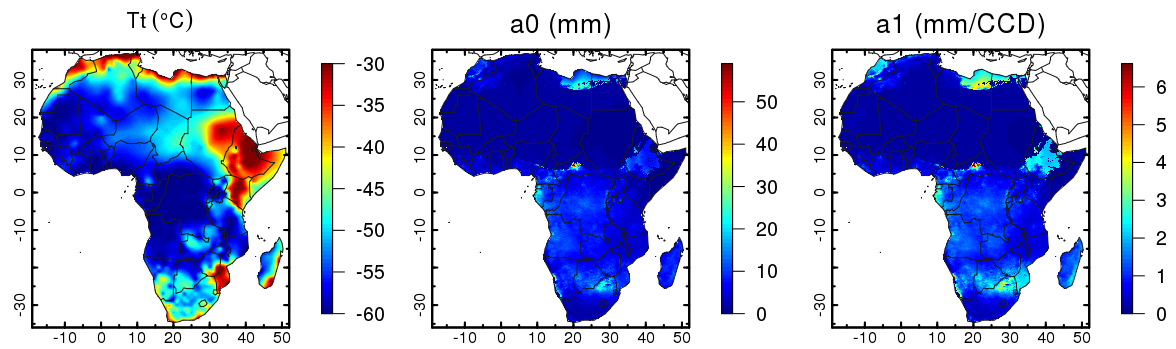


Figure A4.6. TAMSAT v3.0 calibration parameters for January, 6th pentad.

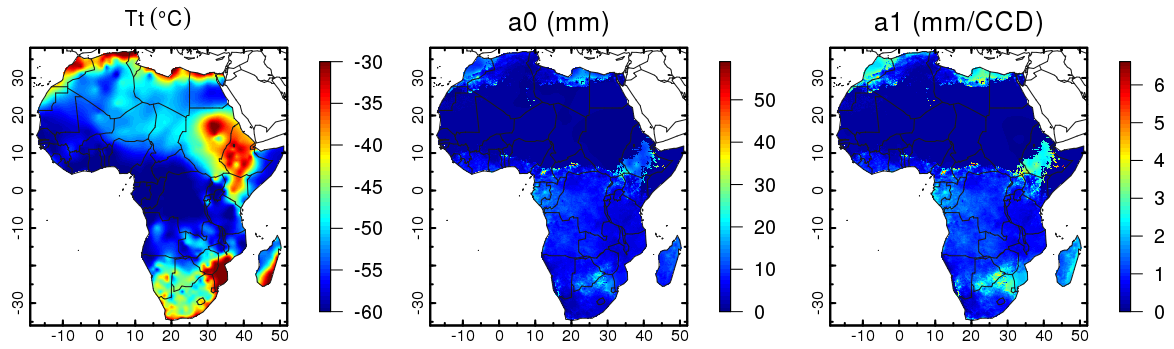


Figure A4.7. TAMSAT v3.0 calibration parameters for February, 1st pentad.

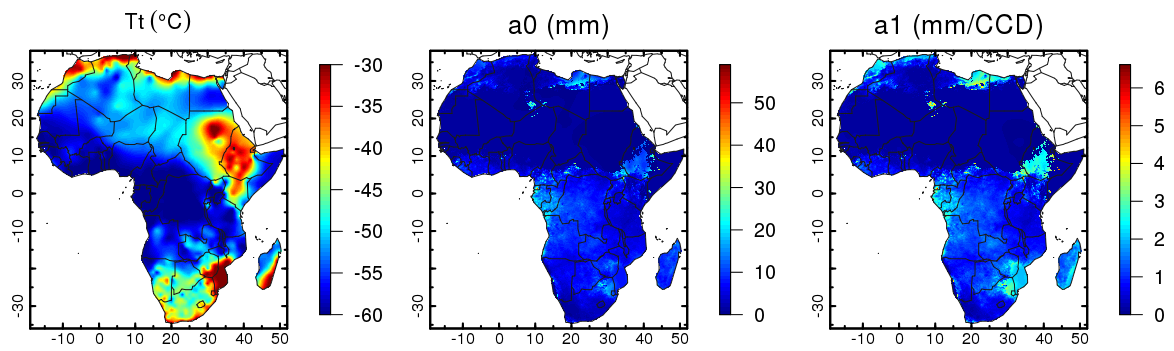


Figure A4.8. TAMSAT v3.0 calibration parameters for February, 2nd pentad.

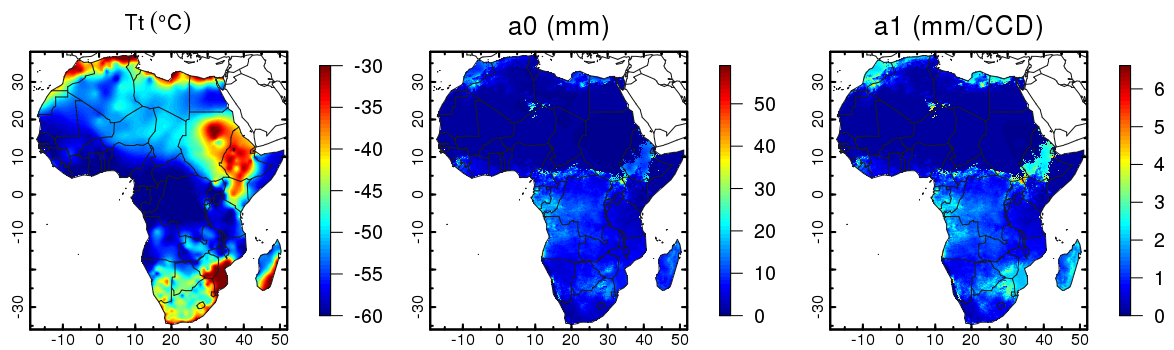


Figure A4.9. TAMSAT v3.0 calibration parameters for February, 3rd pentad.

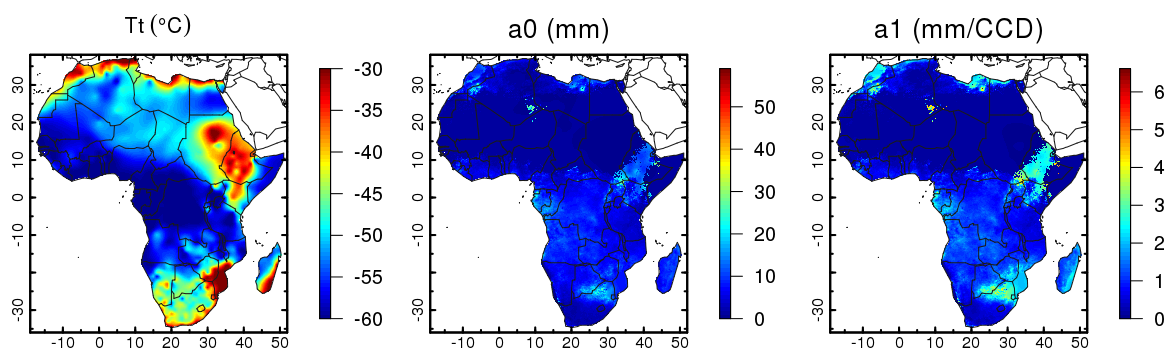


Figure A4.10. TAMSAT v3.0 calibration parameters for February, 4th pentad.

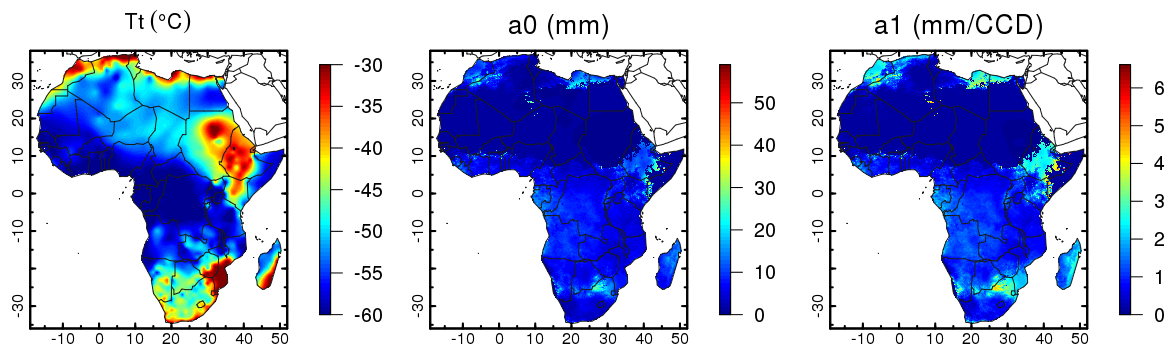


Figure A4.11. TAMSAT v3.0 calibration parameters for February, 5th pentad.

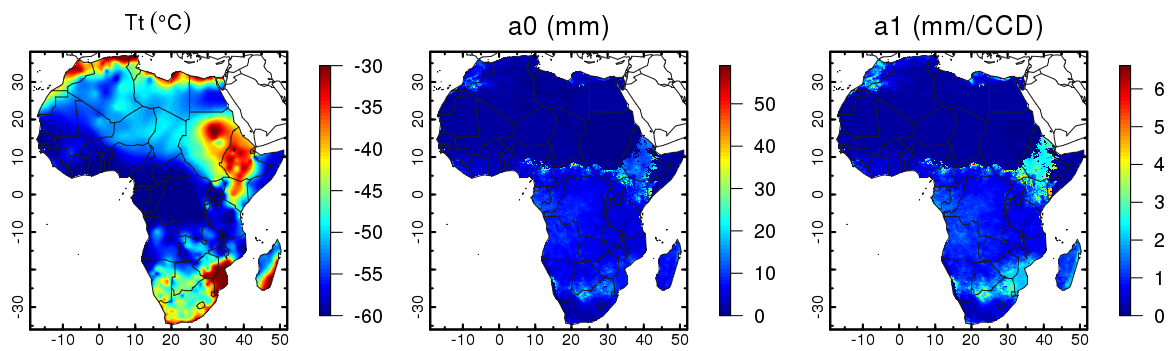


Figure A4.12. TAMSAT v3.0 calibration parameters for February, 6th pentad.

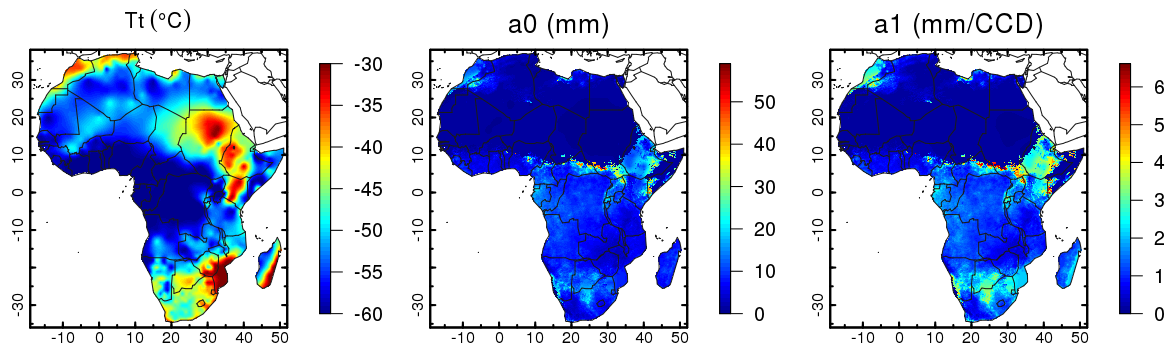


Figure A4.13. TAMSAT v3.0 calibration parameters for March, 1st pentad.

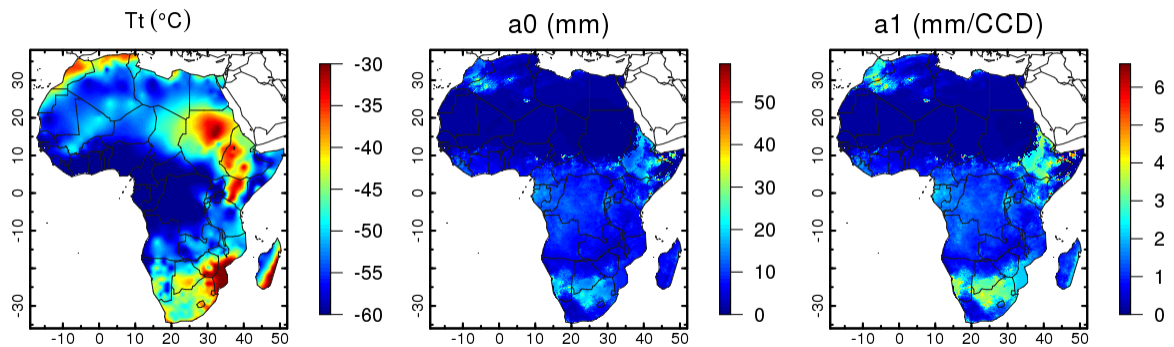


Figure A4.14. TAMSAT v3.0 calibration parameters for March, 2nd pentad.

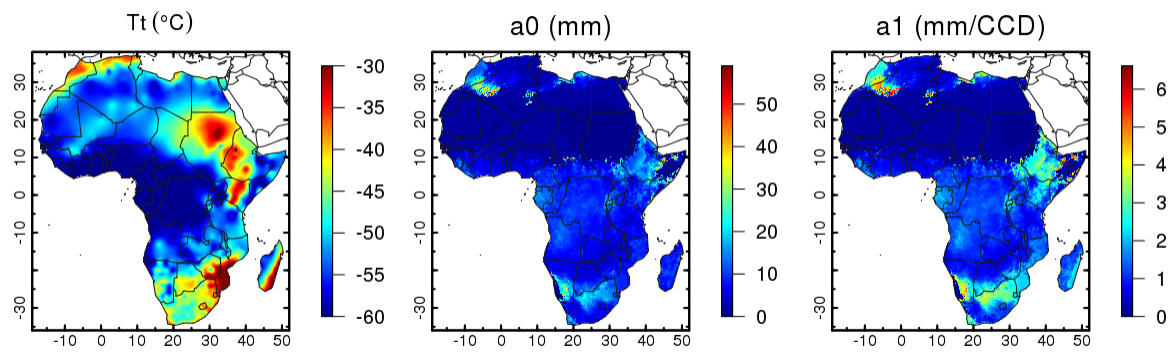


Figure A4.15. TAMSAT v3.0 calibration parameters for March, 3rd pentad.

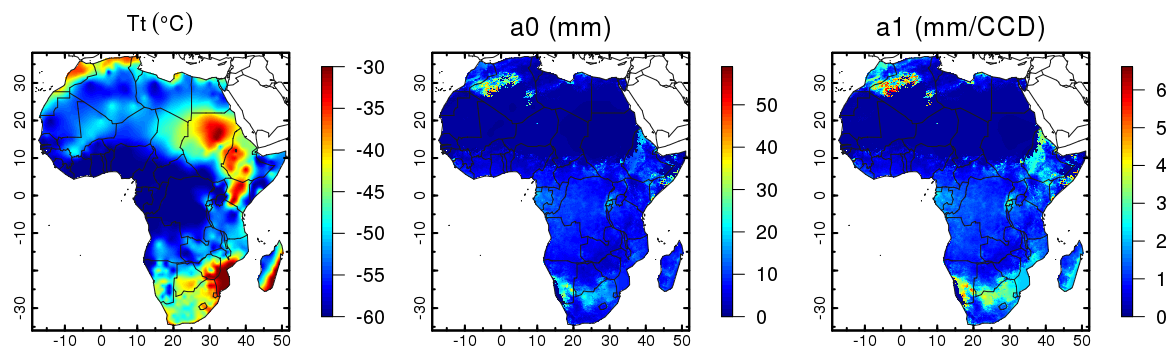


Figure A4.16. TAMSAT v3.0 calibration parameters for March, 4th pentad.

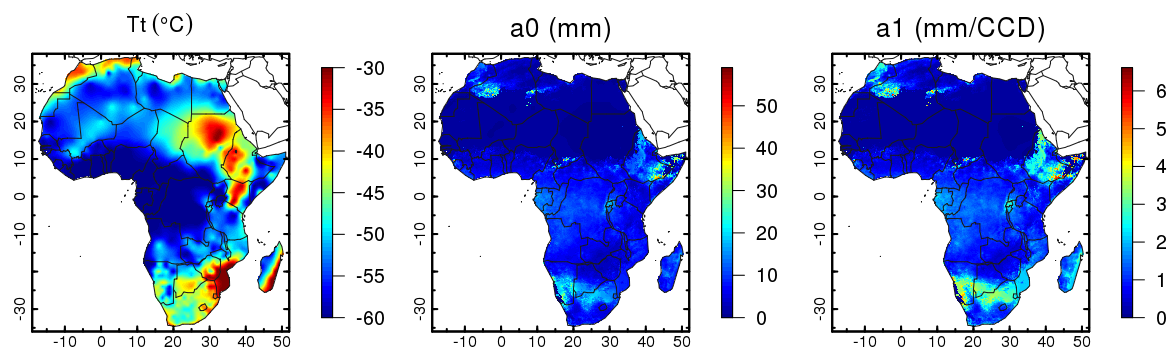


Figure A4.17. TAMSAT v3.0 calibration parameters for March, 5th pentad.

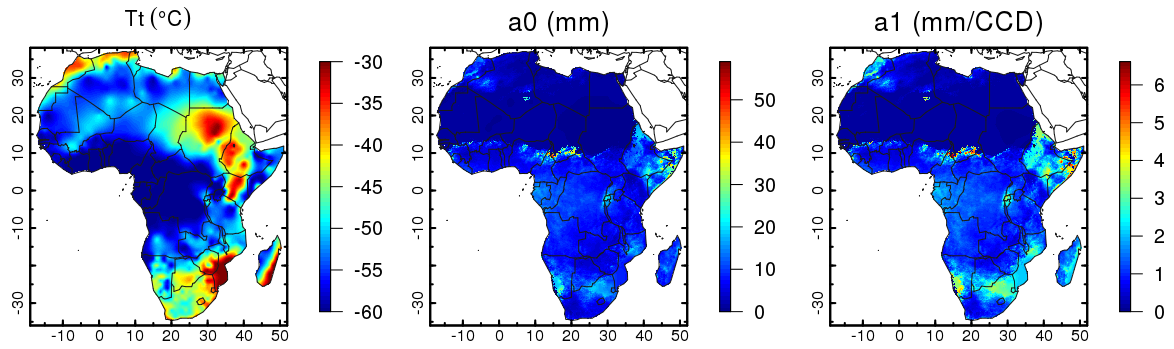


Figure A4.18. TAMSAT v3.0 calibration parameters for March, 6th pentad.

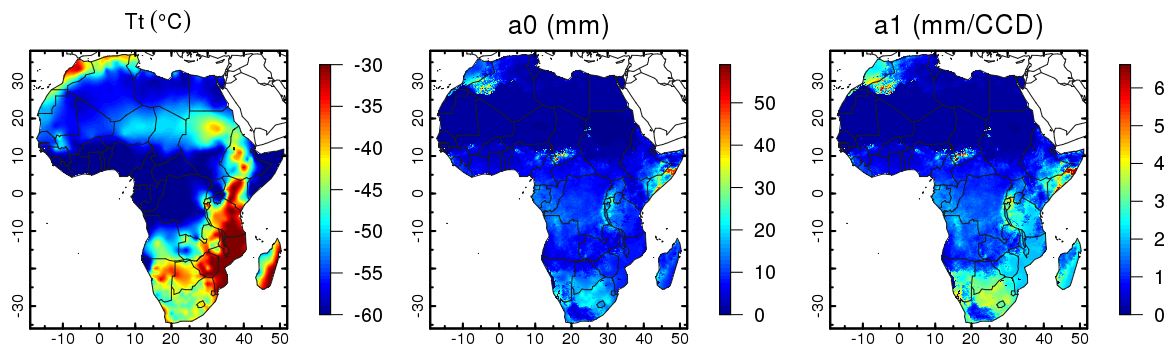


Figure A4.19. TAMSAT v3.0 calibration parameters for April, 1st pentad.

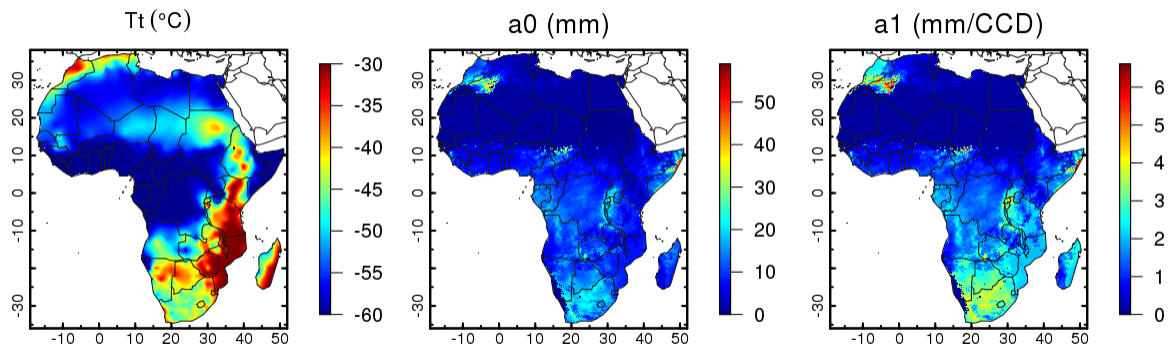


Figure A4.20. TAMSAT v3.0 calibration parameters for April, 2nd pentad.

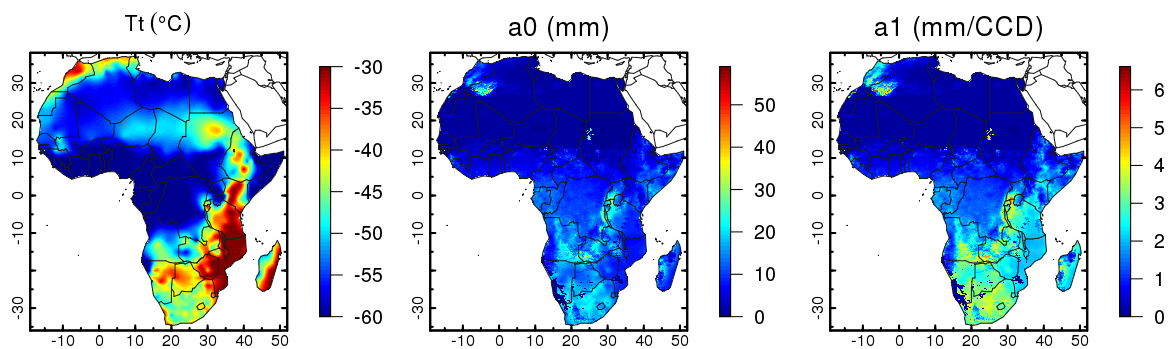


Figure A4.21. TAMSAT v3.0 calibration parameters for April, 3rd pentad.

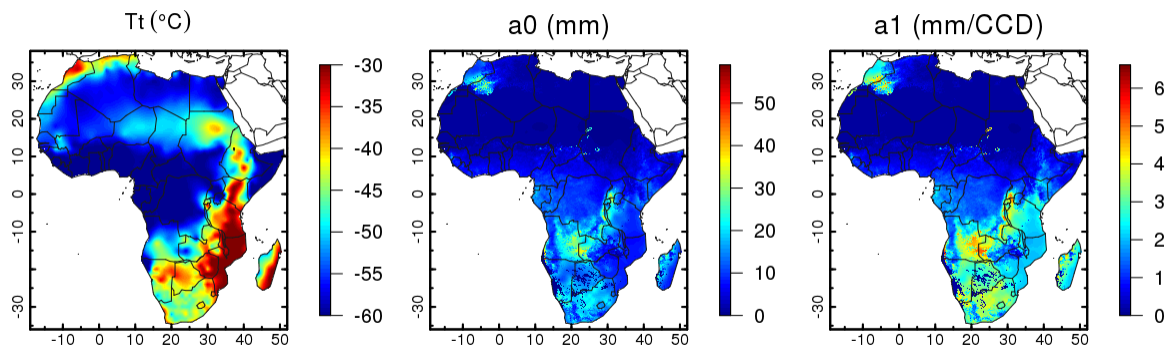


Figure A4.22. TAMSAT v3.0 calibration parameters for April, 4th pentad.

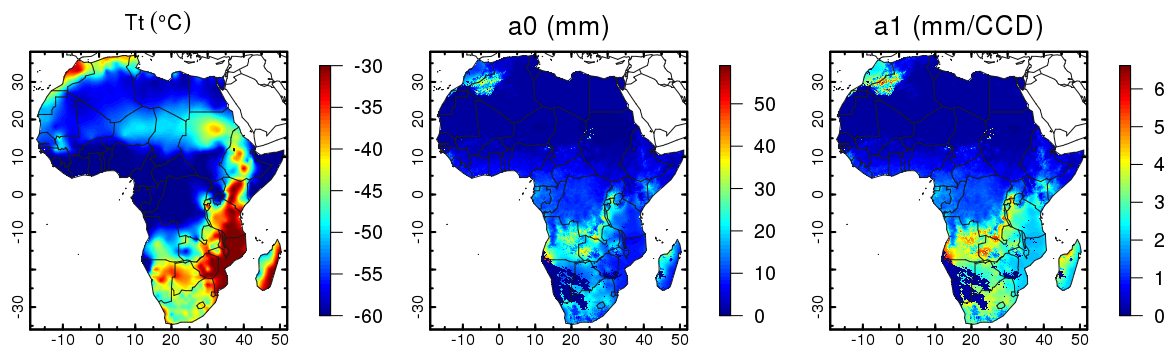


Figure A4.23. TAMSAT v3.0 calibration parameters for April, 5th pentad.

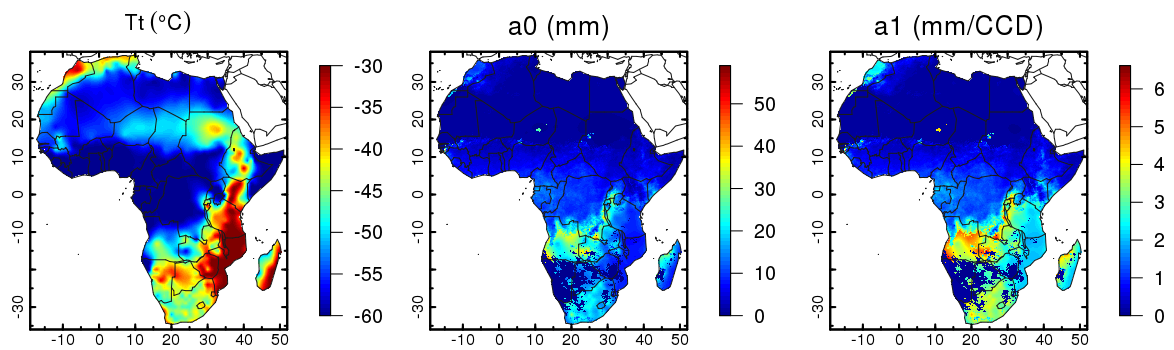


Figure A4.24. TAMSAT v3.0 calibration parameters for April, 6th pentad.

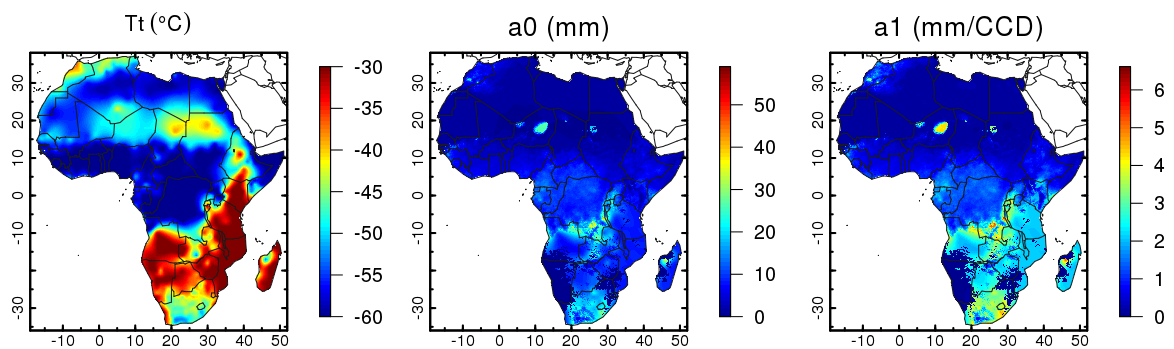


Figure A4.25. TAMSAT v3.0 calibration parameters for May, 1st pentad.

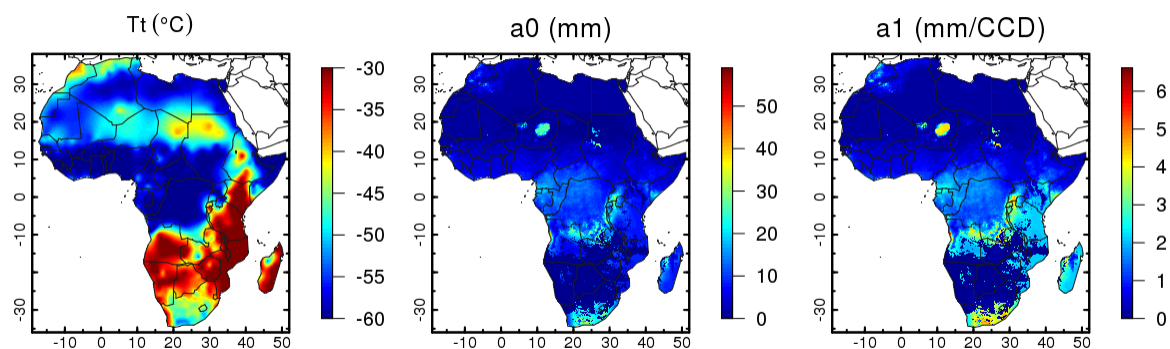


Figure A4.26. TAMSAT v3.0 calibration parameters for May, 2nd pentad.

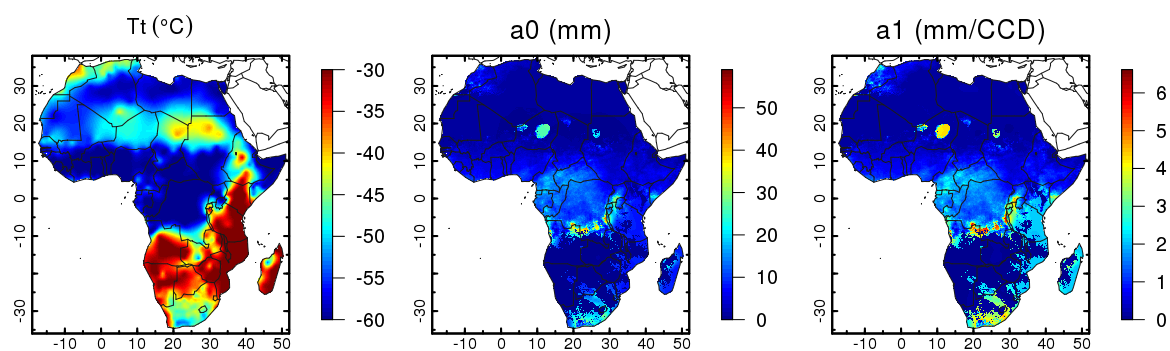


Figure A4.27. TAMSAT v3.0 calibration parameters for May, 3rd pentad.

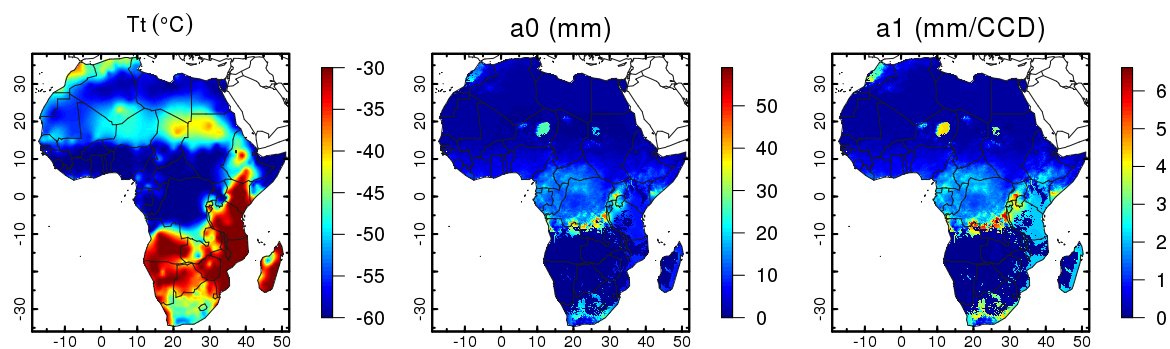


Figure A4.28. TAMSAT v3.0 calibration parameters for May, 4th pentad.

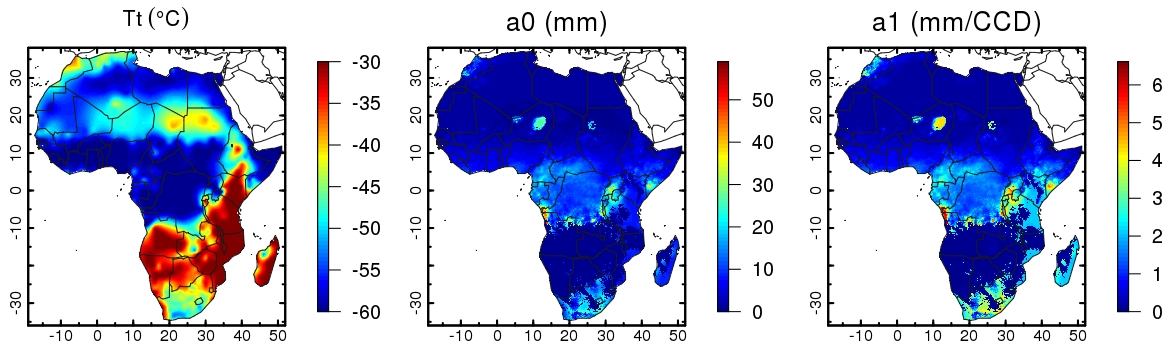


Figure A4.29. TAMSAT v3.0 calibration parameters for May, 5th pentad.

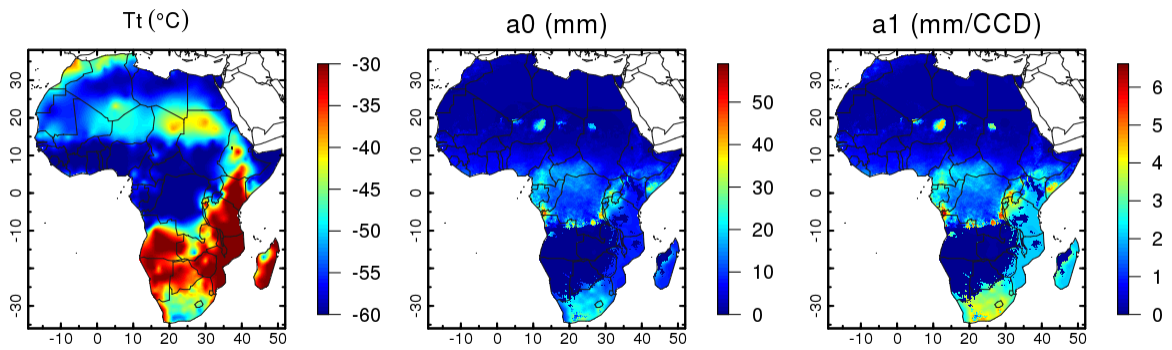


Figure A4.30. TAMSAT v3.0 calibration parameters for May, 6th pentad.

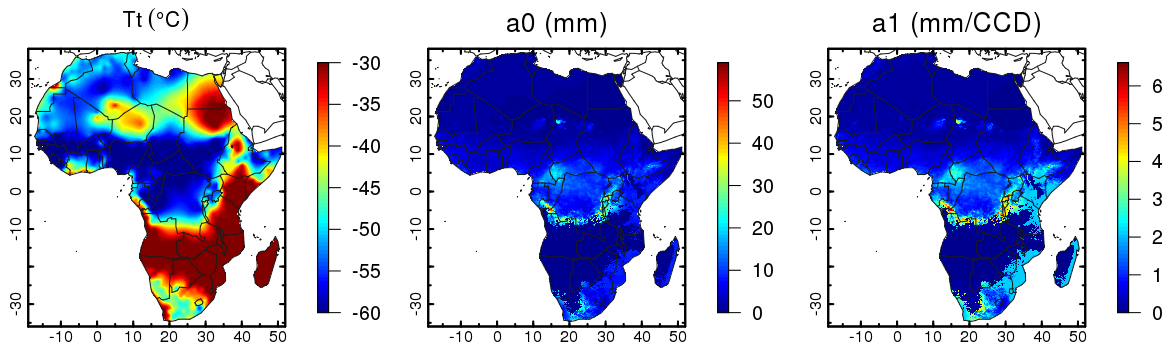


Figure A4.31. TAMSAT v3.0 calibration parameters for June, 1st pentad.

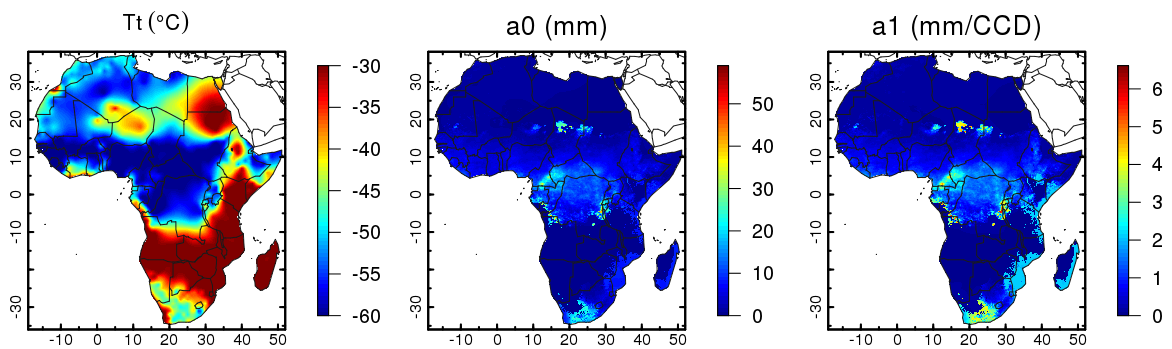


Figure A4.32. TAMSAT v3.0 calibration parameters for June, 2nd pentad.

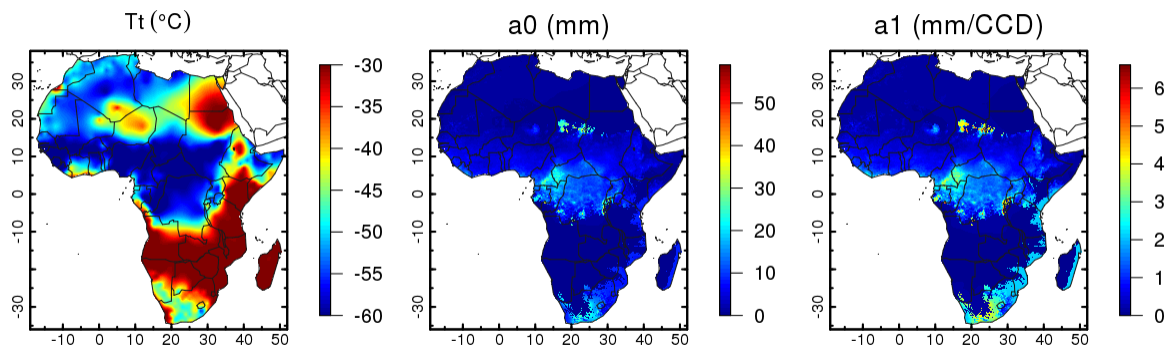


Figure A4.33. TAMSAT v3.0 calibration parameters for June, 3rd pentad.

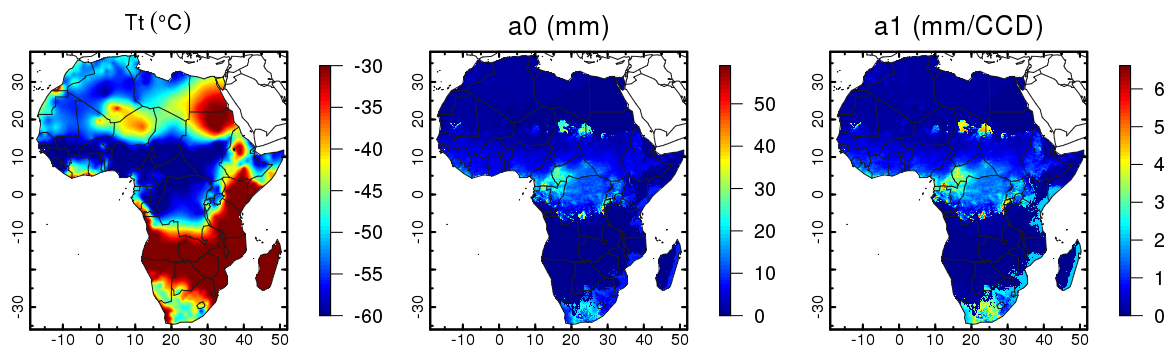


Figure A4.34. TAMSAT v3.0 calibration parameters for June, 4th pentad.

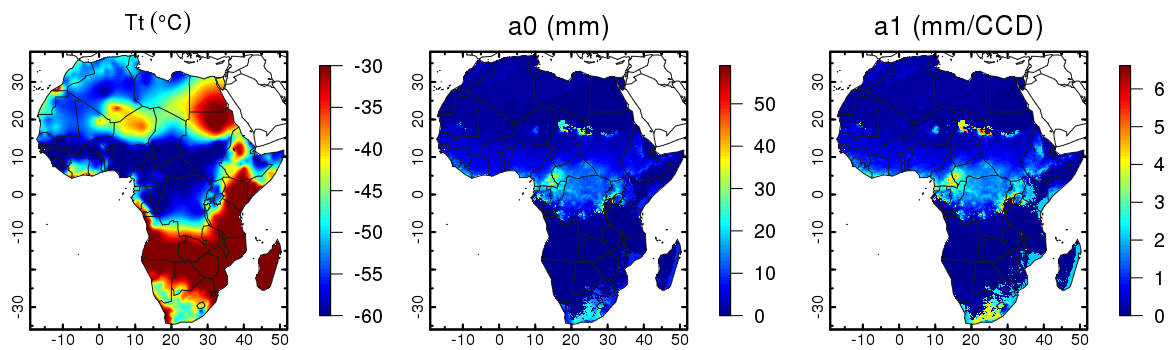


Figure A4.35. TAMSAT v3.0 calibration parameters for June, 5th pentad.

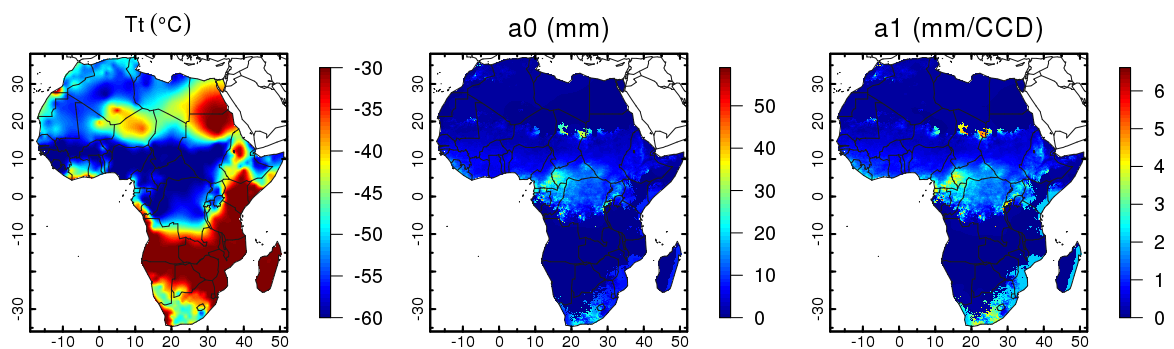


Figure A4.36. TAMSAT v3.0 calibration parameters for June, 6th pentad.

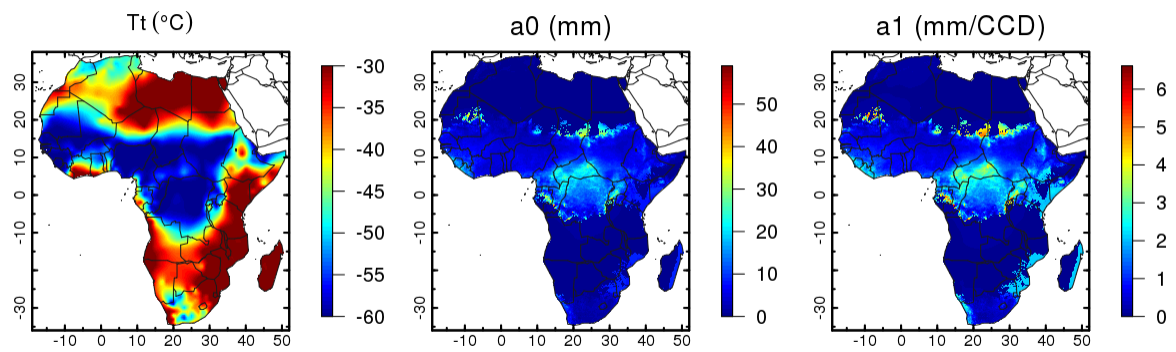


Figure A4.37. TAMSAT v3.0 calibration parameters for July, 1st pentad.

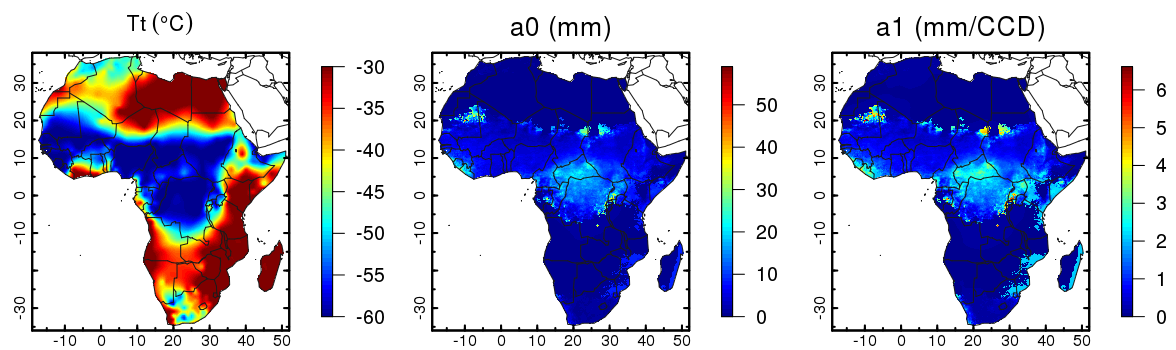


Figure A4.38. TAMSAT v3.0 calibration parameters for July, 2nd pentad.

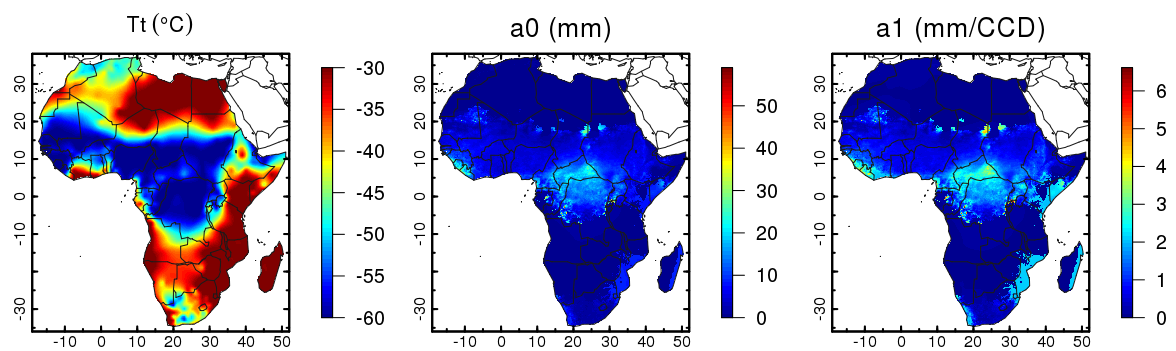


Figure A4.39. TAMSAT v3.0 calibration parameters for July, 3rd pentad.

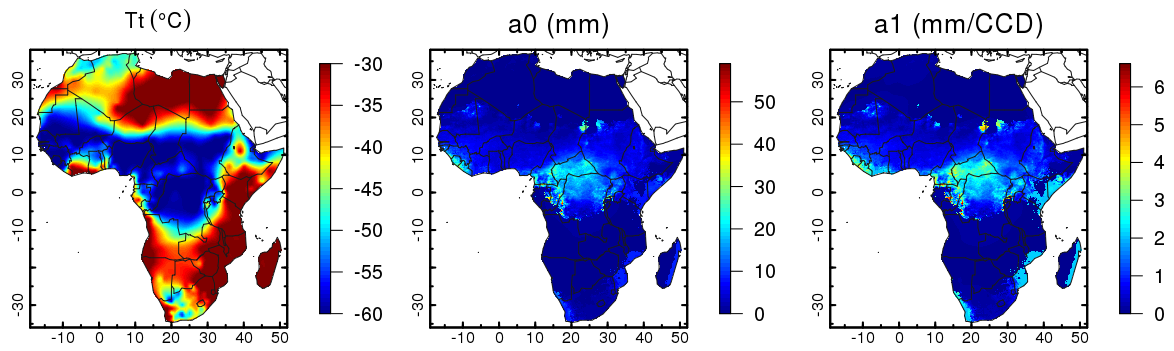


Figure A4.40. TAMSAT v3.0 calibration parameters for July, 4th pentad.

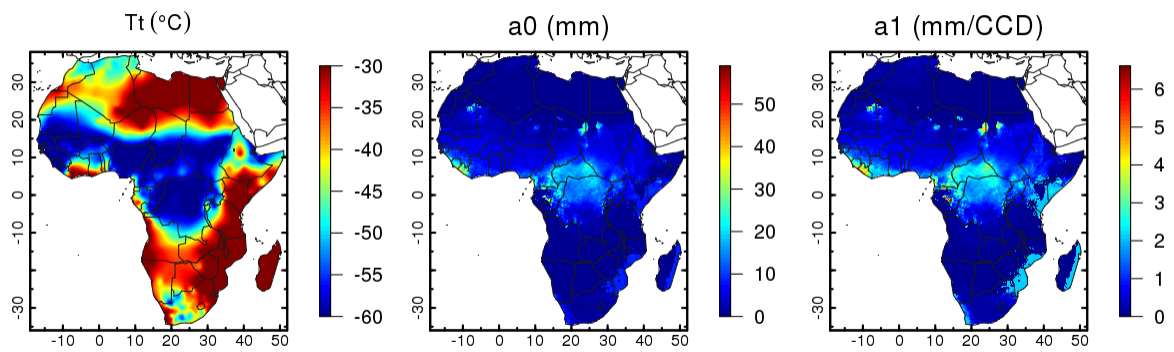


Figure A4.41. TAMSAT v3.0 calibration parameters for July, 5th pentad.

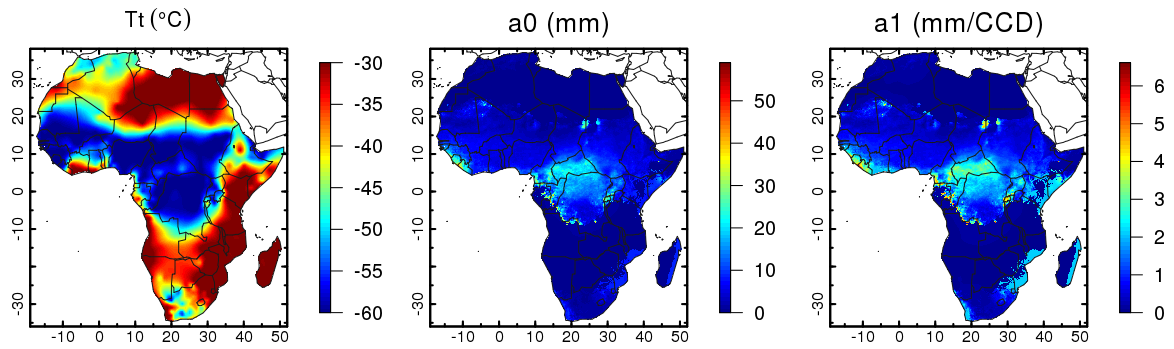


Figure A4.42. TAMSAT v3.0 calibration parameters for July, 6th pentad.

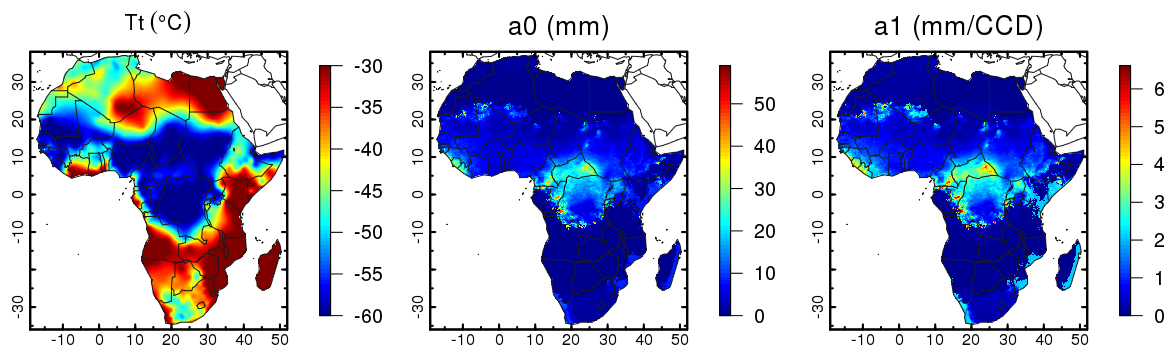


Figure A4.43. TAMSAT v3.0 calibration parameters for August, 1st pentad.

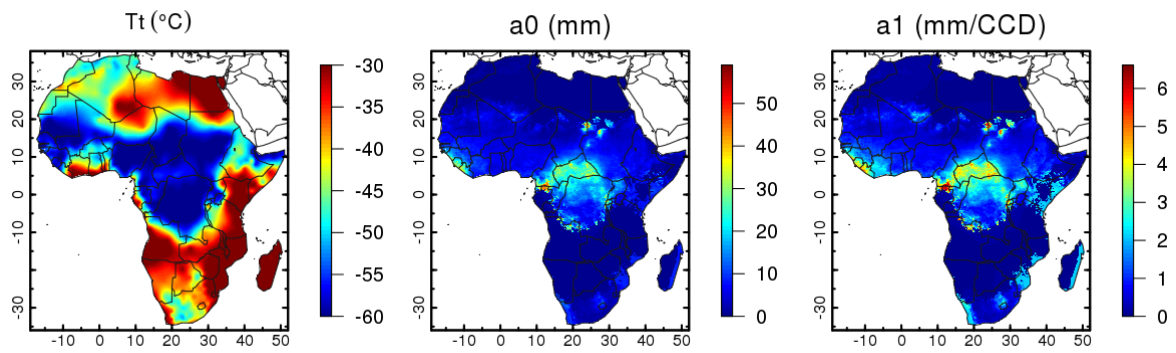


Figure A4.44. TAMSAT v3.0 calibration parameters for August, 2nd pentad.

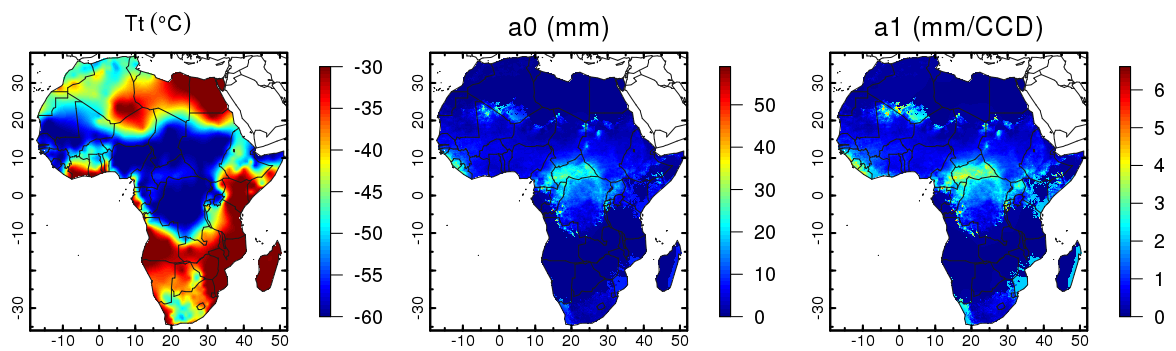


Figure A4.45. TAMSAT v3.0 calibration parameters for August, 3rd pentad.

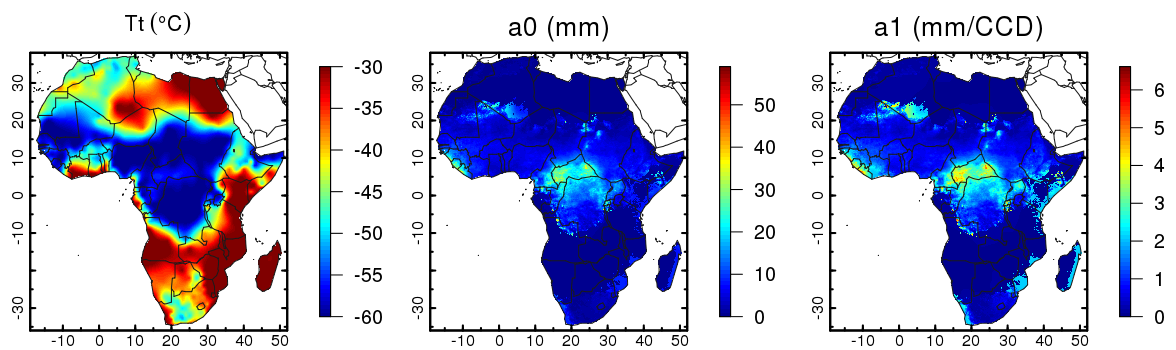


Figure A4.46. TAMSAT v3.0 calibration parameters for August, 4th pentad.

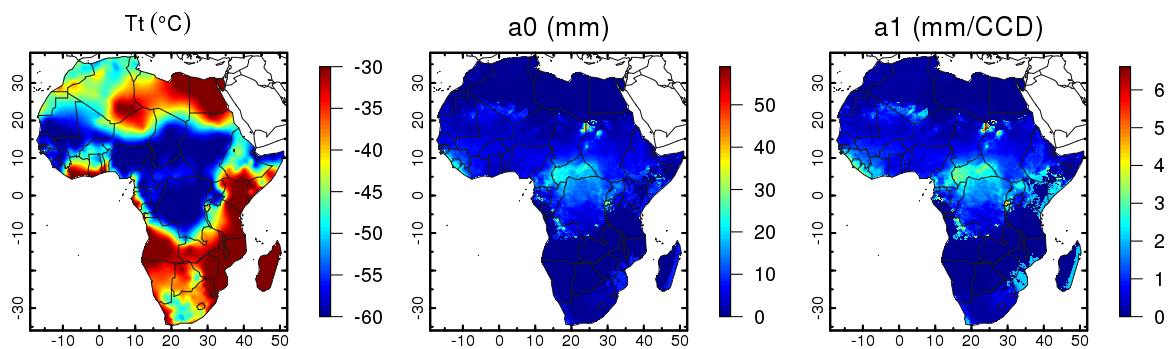


Figure A4.47. TAMSAT v3.0 calibration parameters for August, 5th pentad.

Figure A4.47. TAMSAT v3.0 calibration parameters for August, 5th pentad.

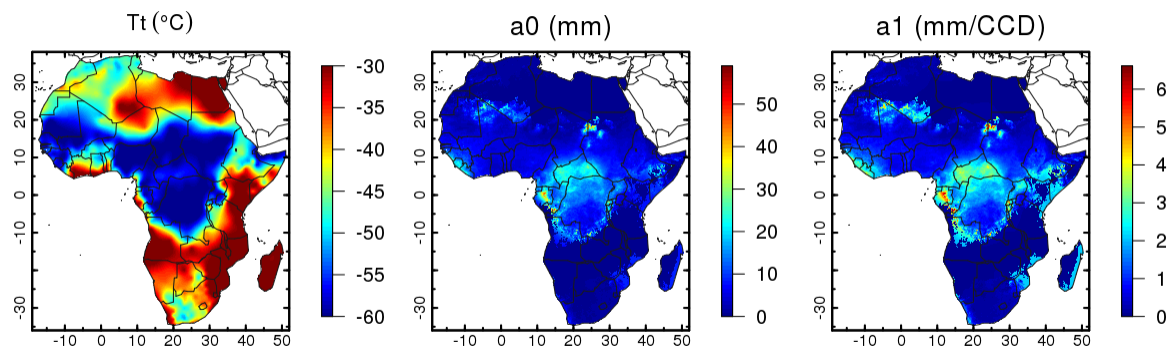


Figure A4.48. TAMSAT v3.0 calibration parameters for August, 6th pentad.

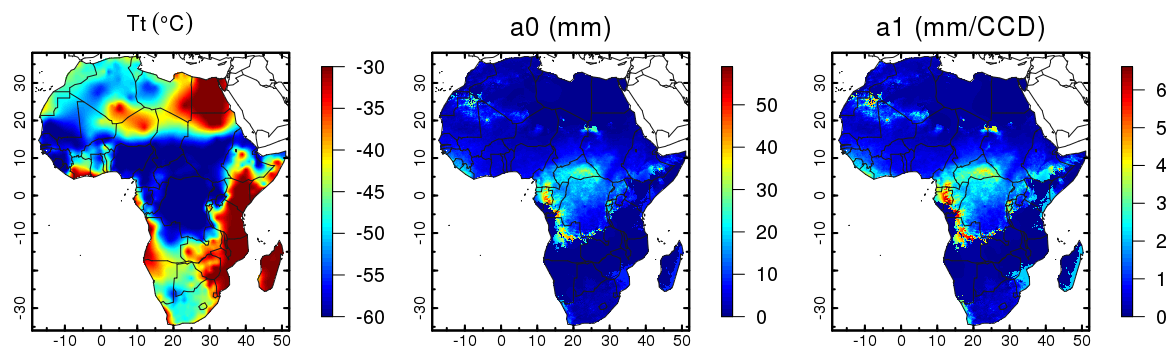


Figure A4.49. TAMSAT v3.0 calibration parameters for September, 1st pentad.

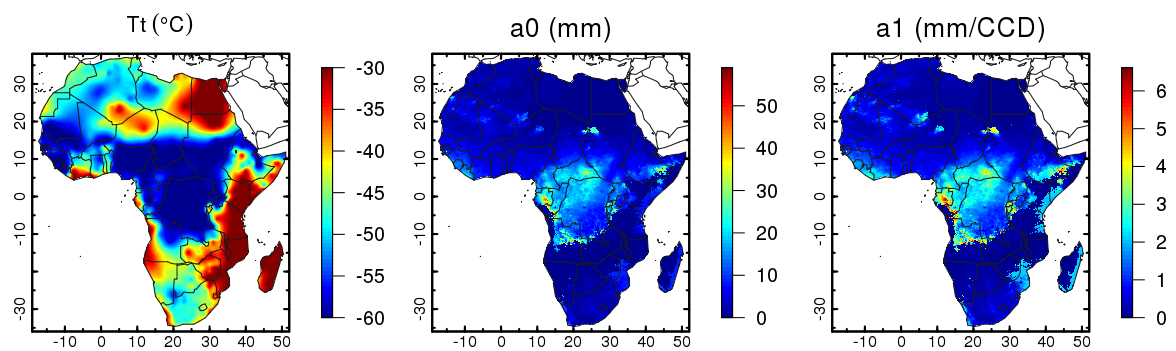


Figure A4.50. TAMSAT v3.0 calibration parameters for September, 2nd pentad.

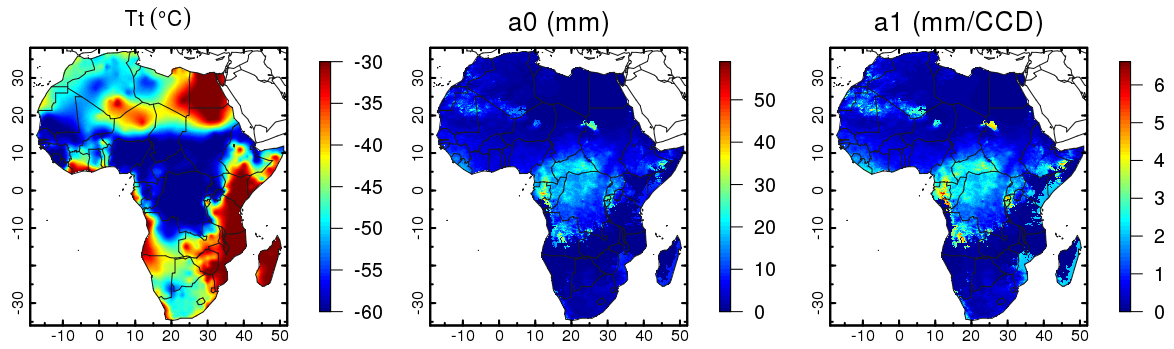


Figure A4.51. TAMSAT v3.0 calibration parameters for September, 3rd pentad.

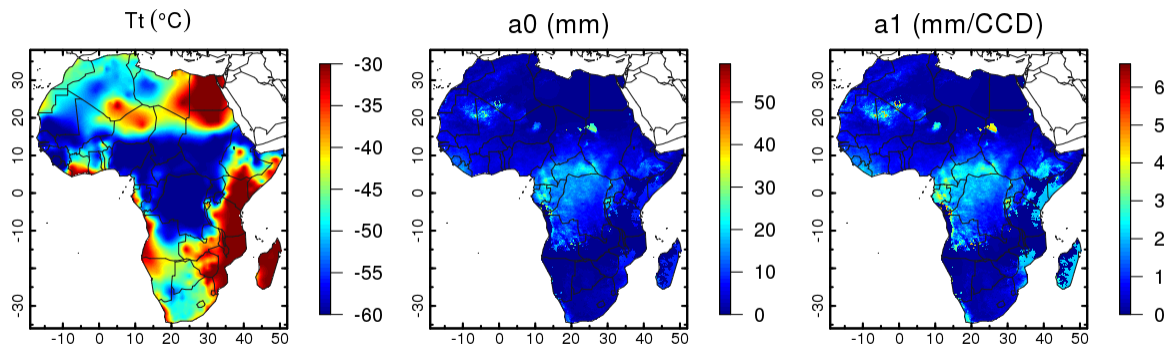


Figure A4.52. TAMSAT v3.0 calibration parameters for September, 4th pentad.

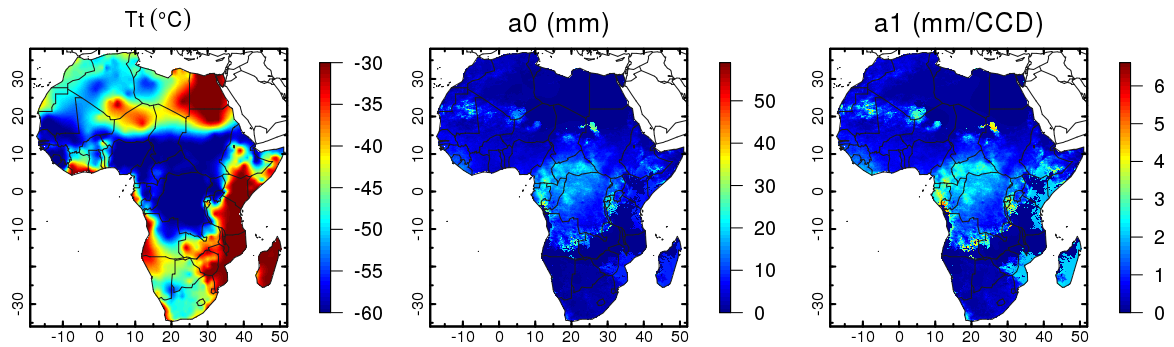


Figure A4.53. TAMSAT v3.0 calibration parameters for September, 5th pentad.

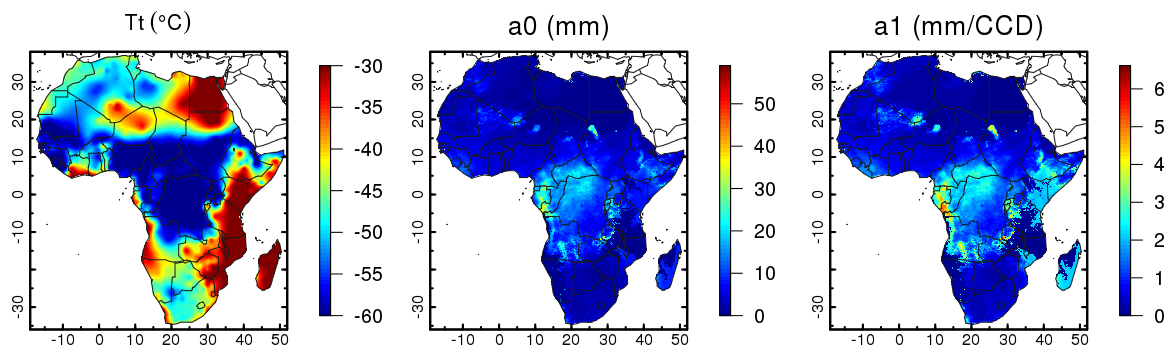


Figure A4.54. TAMSAT v3.0 calibration parameters for September, 6th pentad.

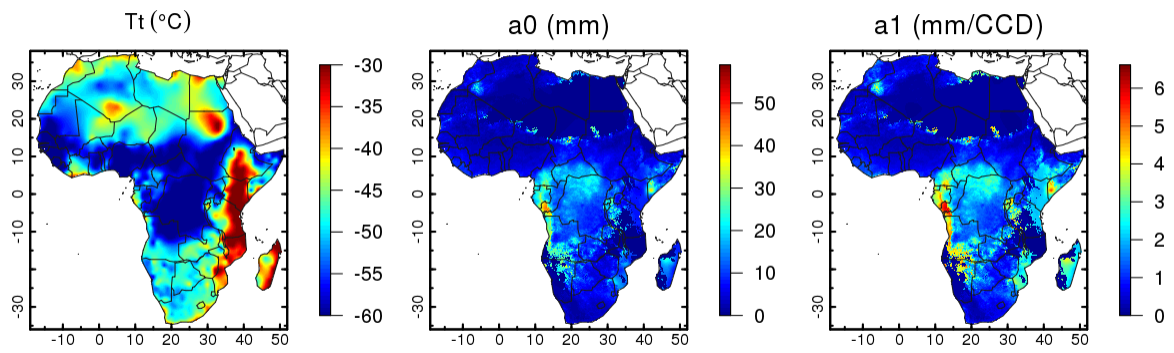


Figure A4.55. TAMSAT v3.0 calibration parameters for October, 1st pentad.

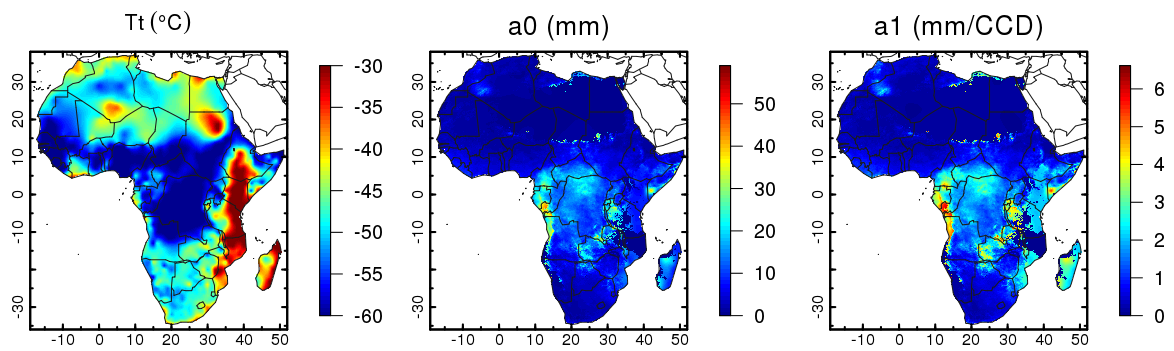


Figure A4.56. TAMSAT v3.0 calibration parameters for October, 2nd pentad.

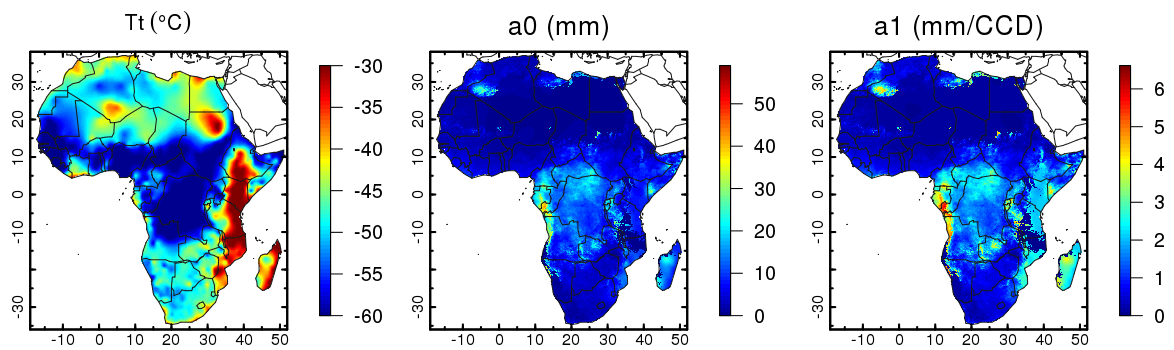


Figure A4.57. TAMSAT v3.0 calibration parameters for October, 3rd pentad.

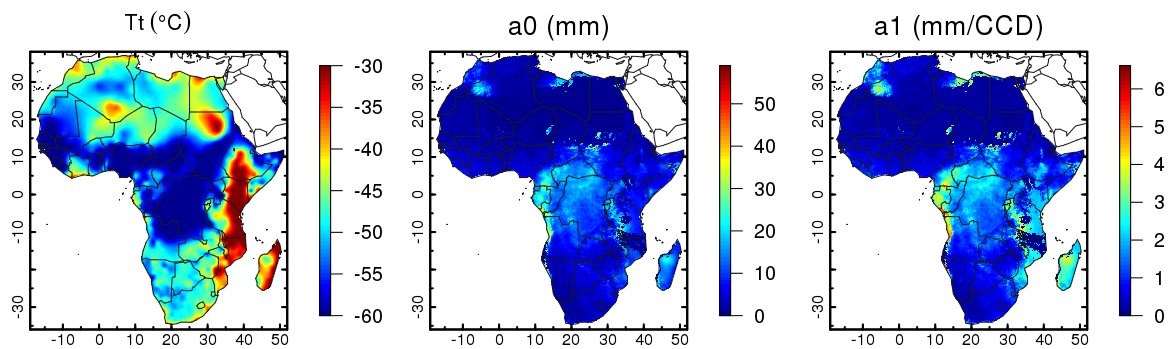


Figure A4.58. TAMSAT v3.0 calibration parameters for October, 4th pentad.

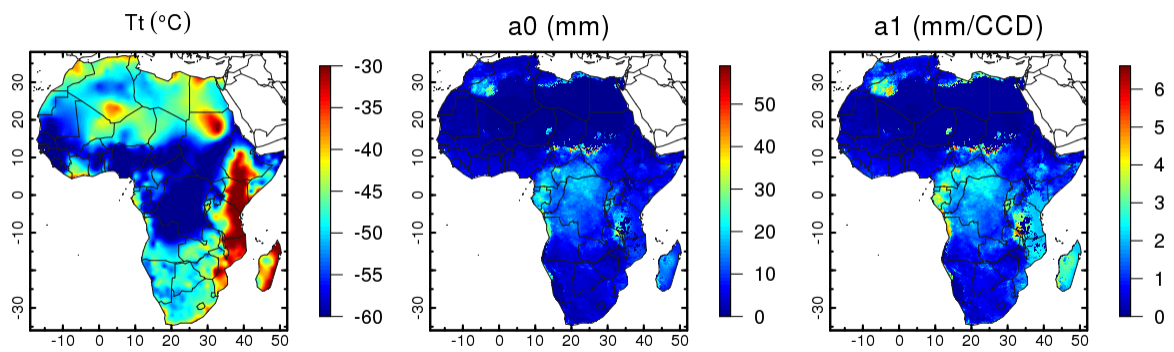


Figure A4.59. TAMSAT v3.0 calibration parameters for October, 5th pentad.

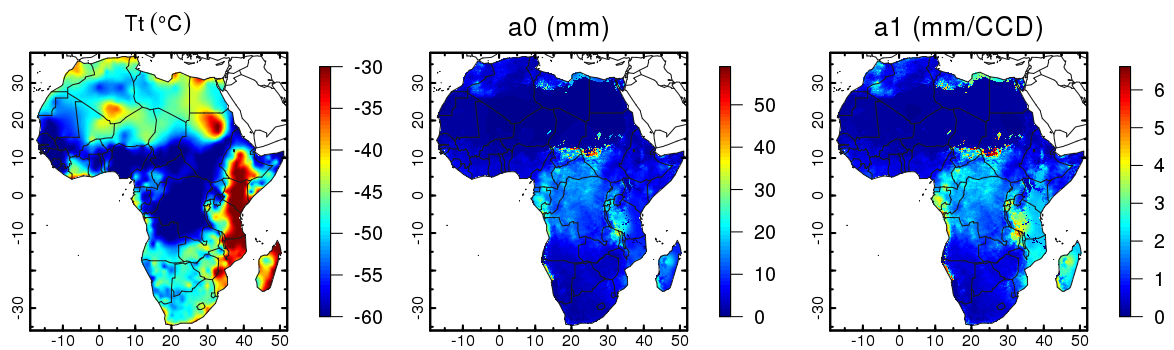


Figure A4.60. TAMSAT v3.0 calibration parameters for October, 6th pentad.

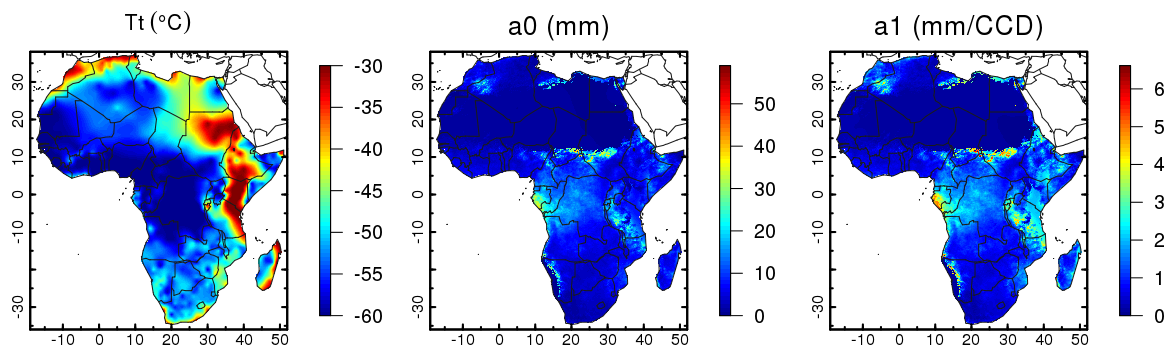


Figure A4.61. TAMSAT v3.0 calibration parameters for November, 1st pentad.

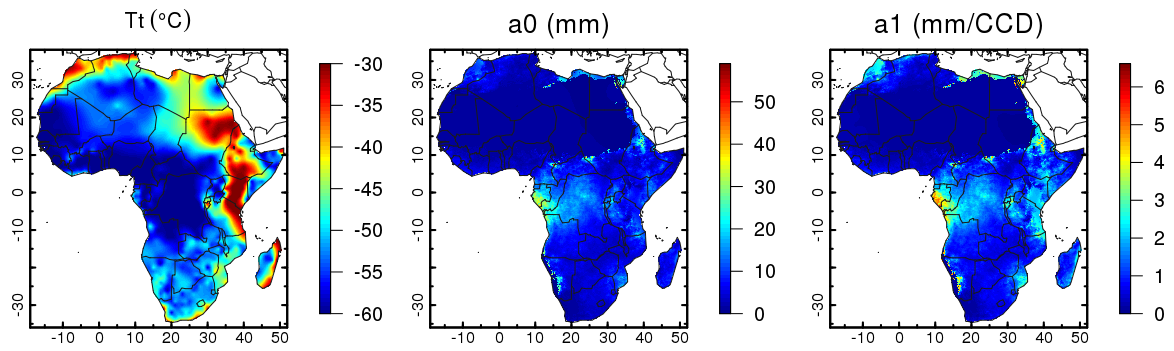


Figure A4.62. TAMSAT v3.0 calibration parameters for November, 2nd pentad.

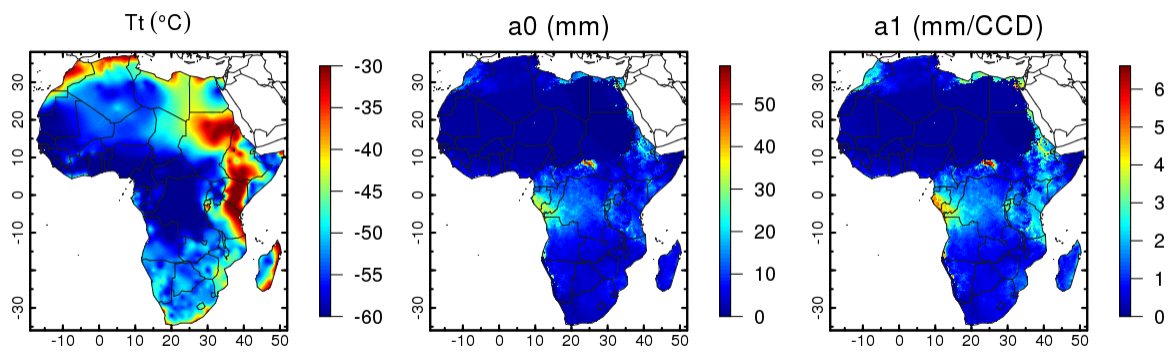


Figure A4.63. TAMSAT v3.0 calibration parameters for November, 3rd pentad.

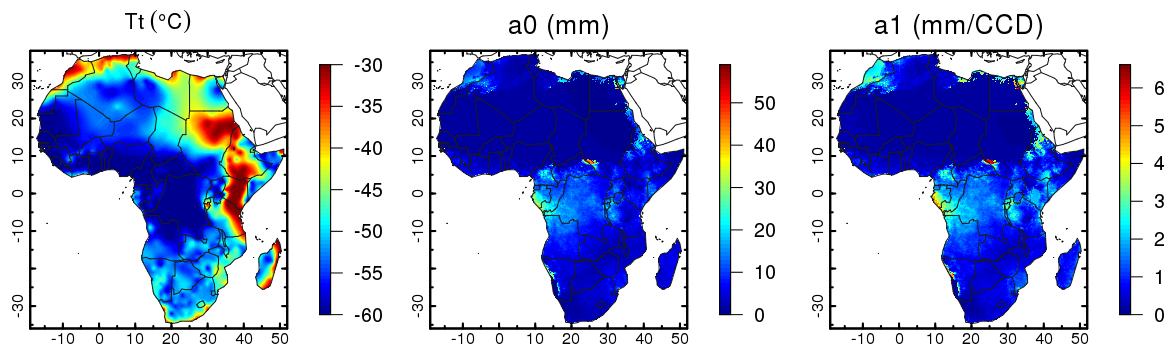


Figure A4.64. TAMSAT v3.0 calibration parameters for November, 4th pentad.

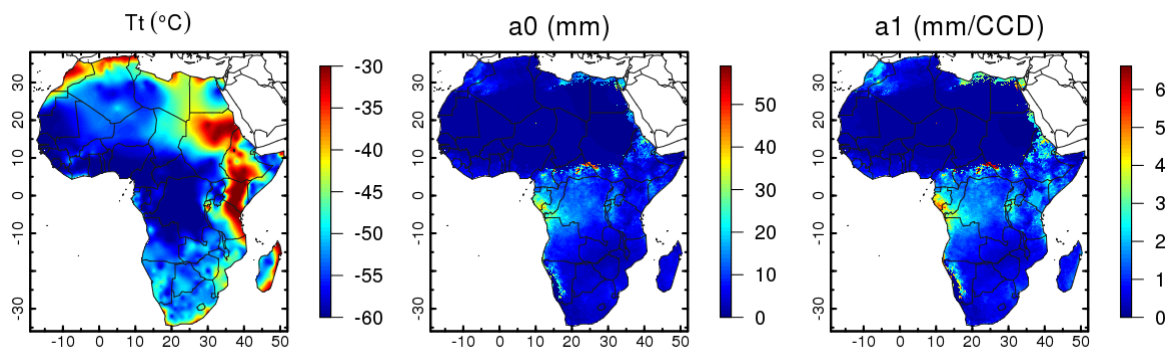


Figure A4.65. TAMSAT v3.0 calibration parameters for November, 5th pentad.

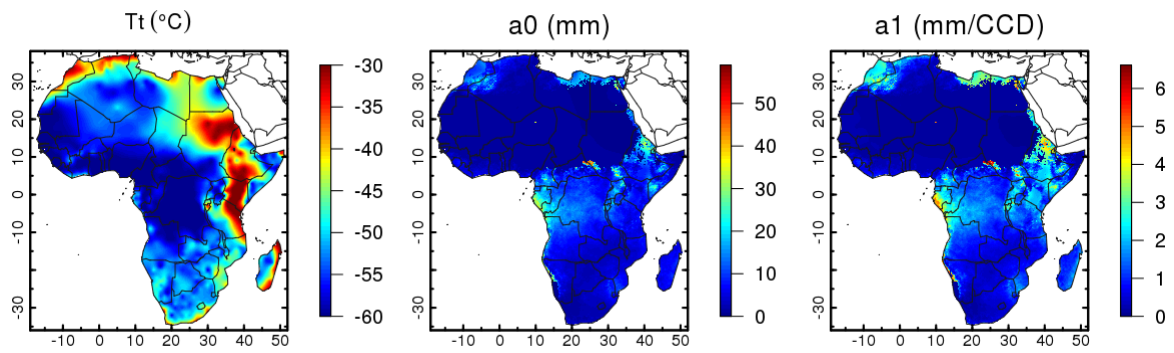


Figure A4.66. TAMSAT v3.0 calibration parameters for November, 6th pentad.

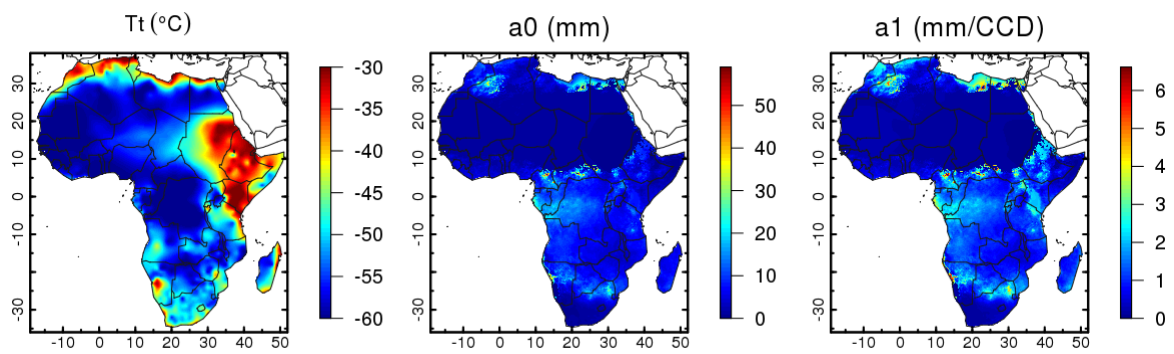


Figure A4.67. TAMSAT v3.0 calibration parameters for December, 1st pentad.

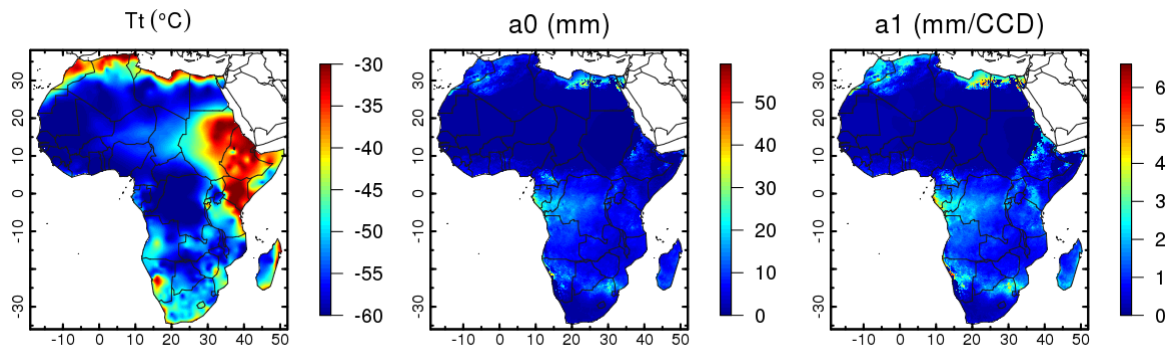


Figure A4.68. TAMSAT v3.0 calibration parameters for December, 2nd pentad.

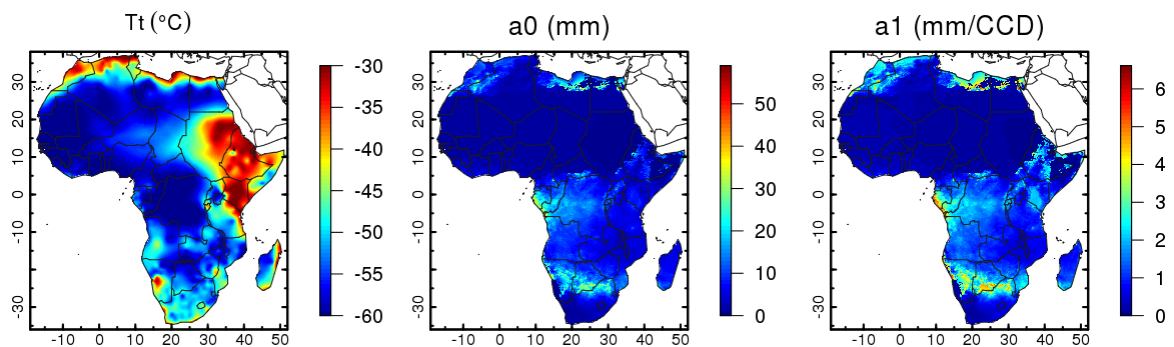


Figure A4.69. TAMSAT v3.0 calibration parameters for December, 3rd pentad.

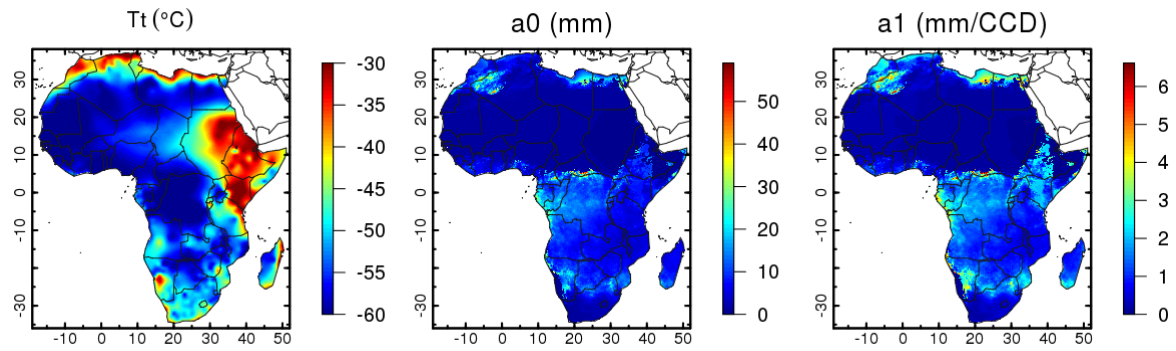


Figure A4.70. TAMSAT v3.0 calibration parameters for December, 4th pentad.

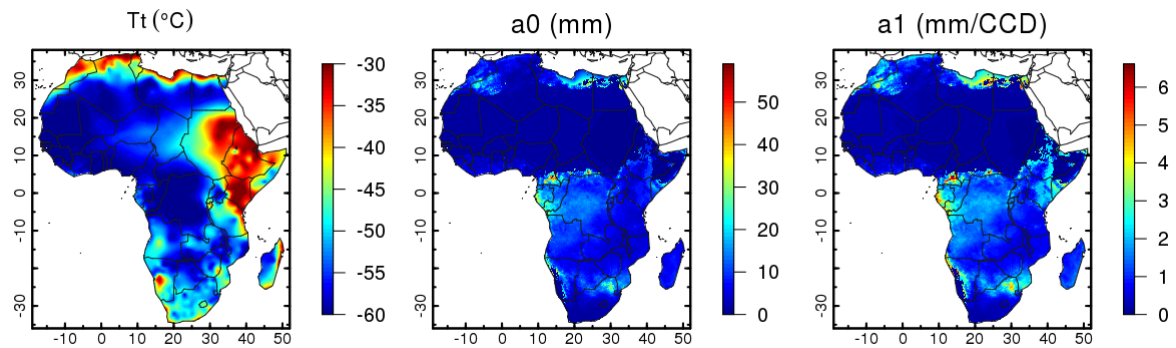


Figure A4.71. TAMSAT v3.0 calibration parameters for December, 5th pentad.

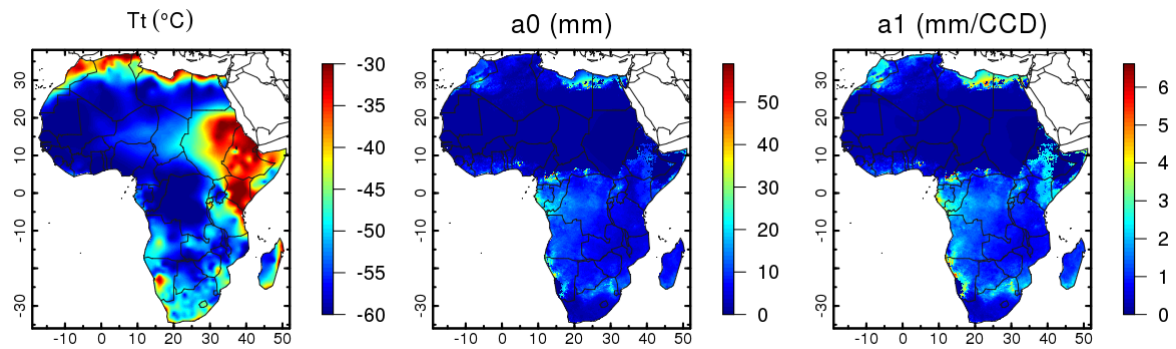


Figure A4.72. TAMSAT v3.0 calibration parameters for December, 6th pentad.